
Paving the way to 3D spatial omics: Methodological evolution of nanosecond infrared laser (NIRL)-based tissue sampling and further processing for low-input mass spectrometric analysis

Dissertation

for the acquisition of the academic degree

Doctor rerum naturalium

(Dr. rer. nat.)

at the Faculty of Mathematics, Informatics and Natural Sciences

Department of Chemistry

University of Hamburg

submitted by

Manuela Moritz

Hamburg, July 2024

Reviewers:

Prof. Dr. Hartmut Schlüter

Prof. Dr. Markus Fischer

Members of the examination committee:

Prof. Dr. Hartmut Schlüter

Prof. Dr. Wolfram Brune

Prof. Dr. Christian Betzel

Date of disputation:

29.11.2024

Date of print approval:

17.12.2024

The work was done from August 2020 to July 2024 at the University Medical Center Hamburg-Eppendorf in the working group of Mass Spectrometry and Proteomics, under the supervision of Prof. Dr. Hartmut Schlüter.

DEDICATED TO ME
AND ALL THE PEOPLE
WHO HAVE BEEN PART OF MY JOURNEY.

I. LIST OF PUBLICATIONS

- 1 Baerenfaenger, M., Moritz, M., Meyer, B., Quantitation of Glycopeptides by ESI/MS - size of the peptide part strongly affects the relative proportions and allows discovery of new glycan compositions of Ceruloplasmin. *Glycoconjugate journal* 2019, 36, 13–26. doi:10.1007/s10719-018-9852-5.
- 2 Hahn J., Moritz M., Voß H., Pelczar P., Huber S., Schlüter H., Tissue Sampling and Homogenization in the Sub-Microliter Scale with a Nanosecond Infrared Laser (NIRL) for Mass Spectrometric Proteomics. *International journal of molecular sciences* 2021, 22. doi:10.3390/ijms221910833.
- 3 Aypek H., Krisp C., Lu S., Liu S., Kylies D., Kretz O., Wu G., Moritz M., Amann K., Benz K., Tong P., Hu Z. M., Alsulaiman S. M., Khan A. O., Grohmann M., Wagner T., Müller-Deile J., Schlüter H., Puelles V. G., Bergmann C., Huber T. B., Grahammer F., Loss of the collagen IV modifier prolyl 3-hydroxylase 2 causes thin basement membrane nephropathy. *The Journal of clinical investigation* 2022, 132. doi:10.1172/JCI147253.
- 4 Voß H., Moritz M., Pelczar P., Gagliani N., Huber S., Nippert V., Schlüter H., Hahn J., Tissue Sampling and Homogenization with NIRL Enables Spatially Resolved Cell Layer Specific Proteomic Analysis of the Murine Intestine. *International journal of molecular sciences* 2022, 23. doi:10.3390/ijms23116132.
- 5 Stadlhofer R., Moritz M., Fuh M. M., Heeren J., Zech H., Clauditz T. S., Schlüter H., Betz C. S., Eggert D., Böttcher A., Hahn J., Lipidome Analysis of Oropharyngeal Tumor Tissues Using Nanosecond Infrared Laser (NIRL) Tissue Sampling and Subsequent Mass Spectrometry. *International journal of molecular sciences* 2023, 24. doi:10.3390/ijms24097820.
- 6 Dyshlovoy S. A., Hauschild J., Venz S., Krisp C., Kolbe K., Zapf S., Heinemann S., Fita K. D., Shubina L. K., Makarieva T. N., Guzii A. G., Rohlfing T., Kaune M., Busenbender T., Mair T., Moritz M., Poverennaya E. V., Schlüter H., Serdyuk V., Stonik V. A., Dierlamm J., Bokemeyer C., Mohme M., Westphal M., Lamszus K., von Amsberg G., Maire C. L., Rhizochalinin Exhibits Anticancer Activity and Synergizes with EGFR Inhibitors in Glioblastoma In Vitro Models. *Molecular pharmaceutics* 2023, 20, 4994–5005. doi:10.1021/acs.molpharmaceut.3c00217.
- 7 Navolić J., Moritz M., Voß H., Schlumbohm S., Schumann Y., Schlüter H., Neumann J. E., Hahn J., Direct 3D Sampling of the Embryonic Mouse Head: Layer-wise Nanosecond Infrared Laser (NIRL) Ablation from Scalp to Cortex for Spatially Resolved Proteomics. *Analytical chemistry* 2023, 95, 17220–17227. doi:10.1021/acs.analchem.3c02637.
- 8 Hahn, J., Moritz, M., Walter, A., Wieck, T., Moustafa A., Mansour W. Y., Harms C., Stenzel P., Heeren J., Haider M.-T., Lange, T. Schlüter H. in: Tarnok, A., Houston, J. P. (Eds.), *Imaging, Manipulation, and Analysis of Biomolecules, Cells, and Tissues XXII*, SPIE 2024 - 2024, p. 32.
- 9 Godbole S., Voß H., Gocke A., Schlumbohm S., Schumann Y., Peng B., Mynarek M., Rutkowski S., Dottermusch M., Dorostkar M. M., Korshunov A., Mair T., Pfister S. M., Kwiatkowski M., Hotze M., Neumann P., Hartmann C., Weis J., Liesche-Starnecker F., Guan Y., Moritz M., Siebels B., Struve N., Schlüter H., Schüller U., Krisp C., Neumann J. E., Multiomic profiling of medulloblastoma reveals subtype-specific targetable alterations at the proteome and N-glycan level. *Nature Communications* 2024, 15, 6237. doi:10.1038/s41467-024-50554-z.

II. TABLE OF CONTENTS

I.	List of Publications	5
II.	Table of Contents	6
III.	List of Abbreviations.....	7
1	Zusammenfassung	8
2	Summary	10
3	Introduction.....	12
3.1	The Challenges in Mass Spectrometry-based Spatial Omics	12
3.2	Latest Developments and Current Limitations in Spatial Tissue Sampling	13
3.3	Tissue Homogenization as Crucial Step in Sample Preparation and Associated Challenges.....	14
3.4	Short Pulse Mid-Infrared Laser Ablation for Simultaneous Tissue Sampling and Homogenization	15
4	Aim and Research Objectives.....	17
5	Cumulative part.....	18
5.1	Tissue Sampling and Homogenization in the Sub-Microliter Scale with a Nanosecond Infrared Laser (NIRL) for Mass Spectrometric Proteomics.....	18
5.2	Lipidome Analysis of Oropharyngeal Tumor Tissues Using Nanosecond Infrared Laser (NIRL) Tissue Sampling and Subsequent Mass Spectrometry	34
5.3	Tissue Sampling and Homogenization with NIRL Enables Spatially Resolved Cell Layer Specific Proteomic Analysis of the Murine Intestine	51
5.4	Direct 3D Sampling of the Embryonic Mouse Head: Layer-wise Nanosecond Infrared Laser (NIRL) Ablation from Scalp to Cortex for Spatially Resolved Proteomics.....	68
6	Discussion	77
7	Conclusion and Outlook.....	82
8	References	83
9	Appendix.....	90
9.1	Risk and Safety Statements.....	90
10	Acknowledgements.....	91
11	Declaration	92

III. LIST OF ABBREVIATIONS

3D	-	Three-dimensional
ANOVA	-	Analysis of variance
BOT	-	Base of tongue
CRC	-	Colorectal cancer
DDM	-	<i>n</i> -Dodecyl β -D-maltoside
DIVE	-	Desorption by impulsive vibrational excitation
DMS	-	Differential mobility spectrometry
DTT	-	Dithiothreitol
ECM	-	Extracellular matrix
EDTA	-	Ethylenediaminetetraacetic acid
FACS	-	Fluorescence-activated cell sorting
FFPE	-	Formalin-fixed paraffin-embedded
H&E	-	Hematoxylin and eosin
HPV	-	Human papillomavirus
IHC	-	Immunohistochemistry
IR	-	Infrared
ISH	-	In situ hybridization
LCM	-	Laser capture microdissection
LC-MS/MS	-	Liquid chromatography-tandem mass spectrometry
MIRL	-	Microsecond infrared laser
MRM	-	Multiple reaction monitoring
MS	-	Mass spectrometry
NIRL	-	Nanosecond infrared laser
OCT	-	Optical coherence tomography
OPSCC	-	Oropharyngeal squamous cell carcinoma
PARS	-	Photo acoustic remote sensing
PAC	-	Proportion of ambiguous clustering
PC	-	Phosphatidylcholine
PCA	-	Principal component analysis
PCT	-	Pressure cycling technology
PE	-	Phosphatidylethanolamine
PIRL	-	Picosecond infrared laser
PTFE	-	Polytetrafluoroethylene
PTM	-	Post-translational modification
ROI	-	Region of interest
SCC	-	Squamous cell carcinoma
SDC	-	Sodium deoxycholate
SDS	-	Sodium dodecyl sulfate
TAG	-	Triacylglycerol
UV	-	Ultraviolet
WALDI	-	Water-assisted laser desorption ionization

1 ZUSAMMENFASSUNG

In den letzten Jahren hat die Anzahl der massenspektrometrie-basierten räumlichen Omik-Studien deutlich zugenommen. Die Berücksichtigung der räumlichen Auflösung ermöglicht einen tieferen Einblick in die zelluläre Organisation und der Gewebe-Interaktionen, wodurch physiologische und pathologische Prozesse umfassender untersucht werden können. Trotz der wachsenden Nachfrage mangelt es derzeit an geeigneten Arbeitsabläufen, in denen die räumliche Information bei der Probenentnahme erhalten bleibt und zudem eine umfassende Proteom- und Lipidomanalyse erzielt wird. Die kurzgepulste Laserablation im mittleren Infrarotbereich bietet einen neuartigen Ansatz für die gleichzeitige Entnahme und Homogenisierung von Geweben. In einem schnellen und sanften Verdampfungsprozess werden alle Biomoleküle aus dem bestrahlten Bereich des Gewebes freigesetzt, während die benachbarten Gewebestrukturen intakt bleiben und die räumliche Information der Entnahmestelle erhalten bleibt. In dieser Dissertation wurde die Methodik der Nanosekunden-Infrarotlaser (NIRL)-basierten Gewebeentnahme und die anschließende Probenvorbereitung für die massenspektrometrische Analyse von geringen Einsatzmengen weiterentwickelt, mit dem Ziel diese für die dreidimensionale räumliche Omik anzuwenden. Da herkömmliche Protokolle für die *Bottom-up*-Proteomik und *Shotgun*-Lipidomik eine Verwendung von mehreren Milligramm Gewebe erfordern, wurden zunächst Arbeitsabläufe entwickelt, die eine robuste Verarbeitung für miniaturisierte Gewebevolumina von 500 nL, einer geringen Einsatzmenge von 500 µg entsprechend, ermöglichen. Mit der zusätzlichen Implementierung einer neuen Methode zum direkten Auffangen des entstehenden Gewebeaerosols an Objektträgern, konnte die *Bottom-up*-Proteomik von den miniaturisierten Gewebevolumina von Milz- und Dickdarmgewebe der Maus erfolgreich durchgeführt werden. In der Studie von Hahn & Moritz et al. konnten insgesamt 1.889 Proteine mit quantitativen Informationen identifiziert werden, was einer vergleichbaren Anzahl von Proteinen entspricht, die in einer früheren PIRL-basierten Studie unserer Gruppe gefunden wurden, bei der jedoch ein 50-fach größeres Gewebevolumen verwendet wurde. Die Ergebnisse der differentiellen quantitativen Proteomanalyse zeigten signifikant unterschiedliche Proteinabundanzen in den Geweben, die den erwarteten proteomischen Signaturen von Milz- und Dickdarmgewebe entsprachen, wodurch die Anwendbarkeit der NIRL-Ablation für weiche und muskelreiche Gewebetypen bestätigt wurde. In einer weiteren methodischen Entwicklung wurde die NIRL-basierte Gewebeentnahme erstmals mit einer quantitativen *Shotgun*-Lipidomanalyse kombiniert. In der Studie von Stadlhofer & Moritz et al. wurden menschliche Plattenepithelkarzinome des Oropharynx (OPSCC) und das umgebende Schleimhautgewebe untersucht. Mit der entwickelten Methode wurden insgesamt 755 Lipidspezies aus 13 Lipidklassen quantifiziert. Die Daten zeigen nicht nur Veränderungen in der Lipidzusammensetzung der unterschiedlichen Gewebe innerhalb eines Patienten, sondern auch zwischen verschiedenen Patienten. Die Ergebnisse zeigen Ähnlichkeiten in den Lipidprofilen der OPSCC-Proben aus verschiedenen Tumorlokalisationen. So wurden beispielsweise die Lipidklassen Phosphatidylcholin (PC) und Phosphatidylethanolamin (PE) in den OPSCC-Proben in höheren Konzentrationen gefunden als im entsprechenden nicht-tumorösen Oropharynxgewebe. Im Gegensatz dazu lassen sich die nicht-tumorösen Proben aus dem Zungengrund und den Tonsillen durch unterschiedliche Lipidzusammensetzungen charakterisieren. Auf Basis der methodischen Weiterentwicklung konnten trotz der kleinen Gewebevolumen von 500 nL, sowohl für die *Bottom-up*-Proteomik als auch für die *Shotgun*-Lipidomik reproduzierbare und vor allem umfangreiche Ergebnisse erzielt werden, was eine wichtige Grundlage für die Weiterentwicklung der NIRL-basierten Methodik für die dreidimensionale räumliche Omik darstellte. In der Studie von Voß & Moritz et al. wurden mittels der NIRL-basierten Gewebeentnahme Proben aus drei verschiedenen Regionen des Dickdarms (ascendens, transversum, descendens) sowie von acht

aufeinanderfolgenden Gewebeschichten entnommen. Die Proben wurden mit dem zuvor entwickelten Protokoll für die *Bottom-up*-Proteomik verarbeitet, mit dem, durch eine weitere Optimierung im Versuchsaufbau, die Zahl der identifizierten Proteine auf 3.053 Proteine für die regionsaufgelöste und 2.882 Proteine für die schichtaufgelöste Proteomanalyse erhöht werden konnte. Auf Grundlage der quantitativen *Bottom-up*-Proteomik konnten die drei Dickdarmregionen durch signifikant unterschiedlich abundante Proteine, die hauptsächlich mit verschiedenen Stoffwechselprozessen in Verbindung stehen, differenziert werden. Darüber hinaus konnten auf Basis der schichtweise ablatierten Proben erstmals eine räumlich aufgelöste Proteomanalyse des Mäusedarms mit einer axialen Auflösung von 117 µm durchgeführt werden. Während die oberen und unteren Ablationsschichten eindeutig der Mukosa beziehungsweise der Muscularis propria zugeordnet werden konnten, konnten die Zwischenschichten keinen morphologischen Strukturen zugewiesen werden, was möglicherweise auf eine unzureichende räumliche Auflösung zurückzuführen ist. Um die räumliche Auflösung weiter zu verbessern, wurden die Probenvorbereitungsschritte weiter optimiert, indem der Probenverlust durch mögliche Adsorptionseffekte minimiert wurde. Dadurch konnte das Gewebevolumen, welches für die umfangreiche und reproduzierbare Analyse mittels *Bottom-up*-Proteomik benötigt wird, um den Faktor 20 von 600 nL auf 30 nL reduziert werden. Auf Basis dessen wurde die axiale Auflösung auf 40 µm erhöht und in der neuesten Studie von Navolić & Moritz et al. für die räumlich aufgelöste Proteomanalyse eines intakten embryonalen Mauskopfes demonstriert. Im Bereich des Vorderhirns wurden neun aufeinanderfolgende Gewebeschichten direkt von der Kopfhaut bis zum Zerebralen Kortex mittels der NIRL-basierten Gewebeentnahme gewonnen. Trotz des deutlich reduzierten Ablationsvolumens wurden 5.031 Proteine identifiziert, von denen 3.126 Proteine mit quantitativen Informationen gefunden wurden, wodurch der Erfolg in der weiteren Methodenoptimierung hervorgehoben wird. Während die oberflächlichen Schichten eindeutig den Haut- und Knochenstrukturen zugeordnet werden konnten, wurden zudem spezifische Markerproteine für die Hirnhäute identifiziert, die mit herkömmlichen Techniken nur schwer zugänglich sind. Darüber hinaus konnten auf Basis der räumlich aufgelösten Proteomanalyse erstmals die graduellen Veränderungen der Proteinabundanzen in der hochkomplexen Schichtstruktur des Zerebralen Kortex im Entwicklungsstadium aufgezeigt und potentielle neue Markerproteine für die kortikalen Schichten vorgeschlagen werden. Abschließend lässt sich sagen, dass auf Grundlage der methodischen Weiterentwicklung der NIRL-basierten Gewebeentnahme und der anschließenden Probenvorbereitung für die massenspektrometrische Analyse von kleinen Einsatzmengen erfolgreich das Ziel der dreidimensionalen räumlichen Omik umgesetzt werden konnte. Bei der NIRL-basierten Gewebeentnahme kann der Bereich von Interesse direkt aus intaktem, frisch gefrorenem Gewebe entnommen werden, wodurch die dreidimensionale räumliche Information erhalten bleibt. Da diese herausragende Technik keine Einschränkungen hinsichtlich der Gewebeart aufweist und die schichtweise Probenentnahme unabhängig von der gegebenen Gewebestruktur erfolgt, ist nicht nur für geschichtete, sondern auch für komplexe und empfindliche Gewebestrukturen eine orts aufgelöste Analyse möglich. Die Implementierung einer multimodalen Bildgebung für die zusätzliche Validierung und gezielte Ablation wird die Anwendung der NIRL-basierten Gewebeentnahme für die dreidimensionale räumliche Omik noch weiter stärken und damit zunehmend den Weg für die Untersuchung von Forschungsfragen ebnet, die bisher aufgrund methodischer Limitationen unbeantwortet blieben.

2 SUMMARY

In recent years, there has been a significant increase in the number of mass spectrometry-based spatial omics studies. Considering the spatial resolution allows for a deeper understanding of the cellular organization and tissue interactions, whereby physiological and pathological processes can be investigated more comprehensively. Despite the growing demand, there is currently a lack of suitable workflows in which both the spatial information in the tissue is retained during sampling and comprehensive coverage is achieved in the subsequent proteome and lipidome analysis. A novel approach utilizes short pulse mid-infrared laser ablation for the simultaneous sampling and homogenization of tissues. Biomolecules are released from their cellular tissue compartments via a gentle and cold vaporization process. Moreover, this technology preserves the spatial information of the sample location and provides highly precise sampling by maintaining the integrity of the surrounding tissue area. In this dissertation, the methodology of nanosecond infrared laser (NIRL)-based tissue sampling and subsequent processing for low-input mass spectrometric omics was further developed, paving the way for an application in three-dimensional spatial omics. Given that common sample processing workflows for bottom-up proteomics and shotgun lipidomics necessitate the use of tissue amounts of several milligrams for robust processing, workflows were developed enabling the robust processing of miniaturized tissue volumes of 500 nL, corresponding to low input amounts of 500 µg. The implementation of a novel aerosol collection method, as described in the study performed by Hahn & Moritz et al., enabled the successful bottom-up proteome analysis of miniaturized tissue volumes of murine spleen and colon tissue. This resulted in the identification of 1,889 proteins with quantitative information. In comparison to a previous PIRL-based study conducted by our research group, in which a 50-fold larger tissue volume was utilized, a comparable number of proteins was identified. The results of differential quantitative proteome analysis revealed significantly different protein abundances in the tissues displaying expected proteomes of spleen and colon tissue. Accordingly, the applicability of NIRL ablation for soft and muscle-rich tissue types was confirmed. In a further methodological development, NIRL-based tissue sampling was combined with quantitative shotgun lipidome analysis, for the first time. In the study of Stadlhofer & Moritz et al., biopsies from human squamous cell carcinomas of the oropharynx (OPSCC) and surrounding mucosa tissue were ablated by NIRL. In total, 755 lipid species from 13 lipid classes were quantified. The data demonstrated not only intra- but also interpatient alterations in lipid composition. The findings confirm similarities in the lipid profiles of the OPSCC samples from different tumor locations. For instance, the lipid classes phosphatidylcholine (PC) and phosphatidylethanolamine (PE) were found to be present in higher concentrations in the OPSCC samples than in the respective non-tumorous oropharyngeal tissue. In contrast, mucosa samples from the base of tongue and tonsil exhibit distinct lipid compositions. Since comprehensive analysis with high coverage was achieved for both bottom-up proteomics and shotgun lipidomics, the suitability of the developed processing workflows for the sampled tissue volumes was verified and provided the foundation for further development towards spatial omics. In the study of Voß & Moritz et al., NIRL ablation was utilized for the tissue sampling of three different colon parts (ascending, transverse, descending) and for layer-by-layer sampling of eight consecutive intestinal tissue layers. The samples were processed by the previously developed bottom-up proteomics workflow. The optimization of the experimental setup further enhanced the number of identified proteins to 3,053 proteins for the region-resolved and 2,882 proteins for the layer-resolved proteome analysis. Based on quantitative bottom-up proteome analysis, colon regions were distinguished by significantly differentially abundant proteins mainly corresponding to metabolic processes. Moreover, for the first time, spatially resolved proteome analysis of murine intestine was performed with an axial resolution of 117 µm. While the top and bottom ablation layers could be clearly assigned to the mucosa and the muscularis propria respectively, the cellular identity of the intermediate layers could not be verified, possibly due to insufficient spatial resolution. To further improve the spatial resolution, the sample processing protocol was optimized by minimizing sample loss due to potential adsorption

effects. The ablation volume, which is necessary for reproducible and global analysis, was reduced by a factor of 20, from 600 nL to 30 nL. Accordingly, the study by Navolić & Moritz et al. allowed for the spatially resolved proteome analysis of intact embryonic mouse head with an even higher axial resolution of 40 μm . Targeting the forebrain region, nine consecutive tissue layers were directly ablated from the scalp to the cerebral cortex. Despite the significantly reduced ablation volume, 5,031 proteins were identified including 3,126 proteins with quantitative information, underlining the successful method optimization. While the superficial layers were clearly assigned to skin and bone structures, specific marker proteins for the meninges were also identified, which are difficult to access by conventional techniques. Moreover, gradual changes in spatial protein abundances were analyzed in the highly complex cortex lamination at developmental stage, for the first time. According to this, potential new marker proteins for the cortical layers were proposed. To conclude, the methodological evolution of NIRL-based tissue sampling and further processing for low-input mass spectrometric analysis has enabled the successful application for 3D spatial omics. The region of interest can be sampled directly from intact fresh-frozen tissues, whereby the three-dimensional spatial information is maintained. As this outstanding technique has no limitation in tissue type and the layer-by-layer sampling is performed independently of the given tissue architecture, spatially resolved analysis is not only enabled for layered but also complex and sensitive tissue structures. The future incorporation of image guidance will enable cross-validation and targeted ablation, therefore further strengthening the application of NIRL-based tissue sampling for 3D spatial omics and paving the way for answering research questions, which previously remained unanswered due to methodological limitations.

3 INTRODUCTION

3.1 THE CHALLENGES IN MASS SPECTROMETRY-BASED SPATIAL OMICS

Omics research is based on the identification, characterization, and quantification of the entirety of biomolecules originating from biological samples like cells, body fluids, and tissues [1]. Over the last decade, there has been a notable increase in the number of studies that have focused on spatial omics. This field of research involves the analysis of the molecular composition of tissue samples, with a simultaneous consideration of the spatial information related to the sampling site [2]. Tissues are organized in distinct functional regions composed of multiple cell types possessing different characteristics [3]. To gain a deeper understanding of the drivers of physiological and pathophysiological processes, deeper insights into the molecular characteristics of tissues at the spatial and cellular levels are needed. Accordingly, powerful techniques like spatial genomics [4] and transcriptomics [5, 6] have been developed facilitating insights into tissue dynamics at the cellular level. In contrast, the acquisition of both in-depth spatial information and comprehensive coverage for proteomics, lipidomics and metabolomics is still challenging [7, 8]. In contrast to sequencing-based approaches, which are utilized in spatial genomics and transcriptomics, mass spectrometry-based techniques are employed to investigate the proteome, metabolome, and lipidome. This is due to the fact that biomolecules, including proteins, metabolites, and lipids, cannot be amplified [9]. Mass spectrometry is an invaluable tool for comprehensively elucidating cellular composition and pathological alterations. Furthermore, it allows for a high-throughput approach, which is particularly advantageous in the context of large-scale studies. It is therefore crucial to ensure that the quantity of the analyte present in the sample, especially following sample preparation, is sufficient to allow for the intrinsic sensitivity of the mass spectrometric analysis. Therefore, the sample preparation is a particularly challenging aspect of this field, especially when biological material is limited to low-input amounts or when the respective analytes are at low abundance [10–12]. The development of highly sensitive mass spectrometers has enabled the proteome and lipidome analysis, with sample amounts down to single cells [10, 12–14]. However, there is currently a lack of streamlined workflows that combine spatial sample collection and sample processing of low-input amounts to produce high-quality resources. As in all omics research fields, the biomolecules must be released from the cellular compartments prior to further downstream processing and analysis [15]. It is essential to ensure not only high reproducibility and maximum recovery in the release and solubilization of the biomolecules, but also to maintain the native state of the biomolecules as far as possible. Especially in quantitative analysis, it must be ensured that differences in the abundances correspond, for example, to healthy and disease state and are not due to insufficient homogenization, which leads to different analyte concentrations [16, 17]. Moreover, for spatial omics, a sample collection method is required that preserves the spatial information of the sampling site. Thereby, the spatial resolution to be achieved is dependent on both the precision of the sampling tool and the required sample amount for reproducible processing and subsequent mass spectrometric analysis. This further underscores the significance of optimizing sample processing workflows through the development of reliable and high-throughput methodologies for comprehensive and global analysis of low-input amounts.

3.2 LATEST DEVELOPMENTS AND CURRENT LIMITATIONS IN SPATIAL TISSUE SAMPLING

With the advent of spatial omics several tissue sampling methods have been developed. The spatial resolutions achieved range from millimeter to sub-micrometer depending on the precision of dissecting tools [18]. Initial attempts started with the dissection of different anatomic regions to perform spatial omics [19–21]. For the spatially resolved analysis of layered tissues (e.g., skin, intestine), sample preparation protocols were developed separating distinct cellular layers by mechanical, enzymatic and chemical treatment [22, 23]. However, it is rarely given that all layers can be separated due to methodological limitations, as observed in the preceding study by Dyring-Andersen et al. (2020), where spatially resolved proteome analysis of human skin was performed [24]. The spatial resolution achievable is contingent upon both the intrinsic tissue architecture and the suitability of the separation technique employed. Consequently, contamination by neighboring cell layers or loss of layers may occur, as evidenced by the dissociation of the epidermal-dermal junction [23]. In order to analyze a single cell type, pure cell suspensions can be achieved by dissociating tissue samples by enzymatic treatment and subsequent fluorescence-activated cell sorting (FACS) [24]. However, this process results in the loss of important components of the tissue microenvironment, such as the extracellular matrix (ECM), as well as the spatial information [18].

In contrast, laser capture microdissection (LCM) is a powerful sampling technique with high precision enabling the isolation of cell clusters or even single cells from tissue sections without contamination of surrounding cells [25, 26]. Furthermore, it allows for the preservation of the extracellular matrix (ECM). Under direct microscopic visualization, an infrared or UV laser is used to microdissect regions of interest (ROI) from tissue sections with a thickness of 2-15 μm [25–27]. The tissue samples are typically formalin-fixed prior to staining, as this process preserves the morphologies of the cells, which is essential for histopathological evaluation. However, the use of aldehyde-based fixatives has been shown to significantly impact the quality of macromolecules [28]. The formation of cross-links between proteins and between nucleic acids and proteins results in a notable decline in the quality of the biomolecules, which subsequently impairs their suitability for further analysis [25, 29]. In contrast, the application of LCM to frozen tissue sections not only allows for the recovery of high-quality proteins and mRNA [28, 30], but is also advantageous with regard to lipidomics, given that LCM often utilizes formalin-fixed paraffin-embedded (FFPE) tissues. The organic solvents employed for dehydration and clearing of tissue samples prior to paraffin embedding extract the majority of lipids, which are thereby lost for subsequent analysis [31]. Nevertheless, freezing and cryostat sectioning can significantly disrupt the histological architecture of the tissue [28]. As LCM is accomplished through identification of cells by morphological characteristics [26], a consecutive cryo-section can be stained and imaged for identifying features by cross-referencing of native and stained images [10]. Regardless of whether fixed or frozen sections are used, the ROIs must be selected manually, if necessary in consultation with a pathologist, which is very elaborate and time-consuming [25, 32]. The most significant drawback of LCM with regard to spatial omics is that it is restricted to tissue sections, with spatial information being obtained in a two-dimensional manner. Accordingly, the site of action as it is given in the overall tissue specimen is not sufficiently considered. The computational stacking of sequential tissue sections now permits three-dimensional analysis. However, this application is very demanding in terms of time and cost, and therefore not suitable for high-throughput applications [33].

3.3 TISSUE HOMOGENIZATION AS CRUCIAL STEP IN SAMPLE PREPARATION AND ASSOCIATED CHALLENGES

Tissue homogenization typically employs a combination of mechanical techniques, including mortar and pestle, cryogrinding, sonication, bead milling, and barocycling, in conjunction with detergents for cell lysis [34]. This is done with the aim of achieving complete release and solubilization of the biomolecules to be investigated from the cells and tissue compartments [35]. As the efficiency of homogenization affects the extent of identified biomolecules and ultimately the biological interpretation of the data, it is crucial to choose an appropriate mechanical method for efficient tissue disruption depending on the nature of the tissue sample. For some tissue types including bone, heart, lung, intestine, and skin an increase of mechanical force or time of exposure is needed for efficient tissue disruption while soft tissues like spleen, brain and liver can be homogenized by minimal physical force [36].

In general, homogenization should be performed as fast as possible and at low temperatures. During the process of homogenization, several enzymes are released from cellular compartments, potentially leading to alterations in the original composition of biomolecules due to chemical reactions and degradation processes [37, 38]. For instance, this may result in changes to posttranslational modifications (PTMs), playing a significant role in many diseases [39]. Therefore, it is even more important to be able to analyze the biomolecules as they are present in their native tissue environment. Pressure cycling technology (PCT) is a sample processing technique using alternating cycles of ultrahigh and low hydrostatic pressures. The pressure- and temperature-controlled homogenization is advantageous in terms of less potential degradation processes during sample processing [15, 40]. In addition, the automation of homogenization using PCT offers less person-to-person variability and enables a parallel processing of multiple samples compared to techniques like mortar and pestle which rely on manual grinding. Most of the conventional homogenization techniques are designed for tissue amounts of several milligrams. Accordingly, efficient and consistent homogenization of smaller tissue samples for the reproducible extraction of biomolecules remain challenging [15, 38]. The latest developments of PCT, now enable tissue homogenization of biopsy-size tissue samples corresponding to less than 1 mg tissue amount and also improved extraction of biomolecules from hard and fibrous tissue [15, 41]. However, with this method, some hard and relatively large tissues remain incompletely lysed resulting in varying extraction efficiencies.

The efficiency and reproducibility of biomolecule extraction, however, not only depends on the tissue disruption, but also the solvent composition used [38, 39]. Since biomolecules are characterized by different physico-chemical properties, the most efficient extraction protocols often only cover a restricted type of biomolecules. Thus, different methods are needed for extracting different molecules (e.g., proteins and lipids) from tissue samples [42]. Moreover, even within a biomolecule class, the solubilization behavior widely differs [17]. Both proteins and lipids are characterized by inherent diversity in their molecular structures exhibiting variety of functional roles and localizations in cell [43, 44]. For example, it is more difficult to solubilize membrane proteins than proteins of the cytoplasm, due to their location in the lipid-rich cell membrane. According to this, the ionic detergent sodium dodecyl sulfate (SDS) or the chaotropic agent urea is used for enhanced extraction of membrane proteins. Moreover, SDS can inhibit protease and phosphatase activity [37] as well as lipase activity [38]. However, when choosing the solvent composition, it has to be considered that detergents or chaotropes change the native conformation of proteins and functional studies cannot be performed [37]. In addition, it is essential to ensure that the solvents used are suitable for chromatography and mass spectrometry (MS) having no interfering or suppressing effect like SDS, which has to be removed prior mass spectrometric analysis [35].

3.4 SHORT PULSE MID-IRRED LASER ABLATION FOR SIMULTANEOUS TISSUE SAMPLING AND HOMOGENIZATION

In the past decade, a novel approach for simultaneous tissue sampling and homogenization emerged using short pulse mid-infrared laser ablation. This technique has been successfully demonstrated by the application of picosecond (PIRL), nanosecond (NIRL) and microsecond (MIRL) infrared lasers, where the wavelength is specifically tuned to match the absorption maximum of water at 2.94 μm [45]. Thereby the energy of the IR laser is absorbed by water molecules within the tissue and immediately converted into translational energy by intramolecular stretching vibrations in the oxygen-hydrogen bonds of the water molecules. The ablation process leads to the decomposition of the tissue and thereby to the transfer into the gas phase [46].

The group of Dwayne Miller intensively studied the ablation process using PIRL and proposed an underlying mechanism of desorption by impulsive vibrational excitation (DIVE) [47, 48]. The picosecond pulses of PIRL results in an ultrafast transition of water molecules from liquid to gaseous phase [48]. When tissue samples are irradiated by PIRL, ultra-efficient material ejection is achieved within a cold vaporization process since the adiabatic expansion of the formed aerosol plume into the gas phase results in a cooling effect. In a previous study performed by our group, it was demonstrated that PIRL ablation is an effective method for the release of proteins with molecular weights ranging from a few kilodaltons to several million daltons [49]. Moreover, posttranslational modifications, including glycosylation and phosphorylation, were observed to remain intact. The detection of enzymatic activity in the PIRL homogenate provided evidence that the proteins were not denatured by PIRL ablation [49]. In comparison to conventional tissue homogenization by mortar and pestle, the PIRL-based homogenization method yielded higher protein amounts and a greater number of protein identifications were found by bottom-up proteomics [50]. Moreover, the presence of more intact proteoforms was confirmed, thereby substantiating the hypothesis that less degradation occurs due to the significantly faster sampling and homogenization process compared to mechanical homogenization.

In a comparative study of Böttcher et al. (2015), it was found that the pulse length of mid-infrared laser ablation has a primary influence on tissue integrity [51, 52]. A heat rise up to 200 K was observed after irradiating tissue samples with MIRL, whereas PIRL ablation resulted in a negligible temperature increase of 5 K [52]. Moreover, the ablation with MIRL resulted in a damage zone of $\sim 800 \mu\text{m}$ and less amount of viable cells were found in the surrounded tissue [53]. In contrast, thermal or shock-wave damages to the ambient tissue and biomolecules are minimized in PIRL ablation since the thermal and acoustic energy confinement is achieved resulting in less collateral damage [47]. For most types of laser-tissue interactions, the thermal relaxation time is in the order of a few microseconds [54]. MIRL ablation is based on pulse durations in the range of several hundred microseconds, thus up to six orders of magnitude longer than for PIRL. Therefore, neither the thermal nor the acoustic energy of laser pulses can be confined causing leakage of thermal and acoustic energy out of the irradiated volume [55, 56]. When PIRL and MIRL homogenates of renal tissue were tested for retaining enzymatic activity by incubating with angiotensin I it was found that enzymatic activity was detectable in the PIRL homogenate but not for MIRL homogenized samples. It was concluded that not only the tissue integrity is influenced when MIRL is applied, but also causes denaturation of proteins and thereby inactivation of enzymes in the tissue [57].

In parallel to the studies performed with PIRL and MIRL, the group of Kermit Murray applied NIRL-based tissue sampling and homogenization. Their findings demonstrated that NIRL ablation is an appropriate method for the intact release of DNA [58] and RNA [59] molecules from tissue samples. In addition, enzyme activity was detectable in the NIRL homogenate, thus proving that no denaturation of proteins takes place [60]. Based on this, NIRL ablation was found to be similarly soft as PIRL. NIRL operates with pulse length in the lower nanosecond range, whereby thermal but no acoustic confinement is achieved. The ablation by both lasers lead to cold vaporization of tissues with the difference that tissue irradiation with PIRL results in slightly smaller damage zones. This is possibly due to less thermal effects through

picosecond impulsion and leakage of acoustic energy when using pulse width in the nanosecond range [54].

In another application, mid-infrared laser ablation was utilized in combination with ambient mass spectrometry. While Isabelle Fournier invented the NIRL-based SpiderMass Technology [61], Arash Zarrine-Afsar developed PIRL-MS [62]. Both methods are fiber-based and equipped with a handheld, where the aerosol can be directly transferred to the mass spectrometer (MS) by PTFE tubing. During NIRL ablation the biomolecules are already ionized and can be therefore directly analyzed by mass spectrometry. This process is described as water assisted laser desorption and ionization (WALDI) [63]. In contrast, the PIRL-MS technique requires post-ionization. The successful application of mid-infrared laser ablation combined with real-time MS analysis was shown in several studies, e.g. in the differentiation of oral tongue squamous cell carcinoma and nontumor regions [64] or for the identification of different medulloblastoma subgroups [65] and skin cancer types [66].

4 AIM AND RESEARCH OBJECTIVES

In recent years, there has been a significant increase in the number of mass spectrometry-based spatial omics studies. Despite the growing demand, there is currently a lack of suitable workflows that simultaneously preserve the spatial information inherent in the three-dimensional tissue structure during sample collection and achieve comprehensive coverage in the subsequent proteome and lipidome analysis.

This work aims to develop an advanced methodology for three-dimensional spatial omics based on nanosecond infrared laser (NIRL) ablation in combination with low-input mass spectrometric analysis.

Over the past decade, short pulse mid-infrared laser ablation has emerged as an innovative method for simultaneous tissue sampling and homogenization in mass spectrometric omics. Biomolecules are released from their cellular tissue compartments via a gentle and cold vaporization process. Moreover, this technology preserves the spatial information of the sample location and provides high precision by maintaining the integrity of the surrounding tissue area.

Given that the typical sample processing workflows for bottom-up proteomics and shotgun lipidomics of biological tissues necessitate the use of tissue amounts of several milligrams for robust processing and optimal results, the primary objective is to develop streamlined workflows, in which miniaturized tissue amounts of 0.5-1 mg corresponding to the typical size of a tissue biopsy are sampled and homogenized by NIRL. Thereafter, they are processed by improved sample preparation protocols for low-input amounts. The results of mass spectrometry-based differential quantitative bottom-up proteomics and shotgun lipidomics are assessed to ascertain the reproducibility and comprehensiveness of the analysis. Accordingly, the suitability of the developed sample processing protocols for the sampled tissue volumes in terms of the scale will be verified. The second research objective is to further develop the methodology for performing spatially resolved omics using the previously demonstrated size of tissue voxels, sufficient for global analysis with high coverage. To this end, NIRL-based spatial tissue sampling will be employed to obtain tissue volumes from different tissue regions and in a layer-by-layer manner. The samples are subjected to further processing using the previously enhanced bottom-up proteomics workflow. Based on the spatially resolved proteomics data obtained, it will be evaluated whether different functional and cellular regions can be distinguished. Finally, this will determine whether the methodological evolution of NIRL-based spatial tissue sampling in conjunction with optimized sample processing of low-input amounts for mass spectrometric analysis can be successfully applied for 3D spatial omics.

5 CUMULATIVE PART

The results of this thesis are presented below in the form of scientific publications. The contributors are listed in the author's details and collaboration with other institutes is indicated in the corresponding publications. The publications were published in the International Journal of Molecular Sciences (IJMS) and Analytical Chemistry.

5.1 TISSUE SAMPLING AND HOMOGENIZATION IN THE SUB-MICROLITER SCALE WITH A NANOSECOND INFRARED LASER (NIRL) FOR MASS SPECTROMETRIC PROTEOMICS

Jan Hahn*, Manuela Moritz*, Hannah Voß, Penelope Pelczar, Samuel Huber and Hartmut Schlüter

Int. J. Mol. Sci. **2021**, *22*, 10833

*Shared first authorship

In this study, a newly developed workflow for bottom-up proteomics of NIRL-ablated tissue samples was tested. Therefore, murine spleen and intestine were used as tissue models reflecting soft and muscle-rich tissue types. NIRL ablation was performed in a reflection geometry to allow sampling from intact tissue specimens. In contrast to previous studies, the resulting aerosol was captured directly on a microscope slide placed slightly above the ablated tissue sample, thus minimizing sample loss during the aerosol transport. Based on the results of the optical coherence tomography (OCT) measurements, the ablated volume was determined to be $1.1 \times 1.1 \times 0.4 \text{ mm}^3$, which corresponds to a tissue volume of approximately 500 nL. The condensed sample aerosol was subsequently processed by sodium deoxycholate (SDC)-assisted tryptic digestion and analyzed by liquid chromatography-tandem mass spectrometry (LC-MS/MS). The developed workflow for differential quantitative bottom-up proteomics revealed a total of 1,889 proteins in NIRL-ablated murine spleen and colon samples. As illustrated in the scatter plot visualization of the principal component analysis (PCA) results, a distinct separation between the two tissue types was evident. Furthermore, the tight clustering of technical replicates demonstrated the high reproducibility of the method. Student's t-testing underlined these findings. In total, 241 proteins were found to be significantly differentially abundant ($p < 0.05$, 1.5 fold change) when comparing murine spleen and colon samples. To prove that these differences were not due to different tissue behavior during the sampling and homogenization with NIRL, the abundance of so-called housekeeping proteins was compared for both tissue types. These proteins belong to the basic inventory of cells, and therefore have a uniform protein abundance in different tissue types. While the abundances of selected housekeeping proteins were found to be almost similar for the soft and muscle-rich tissues, several tissue-specific proteins were analyzed with higher abundance in the respective tissue type.

The findings of this study confirm the efficacy of NIRL-based tissue sampling and homogenization for soft and muscle-rich tissues. The proteomic data obtained displayed characteristic proteomic signatures for spleen and colon tissue, indicating that miniaturized tissue volumes of approximately 500 nL are sufficient to reach the depth and coverage required for a reasonably comprehensive interpretation in proteome analysis.



Article

Tissue Sampling and Homogenization in the Sub-Microliter Scale with a Nanosecond Infrared Laser (NIRL) for Mass Spectrometric Proteomics

Jan Hahn ^{1,*},[†] , Manuela Moritz ^{1,†} , Hannah Voß ¹, Penelope Pelczar ², Samuel Huber ² and Hartmut Schlüter ¹

¹ Section/Core Facility Mass Spectrometry and Proteomics, University Medical Center Hamburg-Eppendorf (UKE), Martinistr. 52, 20246 Hamburg, Germany; ma.moritz@uke.de (M.M.); ha.voss@uke.de (H.V.); h.schluet@uke.de (H.S.)

² Section of Molecular Immunology and Gastroenterology, I. Department of Medicine, University Medical Center Hamburg-Eppendorf (UKE), Martinistr. 52, 20246 Hamburg, Germany; p.pelczar@uke.de (P.P.); s.huber@uke.de (S.H.)

* Correspondence: ja.hahn@uke.de; Tel.: +49-1522-2827-168

† These authors contributed equally to this work.

Abstract: It was recently shown that ultrashort pulse infrared (IR) lasers, operating at the wavelength of the OH vibration stretching band of water, are highly efficient for sampling and homogenizing biological tissue. In this study we utilized a tunable nanosecond infrared laser (NIRL) for tissue sampling and homogenization with subsequent liquid chromatography tandem mass spectrometry (LC-MS/MS) analysis for mass spectrometric proteomics. For the first time, laser sampling was performed with murine spleen and colon tissue. An ablation volume of $1.1 \times 1.1 \times 0.4 \text{ mm}^3$ (approximately $0.5 \mu\text{L}$) was determined with optical coherence tomography (OCT). The results of bottom-up proteomics revealed proteins with significant abundance differences for both tissue types, which are in accordance with the corresponding data of the Human Protein Atlas. The results demonstrate that tissue sampling and homogenization of small tissue volumes less than $1 \mu\text{L}$ for subsequent mass spectrometric proteomics is feasible with a NIRL.

Keywords: tissue sampling; tissue homogenization; nanosecond infrared laser; laser ablation; proteomics; mass spectrometry



Citation: Hahn, J.; Moritz, M.; Voß, H.; Pelczar, P.; Huber, S.; Schlüter, H. Tissue Sampling and Homogenization in the Sub-Microliter Scale with a Nanosecond Infrared Laser (NIRL) for Mass Spectrometric Proteomics. *Int. J. Mol. Sci.* **2021**, *22*, 10833. <https://doi.org/10.3390/ijms221910833>

Academic Editor: Nagib Ahsan

Received: 25 August 2021

Accepted: 2 October 2021

Published: 7 October 2021

Publisher's Note: MDPI stays neutral with regard to jurisdictional claims in published maps and institutional affiliations.



Copyright: © 2021 by the authors. Licensee MDPI, Basel, Switzerland. This article is an open access article distributed under the terms and conditions of the Creative Commons Attribution (CC BY) license (<https://creativecommons.org/licenses/by/4.0/>).

1. Introduction

In mass spectrometry-based proteomic analysis of tissues, sampling and homogenization is one of the most challenging steps, aiming at a complete release and solubilization of all proteins present in the cells and their compartments within the intact tissue before its sampling and homogenization [1]. In particular, structural interactions of proteins and the formation of macromolecular assemblies make it challenging to fully solubilize proteins from tissue [2]. When choosing a method for homogenization, the high degree of heterogeneity of the chemical properties of proteins should also be considered. This is particularly important in the analysis of tissues, where there are many different types of cells performing specific functions in the tissue [2,3]. Tissue homogenization can be divided into two steps: tissue disruption and cell lysis [2]. Common methods for tissue disruption are mechanical homogenization, including vortexing and grinding with different beads, sonication, pressure-cycling technology or liquid nitrogen treatment and subsequent grinding of the frozen tissue. In the second step of homogenization, detergents or physical methods, such as osmotic shock, mechanical blending, sonication, and/or freeze/thaw treatment can be used for cell lysis [2]. Depending on the particular aim of the analysis, a combination of detergents and mechanical methods is required for the homogenization of tissues. However, when choosing detergents, it is essential to ensure that they are suitable for chromatography and mass spectrometry (MS) and have no interfering or suppressing effect [2].

Furthermore, the duration of the applied homogenization method is also critical and often a very time-consuming process. To release the proteins from the intracellular compartments, tissue and cell lysis steps are applied during homogenization, which release proteases and other enzymes. These biological catalysts can lead to changes in post-translational modifications (PTMs) or even complete degradation of the proteins over time [3]. The PTMs of proteins play a significant role in many diseases. Therefore, if a tissue proteome is to be studied, it is even more important to be able to characterize the proteoforms as they are present in their native tissue environment. While there are many methods, such as using protease inhibitors, to prevent proteome changes due to proteolytic processes, these do not address all enzymes, resulting in at least partial conversion of proteoforms [4].

Pressure BioSciences Inc. has developed a pressure-cycling technology (PCT) for the extraction of proteins from cells and tissues. Cell lysis is caused by rapid alternating cycles of high and low pressures. In comparison to conventional homogenization techniques like the probe sonicator and bead mill, the reaction chambers are temperature-controlled, resulting in no excessive heat during homogenization, which could possibly lead to changes in PTMs [5].

Laser capture microdissection (LCM) represents another method for tissue sampling [6,7]. With this method, cells from a specific area in a tissue can be selected using a microscope and isolated from the tissue by a near-infrared laser energy pulse, transferring it to an adhesive polymer film [3,8]. Next, the polymer is removed from the tissue with the bound cells of interest attached. With appropriate extraction buffers, the cells are released from the polymer surface and the proteins can be subjected to proteolytic digestion for bottom-up proteomics [8]. The advantage of this method is the possibility of selecting cell areas of interest after examination of the tissue section via the microscope, which is particularly useful in clinical applications, for example to distinguish tumor tissue from benign tissue [3]. However, this method is quite time-consuming and can only be applied to two-dimensional tissue sections. Stacking of sequential sections for a three-dimensional view is possible, but very challenging and expensive.

A novel approach for tissue sampling emerged from irradiation with an infrared laser (IR) emitting light at a wavelength of 2.94 μm . The energy of the IR laser is absorbed by water molecules and immediately converted into translational energy caused by the vibrational motion of their OH stretch band, resulting in an explosion of the irradiated water molecules, which leads to the decomposition of the tissue and thereby to the transfer into the gas phase [9]. In the case of the picosecond infrared laser (PIRL) the transfer of the energy of PIRL into translational energy is much faster than the transfer into thermal energy [10–12]. Because of this process, tissue irradiated with PIRL is transferred into an aerosol by cold vaporization [13].

The tissue aerosol represents an ideal homogenate, which can be used for subsequent analytical approaches such as mass spectrometric proteomics. Compared to mechanical homogenization, this is a very gentle method of sample extraction and homogenization, avoiding time-consuming preparation steps. Over the past decade, this tissue sampling and homogenization has been successfully demonstrated with a PIRL, nanosecond infrared laser (NIRL) and even a high-energy microsecond infrared laser (MIRL) with subsequent mass spectrometric proteomics [4,14–21] or directly coupled to real-time MS instruments, such as the “SpiderMass” technology [22–26].

In our previous studies we utilized a picosecond infrared laser (PIRL) [4,13,16,19] as well as a microsecond infrared laser (MIRL) [15,16] for tissue sampling and homogenization for subsequent proteomics and lipidomics. In a first study by Kwiatkowski et al. (2015), it was shown that tissue sampling with the PIRL makes proteins accessible in a wide range from a few kilodaltons to several million daltons. Furthermore, it was demonstrated that post-translational modifications like glycans of glycoproteins were not lost by PIRL ablation. Kwiatkowski et al. also confirmed that proteins are not denatured during PIRL ablation, since enzymatic activity was detectable after irradiation of samples with PIRL [13].

Kwiatkowski et al. (2016) focused on the investigation of proteoforms in tissues. Using human tonsil and rat pancreas tissue, a comparison of mechanical homogenization (cryogrinder or bead mill with 3 mm stainless steel beads) with PIRL ablation showed that the latter contained much more intact proteoforms and a larger number of identified proteins than the mechanical homogenate. Thus, tissue sampling with the PIRL laser yields not only a higher number of identified proteins, but also access to the intact proteoforms as they exist in the intact tissue [4].

In the study of Hänel et al. (2018), the MIRL was demonstrated as a further method for tissue sampling for mass spectrometric proteomics. In that work, for the first time an IR laser was used for tissue sampling of xenograft primary tumors and paired spontaneous metastases. In contrast to PIRL, MIRL is based on much longer pulse durations during laser ablation, ranging within microseconds rather than picoseconds. Based on mass spectrometry proteomic analysis of the MIRL ablated ovarian and liver metastases, some new presumed drivers in metastasis formation were identified, which may be used as new targets for functional studies [15].

In a publication by Krutilin et al. (2019), the PIRL and MIRL were directly compared. Muscle, liver, and kidney tissues of rats were examined. Krutilin et al. showed that both laser systems are suitable for tissue sampling and homogenization. A larger yield of proteins, identified by bottom-up proteomics, was obtained with the PIRL for liver tissue and with the MIRL for muscle tissue. Regarding the enzymatic activity of the proteins based on ablated kidney tissue, it was shown that proteins are denatured during tissue sampling with the MIRL, whereas the PIRL ablation had no denaturing effect. Due to the six orders of magnitude longer pulse duration and a much higher pulse energy, MIRL ablation heats the tissue causing denaturation of proteins in the cells neighboring the zone of ablated cells [16].

In this study, we applied the NIRL for the first time for the sampling of colon and spleen tissue. Unlike previous work, our laser setup is based on a wavelength tuneable NIRL with a pulse duration of about 7 ns. Just like PIRL and MIRL, the water molecules in tissue are excited by using a laser wavelength at the absorption peak of water around 2.94 μm . Highly energetic excitation of the OH vibrational stretching band transfers the sampled tissue into the gas phase, forming a plume of homogenized aerosol. In our setup, we utilize glass cover slips, which are placed slightly above the tissue during sampling to collect the plume as a condensate. In contrast to our previous studies, this approach reduces material loss by avoiding tubing and therefore allows lower sampling amounts, which increases the spatial resolution of the sampling location in the tissue. Our new setup represents an improvement in terms of miniaturization of tissue sampling towards an ablation volume of approximately 0.5 μL , which is roughly the size of a steel pinhead.

2. Results

A nanosecond infrared laser was used to sample fresh-frozen murine colon ($n = 3$) and spleen ($n = 3$) tissue with a beam scanning ablation setup, depicted in Figure 1a. The condensate of the tissue plume was collected by placing a glass cover slip directly over the sample during ablation, shown in Figure 1b,c. The divergent beam of a NIRL system is reflected via a silver mirror into a telescope, consisting of two focusing lenses, for collimation. A focusing lens of 150 mm focal length in combination with a two-axis scanning mirror was used to scan the sample on a manual stage, equipped with a cooling element ($-15\text{ }^{\circ}\text{C}$). The scanning mirror is controlled by two analog signal lines of an input/output card connected to a computer. A glass cover slip on a manual three-axis stage is placed 2–4 mm above the ablation site to collect the aerosol. The tissue aerosol is condensed onto the glass cover slip. Within the area of the condensate, a square of the size of the ablation area, is missing after condensation. The condensate in that area was removed by the laser beam.

Based on the 3D imaging by optical coherence tomography (OCT), image processing and segmentation, shown in Figure 1d,e, a mean ablation volume of $0.43 \pm 0.06 \mu\text{L}$ was determined for tissue sampling; this example was performed on formalin-fixed spleen tissue ($n = 3$) for better handling. Furthermore, mean ablation dimensions for central width and depth were determined with the provided tools of the used segmentation software (Figure 2) to measure about 1.1 mm and 0.4 mm, respectively. In Table 1 we show the separate numbers of the ablation volumes and dimensions for the three ablation sites.

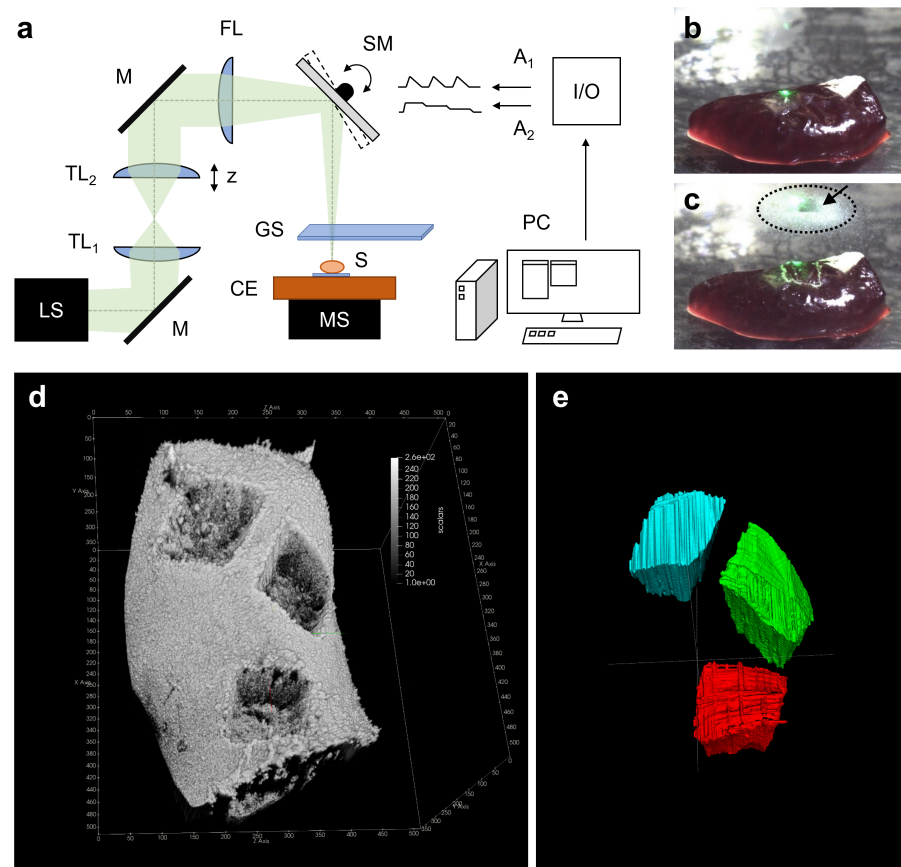


Figure 1. (a) Schematic of the ablation setup. Green: divergent beam; LS: NIRL laser system; M: silver mirror; TL₁, TL₂: telescope lenses; FL: focusing lens (of 150 mm focal length); SM: two-axis scanning mirror; S: scanning of the sample; MS: manual stage; CE: cooling element ($-15\text{ }^{\circ}\text{C}$); I/O: input/output card; A₁, A₂: analog control signals; PC: computer. GS: glass cover slip; (b,c) Photos of the tissue before and after irradiation; (c) Dashed ellipse: Condensed tissue aerosol. Arrow: indicating an area of lost condensate. Green light: pilot laser (532 nm wavelength); (d) Rendered 3D OCT image of the reference ablations on formalin-fixed murine spleen for ablation volume measurement purposes with the open-source application ParaView 5.9.1 [27]; (e) Manually segmented ablation volumes (with the labels red, blue, green) in the open-source software ITK-Snap 3.8.0 [28].

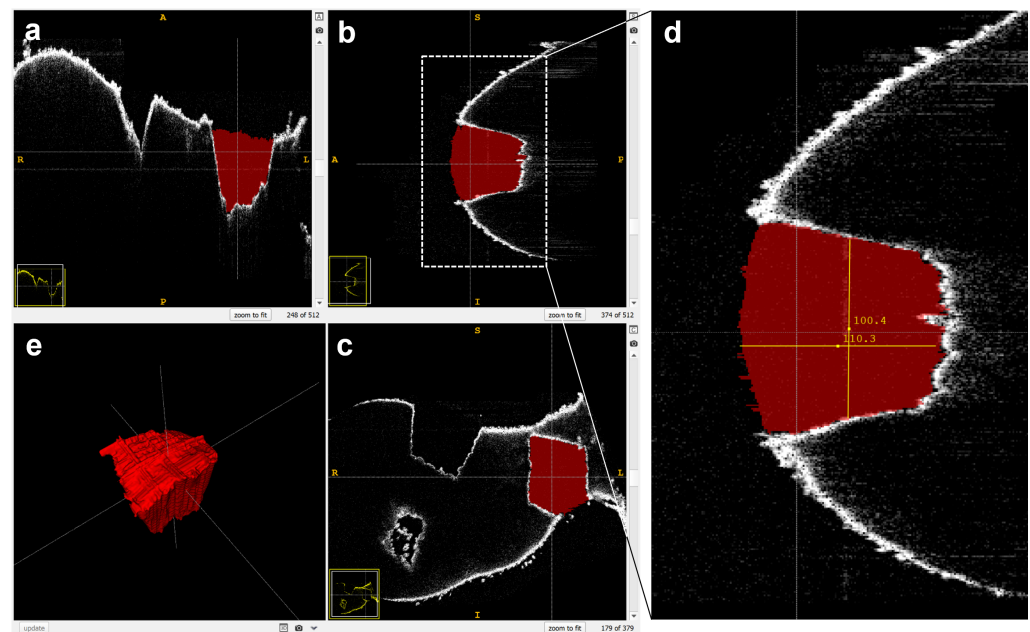


Figure 2. Example of 3D segmentation of an ablation site with the open-source software ITK Snap 3.8.0 [28]. (a–c) Slice views of the three dimensions; (d) Determination of the mean volume dimensions in pixels with the integrated measuring tool; (e) 3D rendering of the segmented volume.

Table 1. Ablation volumes and dimensions of the three ablation sites of a formalin-fixed murine spleen, determined with optical coherence tomography (OCT) for reference. Volume was determined based on the voxel count and the dimensions (mean width and depth) based on random distance measurements of the segmentation.

Ablation Site † [Label Color]	Ablation Volume [μL]	Mean Width [μm]	Mean Depth [μm]
Red	0.38	1,148	397
Green	0.53	1,205	401
Blue	0.40	1,091	404

† Labels are shown in Figure 1e.

Differential quantitative proteome analysis of the murine colon tissue and the spleen tissue (three biological replicates from each tissue) sampled with NIRL resulted in 1889 identified proteins (see Supplementary Tables S1 and S2), wherein a total of 501 proteins had quantitative data in all samples. In Figure 3, the results of a principal component analysis (PCA) (see Supplementary Table S3) are shown as scatter plot visualization, where component 1 (73.4%) is plotted against component 1 (73.4%). The PCA of the 501 proteins revealed a clear tissue-related distinction between colon and spleen samples based on component 1. Thus, the biological differences between the samples based on the different tissue types have the greatest influence. The biological replicates within a sample group play a subordinate role, as they show a low Euclidean distance in the scatter plot visualization of PCA, representing a high grade of similarity. This is also shown by the further results of the PCA, which show that only an explained variance of 14.7% could be calculated for component 2.

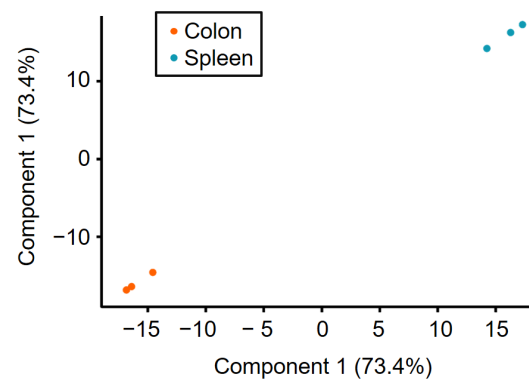


Figure 3. Scatter plot visualization of three murine colon (orange) and spleen (blue) tissue samples, showing component 1 against component 1 of PCA. The visualized data is based on 501 proteins with quantitative information for all samples (see Supplementary Table S3).

T-testing results (see Supplementary Table S4) are displayed as a volcano plot in Figure 4 showing the $-\log_{10} p$ -value against the \log_2 fold change between spleen and colon. The plot is based on 715 proteins, which have only two of three valid values per tissue type. Of these, 466 proteins (shown in black) have no *t*-test significance (p -value > 0.05) are shown in black. Based on the size of their change in abundance, *t*-test significant proteins (p -value < 0.05) can be divided in three different groups. Wherein 131 significant proteins with 1.5-fold higher abundance in the colon are shown in orange and 110 proteins with 1.5-fold higher abundance in the spleen are colored in blue. Significant proteins with an abundance difference less than 1.5-fold are shown in grey.

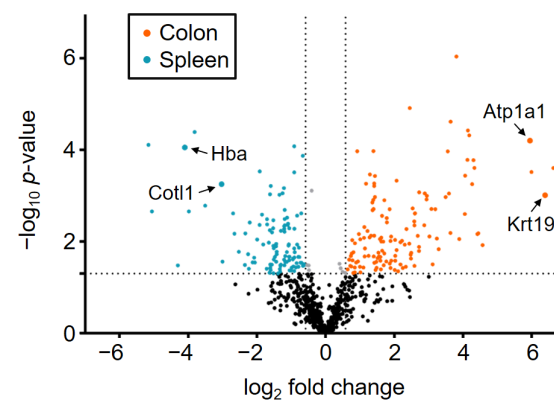


Figure 4. Volcano plot showing the \log_2 fold change values of 715 proteins plotted against their associated $-\log_{10} p$ -values. Dots representing individual proteins were divided in four different groups: p -value > 0.05 (black); p -value < 0.05 (grey); p -value < 0.05 , 1.5-fold higher abundance in colon (orange); p -value < 0.05 , 1.5-fold higher abundance in spleen (blue). For both sample groups two proteins, being typical higher abundant in colon or spleen tissue, respectively are highlighted and named (see Supplementary Table S4).

As expected, there are proteins with characteristic abundance in colon and spleen tissue, respectively. These proteins are visible in the volcano plot in Figure 4 as colored dots. Proteins with similar abundances cover about 65% of the colon and spleen tissues. These proteins belong to the basic inventory which every cell requires, independently from its specialization. In the study of Lee et al. (2016) a list of 20 newly identified housekeeping proteins was published showing a uniform protein abundance level (CV $< 20\%$, < 1.5 -fold change) over 27 different tissue types [29]. In Figure 5 a relative protein abundance plot is shown for four examples of these housekeeping proteins.

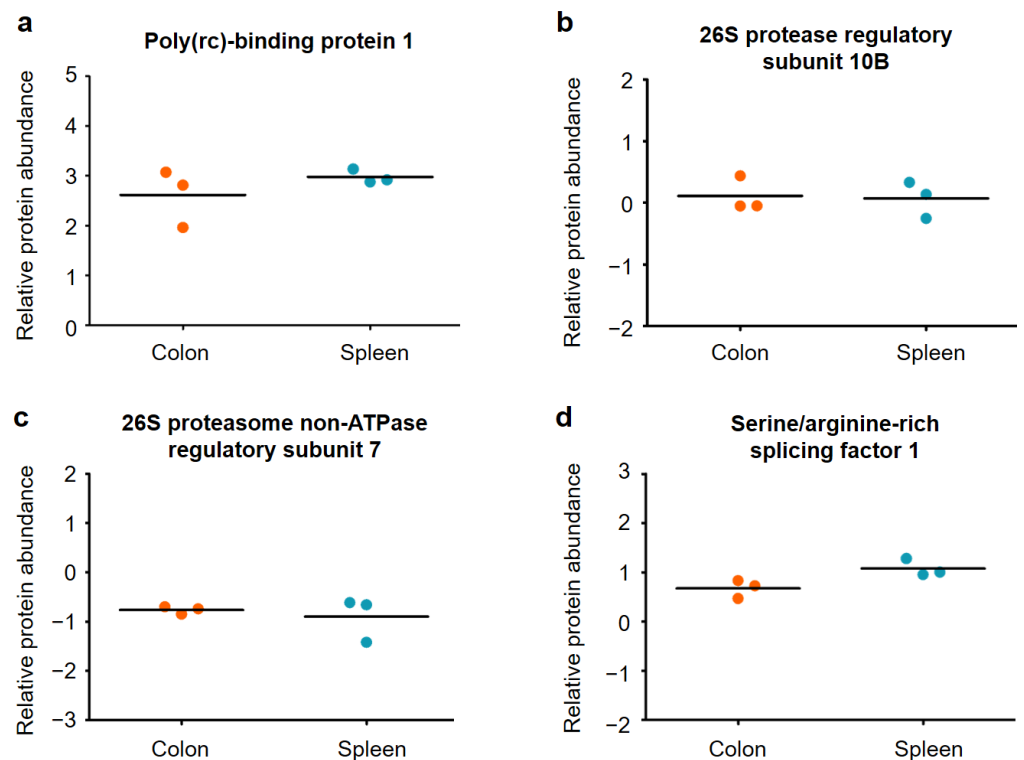


Figure 5. Relative protein abundance plots for (a) Poly(rC)-binding protein 1 (Pcbp1), (b) 26S protease regulatory subunit 10B (Psmc6), (c) 26S proteasome non-ATPase regulatory subunit 7 (Psmc7) and (d) Serine/arginine-rich splicing factor 1 (Srsf1) in murine colon and spleen samples. The data in (a–d) are highlighted in orange for colon tissue and in blue for spleen tissue.

Figure 5 shows very similar relative protein abundances for the colon and spleen samples for the four selected housekeeping proteins. Based on this, we can confirm that the specific differences between the colon and spleen samples are indeed due to significantly different protein abundances in the tissues and not due to, for example, different suitability of both organs for tissue sampling via NIRL. For further validation, two example proteins of each sample group with characteristic abundance in the respective tissues have been highlighted and named in Figure 4. For the colon tissue samples, the proteins hemoglobin subunit alpha (Hba) and coactosin like F-actin binding protein 1 (Cotl1) are significantly higher in abundance. The proteins Keratin, type I cytoskeletal 19 (Krt19) and sodium/potassium-transporting ATPase subunit alpha-1 (Atp1a1) show a 1.5-fold higher abundance in spleen tissue compared to the colon tissue samples. For these proteins, the relative protein abundances are compared against the corresponding protein abundance data from the Human Protein Atlas version 20.1 (<http://www.proteinatlas.org>, accessed on 15 July 2020) [30] in the following Figures 6 and 7.

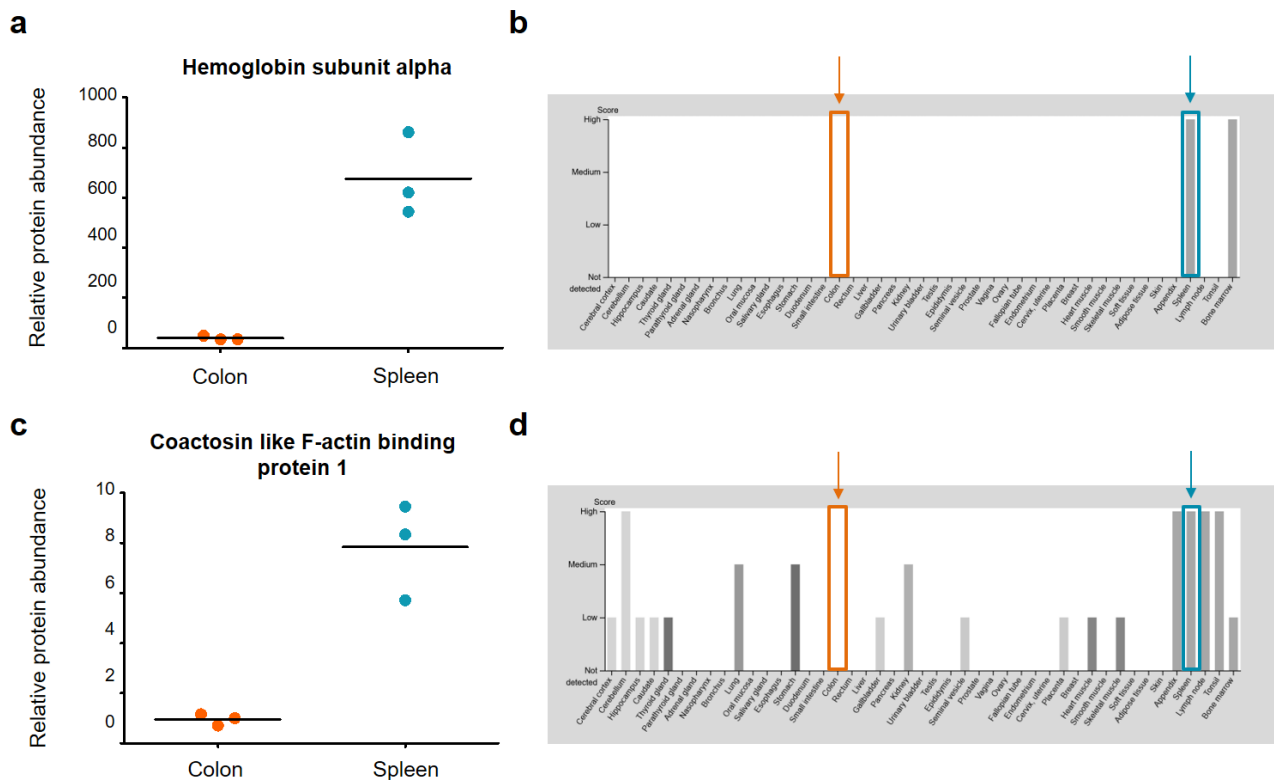


Figure 6. Relative protein abundance plots for (a) hemoglobin subunit alpha (Hba) and (c) coactosin like F-actin binding protein 1 (Cotl1) in murine colon and spleen samples. The corresponding protein abundance data of the Human Protein Atlas (HPA) [30] is shown in (b) for Hba and (d) for Cotl1. A total of 44 different tissue types were examined for the protein abundance data of the HPA. The data in (a,c) is highlighted in orange for colon tissue and in blue for spleen tissue. Images (b,d) are available from v20.1.proteinatlas.org.

The relative abundances of both proteins Hba and Cotl1 (see Supplementary Table S4) were plotted for the two different tissues, colon and spleen in Figure 6. Furthermore, the protein abundance data from the Human Protein Atlas for Hba and Cotl1 are shown. Both Hba and Cotl1 show significantly higher protein abundance in spleen than in colon tissue. In the “protein expression overview” of the Human Protein Atlas, the protein abundance data is shown for 44 tissues. Based on the “protein expression overview” for Hba and Cotl1 it is shown that a high abundance of both proteins is characteristic in human spleen tissue. Our results of significantly higher protein abundance of Hba and Cotl1 are corroborated by the human protein abundance data. A high abundance of Hba is characteristic for spleen tissue and bone marrow. In contrast, Cotl1 can be found with high abundances for several tissues such as appendix, lymph nodes and tonsil [30].

Figure 7 shows the relative protein abundance for the proteins Krt19 and Atp1a1 (see Supplementary Table S4) as well as the corresponding protein abundance data from the Human Protein Atlas for 44 tissues. Based on our results with these two example proteins, the relative protein abundance is higher in murine colon tissue than in spleen tissue. The protein abundance data from the Human Protein Atlas show that both Krt19 and Atp1a1 were detected with a high score in colon tissue, whereas no score could be calculated for spleen tissue, which is in accordance with our data. Furthermore, the data from the Human Protein Atlas shows that both proteins are not only highly abundant in colon tissue, but also in many other tissues such as kidney and appendix [30].

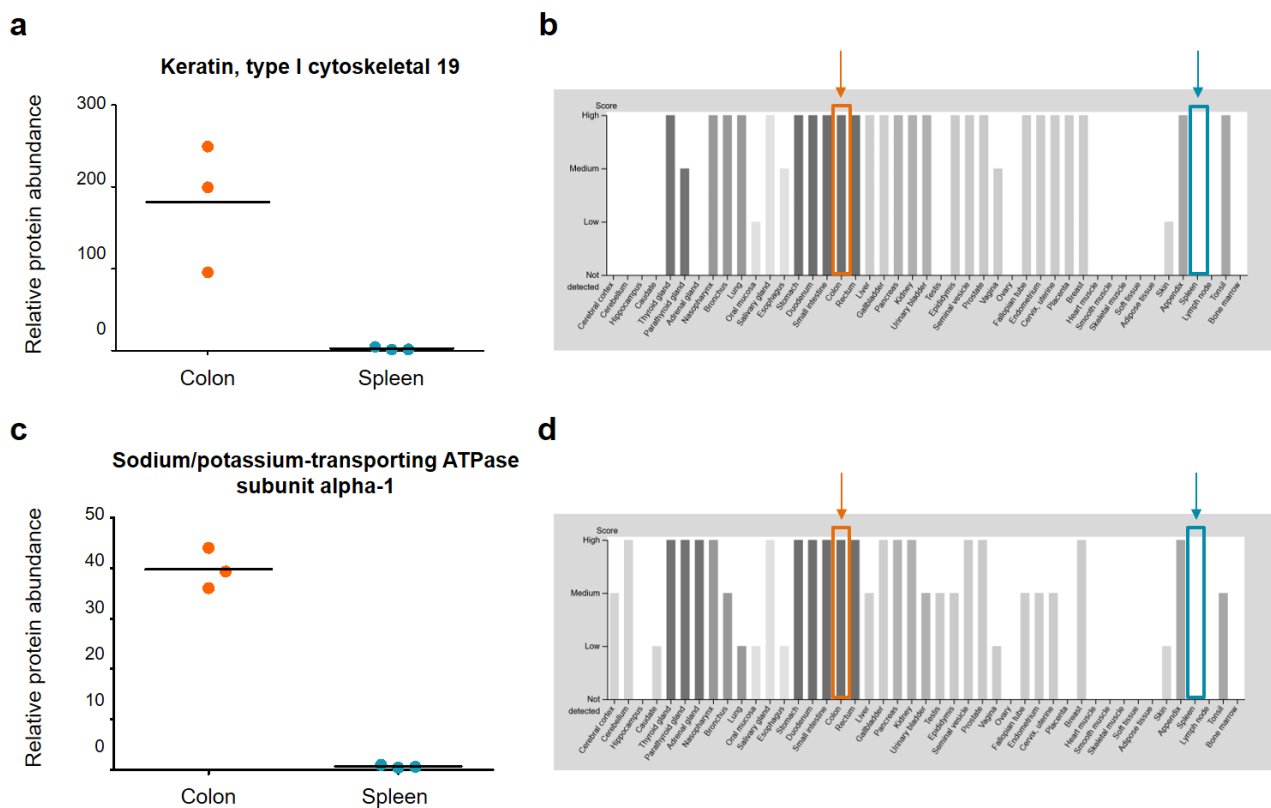


Figure 7. Relative protein abundance plots for (a) keratin, type I cytoskeletal 19 (Krt19) and (c) sodium/potassium-transporting ATPase subunit alpha-1 (Atp1a1) in murine colon and spleen samples. The corresponding protein abundance data of the Human Protein Atlas (HPA) [30] is shown in (b) for Hba and (d) for Cot11. A total of 44 different tissue types were examined for the protein abundance data of the HPA. The data in (a–d) is highlighted in orange for colon tissue and in blue for spleen tissue. Images (b,d) are available from v20.1.proteinatlas.org.

3. Discussion

In this study, we ablated three samples from fresh-frozen murine colon and spleen at different locations (ablation sites) with a volume of $1.1 \times 1.1 \times 0.4 \text{ mm}^3$ (approximately $0.5 \mu\text{L}$). The aerosol plume was condensed and then subjected to differential quantitative mass spectrometric bottom-up proteomics. A total number of 1889 proteins were identified with relative quantitative information, with 1617 proteins in the colon tissue samples and 1207 in the spleen tissue samples (see Supplementary Tables S1 and S2). The results of the differential quantitative proteome analysis display the expected proteomes of colon and spleen tissue and clearly demonstrate the applicability of NIRL for sampling tissues and immediate homogenization for proteomics.

In Table 2 we list ablation parameters and the number of identified proteins of this study together with data of other publications with similar experimental setups, utilizing infrared laser systems with the wavelength of the OH vibration stretching band of water at about $2.94 \mu\text{m}$ and subsequent LC-MS/MS analysis for mass spectrometric proteomics.

Since the number of identified proteins depends on the parameters of the sampling laser system, tissue type, sample collection approach, sample preparation steps, the applied MS instruments and algorithms for identification of the proteins, a comparison of the number of identified proteins of the different studies does not offer any information about the quality of the different IR-laser based sampling procedures. For instance, if we compared the yield of proteins from muscle tissue and renal tissue analyzed with the same bottom-up proteomics LC-MS/MS method, the total number of identified proteins of muscle tissue would usually be significantly lower, because of the ion suppression effect of high abundant proteins like myosin. For a meaningful comparison, a new study is required,

comprising all the different sampling approaches and using the same tissue followed by the same LC-MS/MS based proteomics strategy. Nevertheless, the listed studies show that sampling of different tissues with IR-lasers works well. To enable a higher spatial resolution of sampling of tissue with an IR-laser, the sample volume must be reduced further. With the latest mass spectrometers designed for single cell proteomics, sufficient numbers of identified proteins should be obtainable in the near future. This study, together with that of Wang et al. [21], are steps towards three-dimensional tissue sampling aiming for ultrahigh spatial resolution. Against this background, we want to highlight some aspects of the chronologically listed studies from Table 2, based on the identified proteins.

Table 2. Parameters and identified proteins of different studies sampling different tissues with an IR-laser with 2.94 μm wavelength and analyzing the samples with mass spectrometric bottom-up proteomics.

Author	Pulse Width Regime	Laser Fluence [J/cm^2]	Ablation Area [mm^2]	Ablation Depth [mm]	Ablation Volume [μL]	Tissue Type	Identified Proteins
Hahn et al. (this study)	ns	6.34	1.1×1.1	0.4	0.5	Colon (mouse) Spleen (mouse)	1617 1207
Pulukkody et al. 2021 [20]	ns	4.6 ± 2.1	2×2	unknown	unknown	Biofilm (plankton)	400
Wang et al. 2020 [21]	ns	2	7	0.01	0.07	Brain (rat)	720
			4		0.04	Midbrain (rat)	439
Krutilin et al. 2019 [16]	ms	40–60	4×4	unknown	unknown	Liver (rat) Muscle (rat)	581 883
	ps	1	4×4	unknown	unknown	Liver (rat) Muscle (rat)	926 642
Pettit et al. 2018 [17]	ns	2.7	2×2	0.05	0.2	Brain Q1 [†] (rat) Brain Q2 [†] (rat) Brain Q3 [†] (rat) Brain Q4 [†] (rat)	1674/393 [‡] 1723/379 [‡] 1322/326 [‡] 1575/365 [‡]
Hänel et al. 2018 [15]	ms	37.00	3×3	unknown	unknown	Tumor (mouse) Liver (mouse) Ovary (mouse)	1922 1811 2099
Kwiatkowski et al. 2016 [4]	ps	3.39	5×5	2	50	Pancreas (rat) Tonsils (human)	1743 2085
Donnarumma and Murray 2016 [14]	ns	3.00	1.2×1.1	0.05	0.066	Cerebellum (rat) Midbrain (rat)	250 95

[†] Q1–Q4 refer to different quadrants in the brain slice (thickness of 50 μm); [‡] Maximum of three ablated sections with/without ion mobility mass analyzer.

Compared to our previous studies [4,15,16] the total number of identified proteins are in the same order of magnitude, but with a significantly smaller ablation volume in this study. With regards to the study of Kwiatkowski et al. (2016) [4] the ablation volume was reduced 100-fold down to 0.5 μL . In the work of Kwiatkowski et al. (2016) and Hänel et al. (2018) [15] the aerosol was collected with a cooling trap or a glass fiber filter in combination with a vacuum pump. In this study we used a direct sampling approach in a reflection configuration, similar to studies from Park and Murray [31], who used a microscope slide to directly collect the ablated tissue in a transmission configuration for subsequent matrix-assisted laser desorption/ionization (MALDI) imaging. The increase of the efficiency of aerosol collection by the avoidance of aerosol transport tubing and the improvement of laser parameters of the NIRL setup are the main reasons for this progress. The main drivers for the improvement in the ratio of identified proteins to ablation volume are most likely the high beam quality factor ($M^2 = 2.5$), the relatively high applied laser fluence of the 7 ns pulses in combination with the low repetition rate (20 Hz), which minimizes heating.

The high yield of identified proteins in relation to the ablated volume in the study of Pettit et al. (2018) may be achieved because the authors used a mass spectrometer additionally equipped with an ion mobility (IM) mass analyzer. It was also shown, that the applied mass spectrometer yielded up to four times more identified proteins than tandem mass spectrometers without an IM [17].

In summary, it can be stated that high energy picosecond, nanosecond or even microsecond infrared lasers are sufficient for sampling tissues for subsequent bottom-up proteomics. The development of new highly sensitive mass spectrometers is opening the possibility to further decrease the tissue sampling volumes. Since in our new approach we ablate directly from the tissue and collect the sample in a reflection configuration, which enables us to sample in three dimensions (3D) we are not only capable of sampling in three dimensions (3D), but also making sure to always sample fully vaporized material. In contrast to a transmission configuration, there is a risk that material above the ablation area will also be blasted off [20]. Furthermore, we avoid material loss inside the tubing by not using aerosol transport system as described in our previous studies [4,15,16].

In the future, the technique described here may not only be the basis for basic research and investigation of small to even smaller amounts in the sub-nanoliter scale of tissues, but also for diagnostics in the sense of “precision pathology based on proteomics” giving the opportunity to apply high-resolution proteomics for patients [32].

4. Materials and Methods

4.1. Animals

Mice aged 8–12 weeks old used in this study were on a C57/BL6 background. Mice were kept under specific pathogen free conditions, at an ambient temperature of 20 ± 2 °C, humidity of $55 \pm 10\%$ and a dark/light cycle of 12 h.

4.2. Ablation Setup

The ablation setup is depicted in Figure 1a and consists of the following devices and optical elements. From the outlet of the pulsed nanosecond infrared laser (NIRL) (Opolette SE 2731, Oportek, LLC, Carlsbad, CA, USA) the beam passes a telescope with two plano-convex lenses (ISP-PX-25-150 and ISP-PX-25-100, ISP Optics Latvia, LTD, Riga, Latvia) for collimation purposes, followed by a 150 mm focusing lens (ISP-PX-25-150, ISP Optics Latvia, LTD, Riga, Latvia) resulting in an elliptical spot with the diameters $d_x = 165$ μm and $d_y = 135$ μm , respectively. The beam propagation ratio (M^2) of the NIRL is stated to be about 2.5 by the manufacturer. The spot dimensions were determined using a metal surface as target, colored with a paint stick, and measured with a microscope. A two-inch dual axis scanning mirror (OIM202, Optics in Motion LLC, Long Beach, CA, USA), controlled by a custom-built data acquisition input/output device, was used for transversal (x - and y -direction) focal displacement. The axial (z -direction) focal position can be adjusted by a slight movement of the second telescope lens. The scanning mirror is hit with an offset to the pivot point by the beam allowing the integration of a camera path for distance measurement purposes. The custom-made control software was timed to fit the repetition rate of the NIRL, which was set to the maximum of 20 Hz. Before each sampling procedure, a fresh glass cover slip (H 877, Carl Roth GmbH + Co. KG, Karlsruhe, Germany) was mounted 2–4 mm above the sample, to let the ablated aerosol condense against it during the ablation process.

4.3. Laser Parameters and Tissue Sampling

In this study the tunable wavelength of the NIRL was set to 2.9 μm , as a compromise of matching the strong OH vibration stretching band of water at 2.94 μm and to maximize the power output of the wavelength tuning range at 2.9 μm for the ablation process. The pulse energy was measured to be 560 μJ at the sample position, which corresponds to 11.2 mW at the used maximum repetition rate of 20 Hz. The scanning area was set in the custom control software to 1×1 mm² and the distance between spots to 200 μm . The

ablation time was set to 5 min for all ablations, resulting in 6,000 applied laser shots at each ablation site on the sample.

For this study we sampled three volumes from fresh-frozen murine colon, transversally cut and folded open, as well as fresh frozen murine spleen, with the temperature controlled to $-15\text{ }^{\circ}\text{C}$ during the ablation procedure. During ablation, the sampled tissue is transformed into a plume and immediately homogenized before condensing on the glass cover slip (see Figure 1b,c), where a scanning area of about $1 \times 1\text{ mm}^2$ of the collected condensate is lost due to the scanning of the laser beam.

The condensed homogenate was then collected in three steps, with a pipette filled with $50\text{ }\mu\text{L}$ of 0.1 M triethyl ammonium bicarbonate including 1% sodium deoxycholate (SDC buffer), from the unmounted glass cover slip after each ablation and transferred into a 1.5 mL Eppendorf tube. Afterwards, the samples (dissolved in $150\text{ }\mu\text{L}$ SDC buffer) were stored at $-80\text{ }^{\circ}\text{C}$ for further preparation steps.

4.4. Determination of the Ablation Volume

A formalin-fixed murine spleen was used as reference for ablation volume measurements to prevent sample deformation during the volume measurement procedure. The extracted volume was determined utilizing a spectral domain optical coherence tomography (OCT) system (OQ Labscope 2.0, Lumedica, Durham, NC, USA) with a central wavelength of 840 nm . The applied OCT imaging volume was $512 \times 512 \times 512$ voxels with each voxel measuring $11.48 \times 11.48 \times 3.61\text{ }\mu\text{m}^3$ in air. The OCT image data (see Figure 1d) was manually segmented with the open-source segmentation software ITK-Snap 3.8.0 [28] (see Figure 1e). For each ablation, the voxel count and mean volume dimensions (width and depth) were determined (see Figure 2a–e). The values for all three volumes of the reference ablations, including the mean width and depth for each ablation site are listed in Table 1.

4.5. Sample Preparation Protocol

The samples were boiled at $99\text{ }^{\circ}\text{C}$ for 5 min to denature proteins. Afterwards, samples were processed with a Probe Sonicator for one cycle at 30% power to destroy DNA and RNA molecules. According to a BCA protein assay (the PierceTM, Thermo Fisher Scientific, Waltham, MA, USA), $5\text{ }\mu\text{g}$ of each sample were diluted to $100\text{ }\mu\text{L}$ with SDC buffer. For reduction of disulfide bonded cysteine residues, 10 mM dithiothreitol (DTT) were added to the samples and they were incubated for 30 min at $60\text{ }^{\circ}\text{C}$. After that 20 mM iodoacetamide (IAA) was added to the samples for alkylation of the reduced cysteine residues and they were incubated for 30 min at $37\text{ }^{\circ}\text{C}$ in the dark. Trypsin was added at a ratio of 1:100 trypsin to protein for 16 h at $37\text{ }^{\circ}\text{C}$. To quench the trypsin and precipitate SDC, 100% formic acid was added to a final concentration of 1% formic acid *v/v*. The samples were centrifuged for 5 min at $16,000 \times g$. The supernatant was collected and dried in a SpeedVacTM vacuum concentrator. The digested samples were stored at $-20\text{ }^{\circ}\text{C}$ until further use.

4.6. Mass Spectrometric Analysis

The samples were resuspended in $20\text{ }\mu\text{L}$ of 0.1% FA for a final concentration of $0.25\text{ }\mu\text{g}/\mu\text{L}$. An aliquot of $4\text{ }\mu\text{L}$ was injected into a Dionex Ultimate 3000 UPLC system. Peptides were purified and desalted using an Thermo ScientificTM AcclaimTM PepMapTM 100 C18 Nano Trap pre-column ($100\text{ }\mu\text{m} \times 2\text{ cm}$, $100\text{ }\text{\AA}$ pore size, $5\text{ }\mu\text{m}$ particle size) and transferred to a Thermo ScientificTM AcclaimTM PepMapTM 100 C18 column ($75\text{ }\mu\text{m} \times 50\text{ cm}$, $100\text{ }\text{\AA}$ pore size, $2\text{ }\mu\text{m}$ particle size) for chromatographic separation. Peptide elution was achieved by applying an 80-minute run for each sample with a flow rate of $0.3\text{ }\mu\text{L}/\text{min}$ at $45\text{ }^{\circ}\text{C}$ using a gradient with Eluent A consisting of 0.1% FA and eluent B of 0.1% FA in 90% acetonitrile starting with 2% solvent B. Solvent B was increased to 30% in 65 min followed by a linear gradient elevating the concentration to 90% in 70 min. Finally, the concentration of buffer B was reduced to 2% after 70.1 min. The eluting peptides were analyzed on a Quadrupole Orbitrap hybrid mass spectrometer (QExactive, Thermo Fisher

Scientific, Waltham, MA, USA). Here, the ions that were responsible for the 15 highest signal intensities per precursor scan (1×10^6 ions, 70,000 resolution, 240 ms fill time) were analyzed by MS/MS (HCD at 25 normalized collision energy, 1×10^5 ions, 17,500 resolution, 50 ms fill time) in a range of 400–1200 m/z . A dynamic precursor exclusion time of 20 s was used.

4.7. MS Data Processing

Obtained raw data from the LC-MS/MS measurement of peptides were processed with MaxQuant (version 1.6.2.10). For protein identification, a reviewed murine Swissprot FASTA database without isoforms (status August 2020) containing 17,053 proteins was generated. The measured MS2 spectra were searched with the Andromeda algorithm against the theoretical fragment spectra of tryptic peptides from the data base. The carbamidomethylation of cysteine residues was set as a fixed modification. Oxidation of methionine, protein N-terminal acetylation and the cyclisation of N-terminal glutamine to pyroglutamate were set as variable modifications. Peptides with a minimum length of 6 amino acids and a maximum mass of 6000 Da were accepted with a mass tolerance of 10 ppm. Only peptides with a maximum of two missed trypsin cleavage sites were considered. The error tolerance was set to 20 ppm for the first precursor search and to 4.5 ppm for the following main search. Fragment spectra were matched with a 20 ppm error tolerance. Using a reverted decoy, the peptide database approach was set for protein identification to a false discovery rate (FDR) value threshold of <0.01. Label free quantification (LFQ) was performed with an LFQ minimum ratio count of 1. For quantification, all identified razor and unique peptides were considered. The label minimum ratio count was set to 1. Only unmodified peptides were used for quantification.

4.8. Statistical Data Analysis

Statistical analysis was performed using Perseus software (version 1.5.8.5). The quantitative data of 1889 proteins (see Supplementary Table S1) were transformed into \log_2 values and further median normalized per sample (see Supplementary Table S2). Principle component analysis (PCA) was performed for an overall sample amount of 6 samples including three murine colon and spleen samples. Therefore, protein data were filtered for no missing values resulting in 501 proteins (see Supplementary Table S3). Statistical testing between murine spleen and colon samples was performed using a two sample t -test based on 715 proteins, which were found in two of three samples per tissue type (see Supplementary Table S4). Only proteins identified with a p -value < 0.05 and a 1.5-fold change were considered as statistically significantly different in abundance among the compared groups. Resulting proteins of the two sample t -test (p -value < 0.05, 1.5-fold change) between colon and spleen were further analyzed using the Human Protein Atlas (status July 2021).

5. Conclusions

In our study we demonstrated the ablation of both murine colon and spleen tissue reproducibly with the NIRL. An ablation volume of $1.1 \times 1.1 \times 0.4 \text{ mm}^3$ was sampled, determined with OCT measurements. Based on the results of differential quantitative proteomics, colon and spleen samples could be clearly distinguished. A comparison of the relative abundances of two example proteins per tissue type was carried out. These proteins show significant abundance differences between both tissues and are in accordance with the corresponding Human Protein Atlas data. The yield of proteins is sufficient to identify proteins with significantly different protein abundance, which makes it suitable for biomarker identification approaches based on mass spectrometric proteomics. In conclusion, we demonstrate that a wavelength tunable NIRL is suitable for sampling prior to the differential proteomic analysis of tissues. Additionally, we show that the developed laser setup and aerosol collection method enables a miniaturized analysis, pointing towards spatially resolved proteomic analysis.

Supplementary Materials: The following are available online at <https://www.mdpi.com/article/10.3390/ijms221910833/s1>.

Author Contributions: Conceptualization, J.H., H.V., M.M., S.H. and H.S.; methodology, J.H. and H.V.; software and validation, J.H., H.V. and M.M.; formal analysis, H.V., M.M. and J.H.; investigation, J.H. and P.P.; resources, S.H. and H.S.; writing, J.H., M.M., H.V., H.S., P.P. and S.H. All authors have read and agreed to the published version of the manuscript.

Funding: This research was funded by the “Landesforschungsförderung” (LFF) of the city of Hamburg (grant number LFF-FV-75). This study was also partly supported by grants from the “Deutsche Forschungsgemeinschaft” (DFG) (INST 337/15-1, INST 337/16-1 and INST 152/837-1). Furthermore, this work was supported by intramural funding from the faculty.

Institutional Review Board Statement: The study was conducted according to the guidelines of the Declaration of Helsinki, and approved by the Institutional Review Board of “Behörde für Soziales, Familie, Gesundheit und Verbraucherschutz” (identification code ORG 934, date of approval: 5 October 2018, Hamburg, Germany).

Informed Consent Statement: Not applicable.

Data Availability Statement: Mass spectrometric data generated in this study can be accessed through the ProteomeXchange Consortium via the PRIDE partner repository with the dataset identifier PXD027700.

Acknowledgments: We thank the Max Planck Institute for the Structure and Dynamics of Matter for providing equipment and R.J. Dwayne Miller from the University of Toronto in Canada for his scientific support.

Conflicts of Interest: The authors declare no conflict of interest.

References

1. Liebler, D.C. *Introduction to Proteomics: Tools for the New Biology*; Humana Press: Totowa, NJ, USA, 2002.
2. Cañas, B.; Piñeiro, C.; Calvo, E.; López-Ferrer, D.; Gallardo, J.M. Trends in sample preparation for classical and second generation proteomics. *J. Chromatogr. A* **2007**, *1153*, 235–258. [[CrossRef](#)]
3. Mirzaei, H.; Carrasco, M. *Modern Proteomics—Sample Preparation, Analysis and Practical Applications*; Springer: Cham, Switzerland, 2016; Volume 919. [[CrossRef](#)]
4. Kwiatkowski, M.; Wurlitzer, M.; Krutilin, A.; Kiani, P.; Nimer, R.; Omidi, M.; Mannaa, A.; Bussmann, T.; Bartkowiak, K.; Kruber, S.; et al. Homogenization of tissues via picosecond-infrared laser (PIRL) ablation: Giving a closer view on the in-vivo composition of protein species as compared to mechanical homogenization. *J. Proteom.* **2016**, *134*, 193–202. [[CrossRef](#)] [[PubMed](#)]
5. Smejkal, G.B.; Robinson, M.H.; Lawrence, N.P.; Tao, F.; Saravis, C.A.; Schumacher, R.T. Increased protein yields from *Escherichia coli* using pressure-cycling technology. *J. Biomol. Tech.* **2006**, *17*, 173–175. [[PubMed](#)]
6. Berns, M.W.; Greulich, K.O. Laser manipulation of cells and tissues. In *Methods in Cell Biology*; Elsevier: Amsterdam, The Netherlands; Academic Press: Boston, MA, USA, 2007; Volume 82.
7. Murray, K.K.; Seneviratne, C.A.; Ghorai, S. High resolution laser mass spectrometry bioimaging. *Methods* **2016**, *104*, 118–126. [[CrossRef](#)] [[PubMed](#)]
8. Liu, B.C.S. Tissue proteomics: Pathways, biomarkers, and drug discovery. In *Methods in Molecular Biology*; Humana Press: Totowa, NJ, USA, 2008; Volume 441.
9. Cowan, M.L.; Bruner, B.D.; Huse, N.; Dwyer, J.R.; Chugh, B.; Nibbering, E.T.J.; Elsaesser, T.; Miller, R.J.D. Ultrafast memory loss and energy redistribution in the hydrogen bond network of liquid H₂O. *Nature* **2005**, *434*, 199–202. [[CrossRef](#)] [[PubMed](#)]
10. Franjic, K.; Miller, D. Vibrationally excited ultrafast thermodynamic phase transitions at the water/air interface. *Phys. Chem. Chem. Phys.* **2010**, *12*, 5225–5239. [[CrossRef](#)] [[PubMed](#)]
11. Bhardwaj, C.; Hanley, L. Ion sources for mass spectrometric identification and imaging of molecular species. *Nat. Prod. Rep.* **2014**, *31*, 756–767. [[CrossRef](#)]
12. Amini-Nik, S.; Kraemer, D.; Cowan, M.L.; Gunaratne, K.; Nadesan, P.; Alman, B.A.; Miller, R.J.D. Ultrafast mid-IR laser scalpel: Protein signals of the fundamental limits to minimally invasive surgery. *PLoS ONE* **2010**, *5*, e13053. [[CrossRef](#)]
13. Kwiatkowski, M.; Wurlitzer, M.; Omidi, M.; Ren, L.; Kruber, S.; Nimer, R.; Robertson, W.D.; Horst, A.; Miller, R.J.D.; Schlüter, H. Ultrafast extraction of proteins from tissues using desorption by impulsive vibrational excitation. *Angew. Chem.* **2015**, *54*, 285–288. [[CrossRef](#)]
14. Donnarumma, F.; Murray, K.K. Laser ablation sample transfer for localized LC-MS/MS proteomic analysis of tissue. *J. Mass Spectrom.* **2016**, *51*, 261–268. [[CrossRef](#)]

15. Hänel, L.; Gosau, T.; Maar, H.; Valentiner, U.; Schumacher, U.; Riecken, K.; Windhorst, S.; Hansen, N.O.; Heikau, L.; Wurlitzer, M.; et al. Differential Proteome Analysis of Human Neuroblastoma Xenograft Primary Tumors and Matched Spontaneous Distant Metastases. *Sci. Rep.* **2018**, *8*, 13986. [[CrossRef](#)]
16. Krutilin, A.; Maier, S.; Schuster, R.; Kruber, S.; Kwiatkowski, M.; Robertson, W.D.; Hansen, N.O.; Miller, R.J.D.; Schlüter, H. Sampling of Tissues with Laser Ablation for Proteomics: Comparison of Picosecond Infrared Laser and Microsecond Infrared Laser. *J. Proteome Res.* **2019**, *18*, 1451–1457. [[CrossRef](#)]
17. Pettit, M.E.; Donnarumma, F.; Murray, K.K.; Solouki, T. Infrared laser ablation sampling coupled with data independent high resolution UPLC-IM-MS/MS for tissue analysis. *Anal. Chim. Acta* **2018**, *1034*, 102–109. [[CrossRef](#)] [[PubMed](#)]
18. Mallah, K.; Quanicco, J.; Raffo-Romero, A.; Cardon, T.; Aboulouard, S.; Devos, D.; Kobeissy, F.; Zibara, K.; Salzet, M.; Fournier, I. Matrix-Assisted Laser Desorption/Ionization-Mass Spectrometry Imaging of Lipids in Experimental Model of Traumatic Brain Injury Detecting Acylcarnitines as Injury Related Markers. *Anal. Chem.* **2019**, *91*, 11879–11887. [[CrossRef](#)]
19. Wurlitzer, M.; Hessling, E.; Rinas, K.; Fuh, M.; Petersen, H.; Ricklefs, F.; Lamszus, K.; Regelsberger, J.; Maier, S.; Kruber, S.; et al. Mass Spectrometric Lipid Profiles of Picosecond Infrared Laser-Generated Tissue Aerosols Discriminate Different Brain Tissues. *Lasers Surg. Med.* **2020**, *52*, 228–234. [[CrossRef](#)]
20. Pulkukody, A.C.; Yung, Y.P.; Donnarumma, F.; Murray, K.K.; Carlson, R.P.; Hanley, L. Spatially resolved analysis of *Pseudomonas aeruginosa* biofilm proteomes measured by laser ablation sample transfer. *PLoS ONE* **2021**, *16*, e0250911, [[CrossRef](#)] [[PubMed](#)]
21. Wang, K.; Donnarumma, F.; Pettit, M.E.; Szot, C.W.; Solouki, T.; Murray, K.K. MALDI imaging directed laser ablation tissue microsampling for data independent acquisition proteomics. *J. Mass Spectrom.* **2020**, *55*, e4475. [[CrossRef](#)] [[PubMed](#)]
22. Park, S.G.; Murray, K.K. Infrared laser ablation sample transfer for on-line liquid chromatography electrospray ionization mass spectrometry. *J. Mass Spectrom.* **2012**, *47*, 1322–1326. [[CrossRef](#)] [[PubMed](#)]
23. Park, S.G.; Murray, K.K. Ambient laser ablation sampling for capillary electrophoresis mass spectrometry. *Rapid Commun. Mass Spectrom.* **2013**, *27*, 1673–1680. [[CrossRef](#)] [[PubMed](#)]
24. Fatou, B.; Saudemont, P.; Leblanc, E.; Vinatier, D.; Mesdag, V.; Wisztorski, M.; Focsa, C.; Salzet, M.; Ziskind, M.; Fournier, I. In vivo Real-Time Mass Spectrometry for Guided Surgery Application. *Sci. Rep.* **2016**, *6*, 25919. [[CrossRef](#)]
25. Ogrinc, N.; Saudemont, P.; Balog, J.; Robin, Y.M.; Gimeno, J.P.; Pascal, Q.; Tierny, D.; Takats, Z.; Salzet, M.; Fournier, I. Water-assisted laser desorption/ionization mass spectrometry for minimally invasive in vivo and real-time surface analysis using SpiderMass. *Nat. Protoc.* **2019**, *14*, 3162–3182. [[CrossRef](#)]
26. Ogrinc, N.; Saudemont, P.; Takats, Z.; Salzet, M.; Fournier, I. Cancer Surgery 2.0: Guidance by Real-Time Molecular Technologies. *Trends Mol. Med.* **2021**, *27*, 602–615. [[CrossRef](#)] [[PubMed](#)]
27. Henderson, A. *The ParaView Guide: A Parallel Visualization Application*; Kitware: Clifton Park, NY, USA, 2004.
28. Yushkevich, P.A.; Piven, J.; Hazlett, H.C.; Smith, R.G.; Ho, S.; Gee, J.C.; Gerig, G. User-guided 3D active contour segmentation of anatomical structures: significantly improved efficiency and reliability. *NeuroImage* **2006**, *31*, 1116–1128. [[CrossRef](#)] [[PubMed](#)]
29. Lee, H.G.; Jo, J.; Hong, H.H.; Kim, K.K.; Park, J.K.; Cho, S.J.; Park, C. State-of-the-art housekeeping proteins for quantitative western blotting: Revisiting the first draft of the human proteome. *Proteomics* **2016**, *16*, 1863–1867. [[CrossRef](#)]
30. Uhlén, M.; Fagerberg, L.; Hallström, B.M.; Lindskog, C.; Oksvold, P.; Mardinoglu, A.; Sivertsson, Å.; Kampf, C.; Sjöstedt, E.; Asplund, A.; et al. Proteomics. Tissue-based map of the human proteome. *Science* **2015**, *347*, 1260419. [[CrossRef](#)] [[PubMed](#)]
31. Park, S.G.; Murray, K.K. Infrared laser ablation sample transfer for MALDI imaging. *Anal. Chem.* **2012**, *84*, 3240–3245. [[CrossRef](#)] [[PubMed](#)]
32. Roehrl, M.H.; Roehrl, V.B.; Wang, J.Y. Proteome-based pathology: The next frontier in precision medicine. *Expert Rev. Precis. Med. Drug Dev.* **2021**, *6*, 1–4. [[CrossRef](#)]

5.2 LIPIDOME ANALYSIS OF OROPHARYNGEAL TUMOR TISSUES USING NANOSECOND INFRARED LASER (NIRL) TISSUE SAMPLING AND SUBSEQUENT MASS SPECTROMETRY

Rupert Stadlhofer*, Manuela Moritz*, Marceline M. Fuh, Jörg Heeren, Henrike Zech, Till S. Clauditz, Hartmut Schlüter, Christian S. Betz, Dennis Eggert, Arne Böttcher and Jan Hahn

Int. J. Mol. Sci. **2023**, 24, 7820

*Shared first authorship

This study presents a novel approach combining NIRL-based tissue sampling and shotgun lipidomics for the first time. The feasibility of the designed workflow was evaluated for the differential quantitative lipidome analysis of oropharyngeal squamous cell carcinomas (OPSCC) and non-tumorous mucosa samples. A total of eleven fresh-frozen oropharyngeal tissue samples from four different patients were subjected to analysis. As in the study conducted by Hahn & Moritz et al., tissue volumes of approximately 500 nL were sampled by NIRL. In this study, however, an ablation chamber was used, whereby the resulting aerosol was captured on a glass fiber filter. Subsequently, lipid extraction was performed prior to mass spectrometry-based quantitative shotgun lipidomics. Overall, 755 lipid species from 13 lipid classes were quantified. The data demonstrated not only intra- but also interpatient alterations in lipid composition. For instance, the healthy mucosa tissue samples, derived from either the tonsil or the base of the tongue (BOT), exhibited varying concentrations of triacylglycerides (TAG). However, irrespective of the sample origin, the concentration of TAG was consistently higher in the healthy mucosa samples than in the OPSCC samples from the same patient. In contrast, the lipid classes phosphatidylcholine (PC) and phosphatidylethanolamine (PE) were found to be present in higher concentrations in the OPSCC samples than in the respective non-tumorous oropharyngeal tissue. In the scatterplot visualization of the PCA results, OPSCC samples showed close clustering regardless of their origin, whereas the non-tumorous samples could be clearly distinguished, according to their respective BOT and tonsil origin. These findings confirm similarities in the lipid profiles of the OPSCC samples from different tumor locations, while also demonstrating that non-tumorous samples from the BOT and tonsil exhibit distinct lipid compositions. Finally, Welch's t-testing revealed the lipid species showing significantly different abundances when comparing OPSCC and healthy mucosa samples from the respective patient. In comparison to alternative techniques utilizing ambient mass spectrometry for real-time analysis, it was not only feasible to distinguish between oropharyngeal squamous cell carcinoma (OPSCC) and non-tumorous oropharyngeal tissue, but also to perform a comprehensive lipidome characterization of these distinct tissue types. The developed method, which combines NIRL-based tissue sampling with subsequent shotgun lipidomics, was successfully demonstrated to yield sufficient amounts for a reproducible mass spectrometry-based lipidome analysis with high coverage. This was achieved by sampling miniaturized tissue volumes of approximately 500 nL. The successful methodological developments in differential quantitative proteome analysis demonstrated in the study of Hahn & Moritz et al. and the quantitative shotgun lipidome analysis presented here provide a foundation for further development towards spatial omics.



Article

Lipidome Analysis of Oropharyngeal Tumor Tissues Using Nanosecond Infrared Laser (NIRL) Tissue Sampling and Subsequent Mass Spectrometry

Rupert Stadlhofer ^{1,*},[†] , Manuela Moritz ^{2,†} , Marceline M. Fuh ³, Jörg Heeren ³ , Henrike Zech ^{1,4}, Till S. Clauditz ⁵ , Hartmut Schlüter ² , Christian S. Betz ¹ , Dennis Eggert ¹, Arne Böttcher ^{1,*},[‡] and Jan Hahn ^{2,‡}

- ¹ Department of Otorhinolaryngology, University Medical Center Hamburg-Eppendorf, Martinistraße 52, 20246 Hamburg, Germany
- ² Section/Core Facility Mass Spectrometric Proteomics, Diagnostic Center, University Medical Center Hamburg-Eppendorf, Martinistraße 52, 20246 Hamburg, Germany; ma.moritz@uke.de (M.M.); ja.hahn@uke.de (J.H.)
- ³ Department of Biochemistry and Molecular Cell Biology, Center for Experimental Medicine, University Medical Center Hamburg-Eppendorf, Martinistraße 52, 20246 Hamburg, Germany
- ⁴ Mildred Scheel Cancer Career Center HaTriCS4, University Medical Center Hamburg-Eppendorf, Martinistraße 52, 20246 Hamburg, Germany
- ⁵ Department of Pathology, Diagnostic Center, University Medical Center Hamburg-Eppendorf, Martinistraße 52, 20246 Hamburg, Germany
- * Correspondence: r.stadlhofer@uke.de (R.S.); ar.boettcher@uke.de (A.B.); Tel.: +49-1522-2817641 (R.S.)
- † These authors contributed equally to this work and share first authorship.
- ‡ These authors contributed equally to this work and share senior authorship.



Citation: Stadlhofer, R.; Moritz, M., Fuh, M.M.; Heeren, J.; Zech, H.; Clauditz, T.S.; Schlüter, H.; Betz, C.S.; Eggert, D.; Böttcher, A.; et al. Lipidome Analysis of Oropharyngeal Tumor Tissues Using Nanosecond Infrared Laser (NIRL) Tissue Sampling and Subsequent Mass Spectrometry. *Int. J. Mol. Sci.* **2023**, *24*, 7820. <https://doi.org/10.3390/ijms24097820>

Academic Editors: Marco Falasca and Carlo Agostoni

Received: 23 March 2023

Revised: 16 April 2023

Accepted: 21 April 2023

Published: 25 April 2023



Copyright: © 2023 by the authors. Licensee MDPI, Basel, Switzerland. This article is an open access article distributed under the terms and conditions of the Creative Commons Attribution (CC BY) license (<https://creativecommons.org/licenses/by/4.0/>).

Abstract: Ultrashort pulse infrared lasers can simultaneously sample and homogenize biological tissue using desorption by impulsive vibrational excitation (DIVE). With growing attention on alterations in lipid metabolism in malignant disease, mass spectrometry (MS)-based lipidomic analysis has become an emerging topic in cancer research. In this pilot study, we investigated the feasibility of tissue sampling with a nanosecond infrared laser (NIRL) for the subsequent lipidomic analysis of oropharyngeal tissues, and its potential to discriminate oropharyngeal squamous cell carcinoma (OPSCC) from non-tumorous oropharyngeal tissue. Eleven fresh frozen oropharyngeal tissue samples were ablated. The produced aerosols were collected by a glass fiber filter, and the lipidomes were analyzed with mass spectrometry. Data was evaluated by principal component analysis and Welch's t-tests. Lipid profiles comprised 13 lipid classes and up to 755 lipid species. We found significant inter- and inpatient alterations in lipid profiles for tumor and non-tumor samples (p -value < 0.05, two-fold difference). Thus, NIRL tissue sampling with consecutive MS lipidomic analysis is a feasible and promising approach for the differentiation of OPSCC and non-tumorous oropharyngeal tissue and may provide new insights into lipid composition alterations in OPSCC.

Keywords: nanosecond infrared laser; laser ablation; mass spectrometry; lipidomics; HNSCC; OPSCC; HPV

1. Introduction

Oropharyngeal squamous cell carcinomas (OPSCCs) are a subgroup of head and neck squamous cell carcinomas (HNSCCs) and were estimated to be responsible for 98,412 new cases (0.5% of total cancer incidence) and 48,143 deaths (0.5% of total cancer morbidity) worldwide in 2020 [1]. The current increase in human papillomavirus (HPV)-related OPSCC has countered the positive effects of global efforts to reduce other risk factors such as tobacco usage and alcohol, thus leading to rising incidence overall [2,3]. Compared to the traditional risk factors, HPV-related OPSCC is more prevalent in younger

patients and exhibits different biological behavior that tends to be less aggressive and have a better response to treatment [4]. Despite the ongoing development of new treatment strategies, the therapeutic handling of these malignancies remains challenging and requires a multidisciplinary approach [5,6].

Significant progress has been made in understanding the impact of lipid metabolism on cancer formation and progression. The dysregulation of lipid metabolism is known to contribute to the pathogenesis and progression of cancer. Alterations in lipid metabolism, including synthesis, uptake and storage, have been shown to support the growth, survival, and proliferation of cancer cells, as well as their ability to invade and metastasize. Therefore, the analysis of the lipid composition of tumor cells can provide insights into these mechanisms, thus indicating the high potential value of lipid-based molecular analysis of malignant diseases [7–11]. For this, several studies have also been focused on the lipidome analysis of HNSCCs to investigate alterations in lipid metabolism and identify potential biomarkers. However, HNSCCs originate from different anatomical regions such as the oral cavity, larynx, and pharynx. While lipidome analyses of SCCs of the oral cavity and larynx have been performed in previous studies [12–14], there is still a lack of knowledge about the lipidome for squamous cell carcinomas of the oropharynx (OPSCCs), thus highlighting the necessity of our study.

Mass spectrometry (MS)-based approaches are an essential tool for gaining comprehensive insights into cellular lipid profiles and their pathologic alterations [15,16]. Furthermore, adequate surgical removal of the tumor and, especially, the status of the surgical margin are important factors for individual outcomes in HNSCC, especially in terms of prognosis, adjuvant treatment, and quality of life [17,18]. In oncologic surgery, the differentiation of preservable healthy tissue versus diseased tissue that needs to be resected is usually performed intraoperatively. Even though the surgeon evaluates the tumor margins using preoperative imaging (size, shape, [micro]environment) there is a dependence on intraoperative tactile and visual information that is combined with the surgeon's experience [19–22]. The gold standard for confirming sufficient resection margins is an intraoperative pathologist consultation with frozen sections [17,23,24]. The overall adequacy of using intraoperative frozen sections is >95% in HNSCC cases, but there are several downsides to this technique [25]. In addition to being a time-consuming procedure with interpretation and sampling errors, there are also challenges associated with close margin situations (<5 mm) that can cause sensitivity to drop below 40% for resections of head and neck tumors, thereby leading to positive margins becoming apparent on postoperative histopathologic examination of the complete tumor specimen [23,26–29].

In the last two decades, great efforts have been made to improve surgical guidance by enhancing tissue characterization on a molecular level through MS-based approaches. In these techniques, MS is used to analyze the molecular information of a tissue sample and, in particular, to identify tissue-specific alterations in lipids and proteins. However, the techniques vary in the way the samples are obtained. The application of an electrosurgical knife (iKnife) [30], desorption electrospray ionization (DESI) [31,32], and liquid extraction surface analysis [33] have all been suggested as potential methods.

Ultrashort pulse mid-infrared lasers (IRL) with pulse widths in the picosecond or nanosecond regime are an alternative emerging technology for tissue sampling, whereby the ablation occurs via desorption by impulsive excitation (DIVE) [12,34–36]. The specific wavelength of 2940 nm targets O-H bonds in the tissue's water molecules. The energy from the laser is almost completely converted into translational energy caused by the vibrational motion of the symmetric O-H stretch band, rather than being transferred to the surrounding tissue by thermal or acoustic transport. The water molecules are driven into the gas phase in a much shorter time scale, thereby decomposing the irradiated tissue and preventing significant collateral damage in the neighboring structures [37–39]. Besides the resulting high cutting precision and significant superiority concerning wound healing and scar formation compared with other lasers, the application of DIVE generates an aerosol that is particularly suitable for subsequent differential quantitative proteomics

and lipidomics. Several studies have tested the function of real-time MS concepts for tissue differentiation [32,40,41]. Utilizing laser-based aerosolization [12,42,43] or tissue surface extraction [33] combined with real-time MS enables the characterization of different tissue pathologies (cancer, infection, or inflammation) within seconds based on lipid profile signatures. However, to classify the molecular profile of different tissue types, spectral libraries must be created, and the collected data has to be validated across a large population due to significant molecular heterogeneities in human cancer.

In a recent study, we demonstrated tissue sampling and homogenization using a nanosecond infrared laser (NIRL) for MS proteomics with high spatial resolution [44,45]. Here, we translate this knowledge to the field of head and neck tumors.

In this pilot study, we combined NIRL ablation-based tissue sampling with a shotgun lipidomics approach. By using lipid extraction prior to mass spectrometric measurement and differential mobility separation for targeted lipid analysis, isobaric molecular species can be separated and quantified. With this in-depth lipidome analysis, we achieved the quantification of 755 lipid species across 13 lipid classes, which enabled us to analyze the lipid profiles of OPSCCs and compare them to non-tumorous oropharyngeal tissue samples.

2. Results

In total, 11 oropharyngeal tissue samples from four patients with HPV-positive OPSCC were sampled by NIRL ablation. For differential quantitative lipidome analysis, OPSCC samples and non-tumorous oropharyngeal tissue from the adjacent areas were taken from each patient ($n = 7$ OPSCC and $n = 4$ healthy mucosa samples). Three technical replicates were obtained from each of the OPSCC and adjacent healthy tissue samples. The demographic and clinical data for all patients are presented in Table 1, and the individual demographic and clinical patient data are presented in Table 2. Table 3 shows the correlation between the sample labels and the individual patients.

Table 1. Demographic and clinical data for all patients.

Number of Patients (n)	4
Sex, (n (%))	
male	3 (75%)
female	1 (25%)
Mean age at surgery (years)	63
Age range (years)	51-69
OPSCC	
of the tonsils (n (%))	2 (50%)
of the base of the tongue (n (%))	2 (50%)

Table 2. Detailed demographic and clinical data for individual patients. BOT: base of the tongue; p16: p16 INK4A immunohistochemistry; HPV: human papilloma virus polymerase chain reaction for virus serotype 16.

Patient Number	Age	Gender	Tumor Location	Alcohol Consumption	Tobacco Consumption	OPSCC Samples per Patient	p16/HPV Status
A	69	M	BOT	Yes	No	2	+/+
B	64	F	BOT	No	Yes	2	+/+
C	66	M	Tonsil	Yes	No	1	+/+
D	51	M	Tonsil	Yes	Yes	2	+/+

Table 3. Origin of samples and correlation to patients. BOT: base of the tongue.

Patient	OPSCC Location	OPSCC Samples	Healthy Mucosa Samples
A	BOT	A-1 A-2	A-H
B	BOT	B-1 B-2	B-H
C	Tonsil	C-1	C-H
D	Tonsil	D-1 D-2	D-H

After each ablation, photographs were taken from the ablation site to document the tissue composition inside the sample (Figure 1). The total ablation time was 1 min 35 s. Figure 1b–d show the gentle vaporization of the NIRL ablation without visible burn marks on the tissue samples.

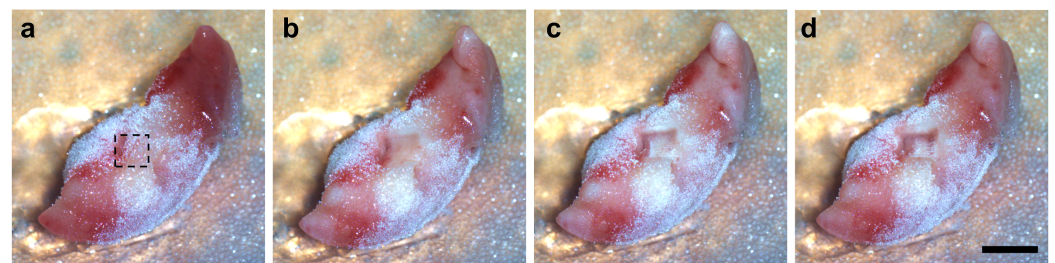


Figure 1. Images of the ablation process on the resected and frozen tissue of sample B-1 placed on the target of the sampling instrument. Images taken before ablation (a) and after each of the three replicate ablations, which were performed in a layer-wise fashion (b–d). The dashed line indicates the edges of the ablation area. NIRL produced a smooth removal of the tissue without any visible burn marks. Scale bar: 2 mm.

Figure 2 shows representative histopathologic H&E stains of tissue sample slides after ablation. It is noteworthy that the NIRL ablation has a high degree of precision.

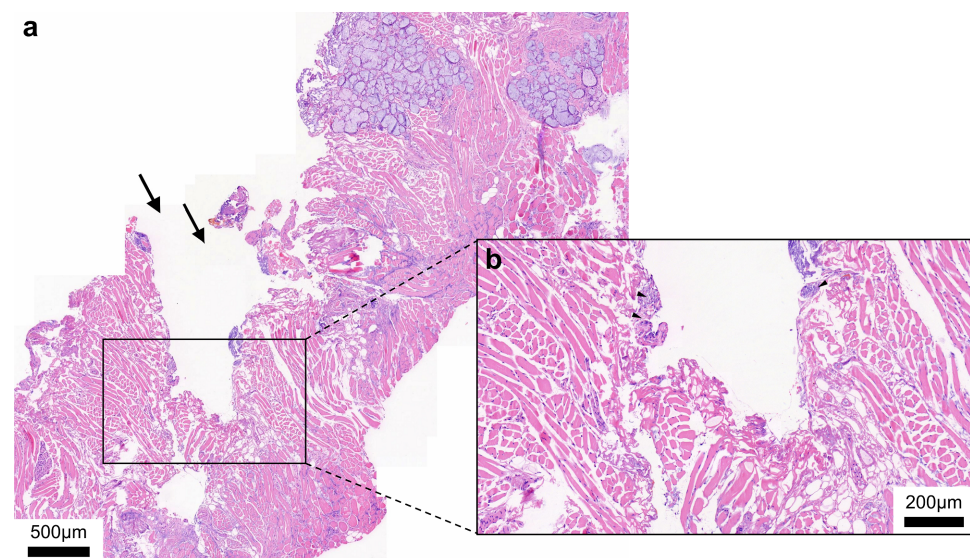


Figure 2. (a) Overview of muscle and connective tissue (incision indicated by arrows). (b) Higher magnification of the incision site.

2.1. Distribution of the Identified Lipid Classes

We were able to identify 13 lipid classes and 755 lipid species using mass-spectrometry-based shotgun lipidomics (Supplementary Table S1a,c). The following 13 lipid classes were quantitatively assessed: cholesterol ester (CE); ceramides (CER); diacylglycerides (DAG); dihydroceramides (DCER); free fatty acids (FFA); hexosylceramides (HCER); lysophosphatidylcholine (LCER); lysophosphatidylcholine (LPC); lysophosphatidylethanolamine (LPE); phosphatidylcholine (PC); phosphatidylethanolamine (PE); sphingomyelin (SM); and triacyl triglycerides (TAG).

Figure 3 shows the lipid compositions (across the 13 lipid classes) for the tumor and adjacent healthy tissue samples from patients A–D. For patient A (Figure 3a), there was an increase in the proportion of FFA, PC, PE, and SM in the OPSCC (base of the tongue; BOT) samples relative to the healthy tissue but a decrease in the proportion of TAG. Similar trends were observed for patient B (Figure 3b). Furthermore, the BOT samples from patients A and B both showed slight increases in the proportions of CE. Although the overall pattern of increases/decreases was similar, the BOT samples from patient A and patient B had different relative proportions of PC, PE, and FFA. The samples from patient A had a higher percentage of PC and PE and a lower percentage of FFA compared with the samples from patient B. For the non-tumorous oropharyngeal tissue samples, the relative proportions for each lipid class were similar for patients A and B (Supplementary Table S1d).

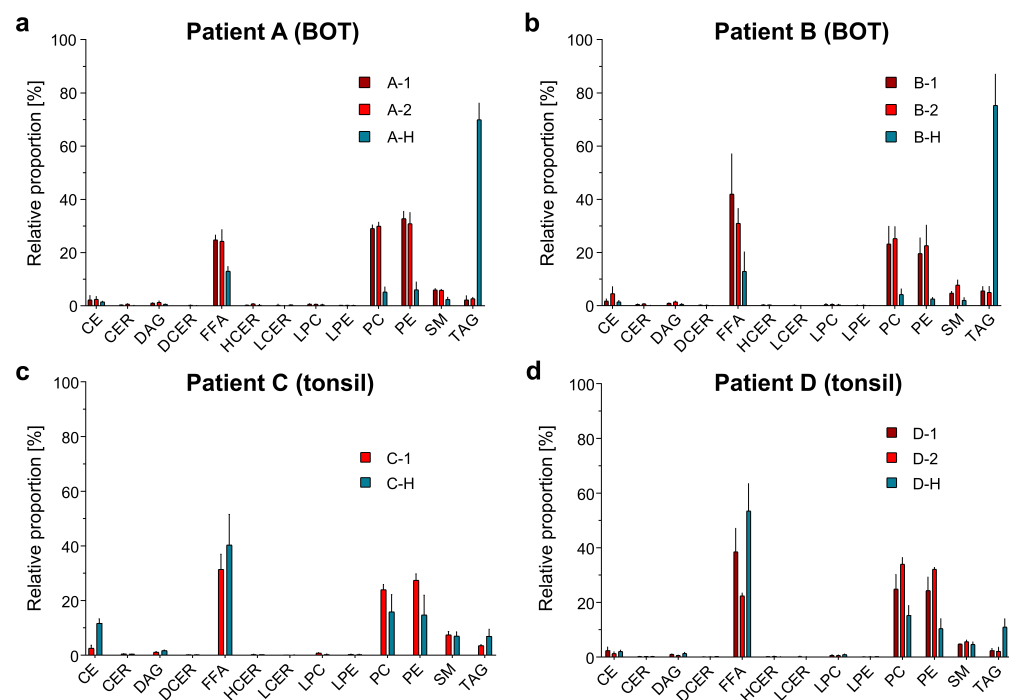


Figure 3. Lipid class composition for all patient samples A–D comparing the OPSCC and non-tumorous oropharyngeal tissue samples (Supplementary Table S1d). Table 3 gives an overview of the samples and their abbreviations. Error bars represent the standard deviation calculated from the three technical replicates per sample. CE: cholesterol ester; CER: ceramide; DAG: diacylglycerol; DCER: dihydroceramide; FFA: free fatty acids; HCER: hexosylceramide; LCER: lactosylceramide; LPC: lysophosphatidylcholine; LPE: lysophosphatidylethanolamine; PC: phosphatidylcholine; PE: phosphatidylethanolamine; SM: sphingomyelin; TAG: triacylglycerol.

The lipid compositions of the samples taken from tonsillar OPSCCs (patient C and D) are shown in Figure 3c,d. The trends in lipid composition of the OPSCC (tonsil) and adjacent healthy tissue samples differed in some aspects from the trends in the BOT samples. Unlike the BOT samples from patients A and B, which showed an increase in the proportion of FFA, the tonsillar samples from patients C and D showed a decrease in the proportion of

FFA. The OPSCC sample from patient C also showed a decrease in the proportion of CE, unlike patients A and B. However, similar to the patients A and B, patients C and D both showed an increase in the proportion of PC and PE in the OPSCC sample compared with the healthy tissue.

Overall, there was an increase in the proportion of PE and PC in OPSCC samples regardless of the tumor location. However, a characteristic specific to the BOT samples was a significant decrease in the proportion of TAG, from about 70% in the non-tumorous oropharyngeal tissue to 5% in the OPSCC samples.

Figure 4 presents the log₂ concentrations of the 13 lipid classes for OPSCC samples and the adjacent healthy tissue samples from each patient. The small standard deviation (calculated from the technical replicates) indicates that the method has good reproducibility. To further evaluate the reproducibility of NIRL-based sampling, Pearson correlation coefficients were calculated (Supplementary Table S1f). The results indicated a higher correlation within technical replicates of the same biological sample compared to different tissue samples. Additionally, all technical replicates within patient samples showed high correlation coefficients above 0.9, thereby indicating the reliability of NIRL-based tissue sampling. The bar graphs show the same pattern for all four patients: The highest concentrations are given for the lipid classes FFA, PC and PE, whereas CER, DCER, HCER, LCER, LPC, and LPE were quantified with very low concentrations of <1 nmol/mL.

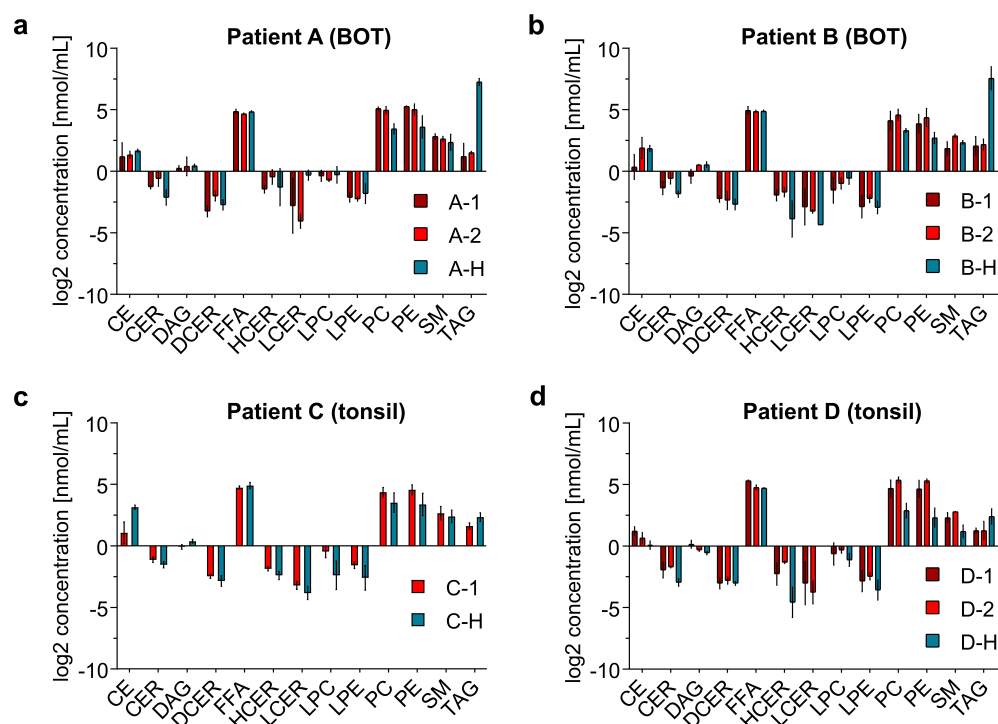


Figure 4. Visualization of log₂ concentration for each of the 13 lipid classes quantified in patient samples A-D (Supplementary Table S1e). Table 3 gives an overview of the samples and their abbreviations. Error bars represent the standard deviation calculated from the three technical replicates per sample. CE: cholesterol ester; CER: ceramide; DAG: diacylglycerol; DCER: dihydroceramide; FFA: free fatty acids; HCER: hexosylceramide; LCER: lactosylceramide; LPC: lysophosphatidylcholine; LPE: lysophosphatidylethanolamine; PC: phosphatidylcholine; PE: phosphatidylethanolamine; SM: sphingomyelin; TAG: triacylglycerol.

In the non-tumorous samples from patients A and B, we measured an exceptionally high concentration of TAG, which even exceeded the log₂ concentration of FFA, PC, and PE. This result is consistent with the lipid composition results described above, where a very high proportion of TAG was found to be characteristic of the healthy BOT samples.

However, for all patient samples, the TAG concentration was lower in the OPSCC samples than in the healthy samples. Our findings show that, for all patients, the PC and PE lipid concentrations were higher in the OPSCC samples than in the respective non-tumorous oropharyngeal tissue.

2.2. Differentiation Between Healthy Tissue and Tumor Tissue

To verify whether the tumor tissue could be clearly distinguished from the adjacent healthy tissue on the basis of the quantified concentrations of the 13 lipid classes, 122 lipid species (summarized by same fatty acyl chain length and degree of unsaturation), and 327 individual lipid species, we performed nonlinear iterative partial least squares (NIPALS) principal component analysis (PCA). Scatter plot visualizations of the PCA results are depicted in Figure 5, with samples from OPSCC and adjacent healthy tissue highlighted for BOT and tonsil samples separately.

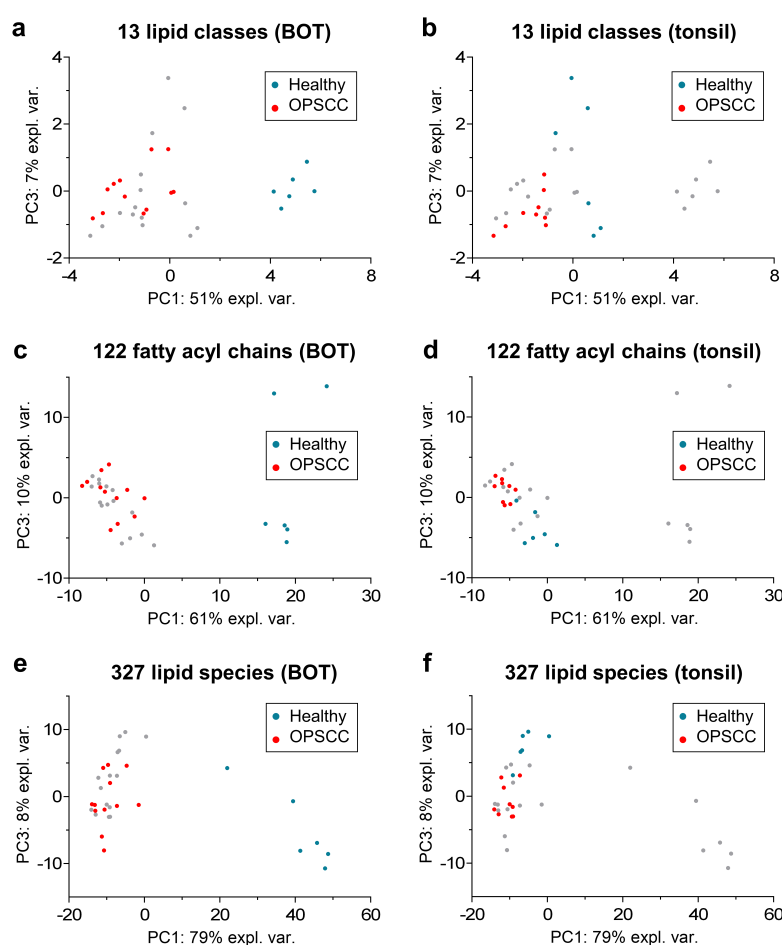


Figure 5. Scatter plot visualization of PCA results calculated with a nonlinear iterative partial least squares (NIPALS) algorithm based on 13 lipid classes, 122 lipid species with same fatty acyl chain length and extent of unsaturation, and 327 individual lipid species (Supplementary Table S2). Each dot represents a single technical replicate, and all technical replicates from all tissue samples are shown in each panel. The healthy (blue) and OPSCC (orange) replicates corresponding to the panel title (BOT or tonsil) are highlighted in each panel. The other oropharyngeal tissue replicates are shown in gray.

For the BOT samples (from patients A and B), there was a clear differentiation of tumorous and healthy tissue along the PC1, regardless of whether the NIPALS PCA was based on quantified lipid classes, lipid species with the same fatty acyl chain length and extent of unsaturation, or individual lipid species (Figure 5a,c,e). For the tonsil samples,

OPSCC and healthy tissue samples were also separated along the PC1 (Figure 5b,d). Based on both the lipid species summarized by their fatty acyl chain and individual lipid species, the different sample types could also be separated on the basis of PC3 (Figure 5d,f). Furthermore, the OPSCC samples for the tonsil and BOT were clustered in a very similar area in the scatterplot visualizations, but the non-tumorous samples for the tonsil and BOT were in different parts of vector space. From this, it can be assumed that there are similarities in the lipid profiles of the OPSCC samples from different tumor locations but that non-tumorous samples from the BOT and tonsil have different lipid profiles. This is consistent with the different TAG concentrations in the non-tumor tissues from the BOT and tonsil (Figure 4).

Welch's test was used to identify significant differences between the lipidomes of the OPSCC and healthy samples for each patient. As differences in the biological replicates are already shown in Figures 4 and 5, Welch's test was performed for each biological replicate, including three corresponding technical replicates. Figure 6 shows the results visualized as volcano plots. Significant two-fold changes ($p < 0.05$) for lipid classes are highlighted.

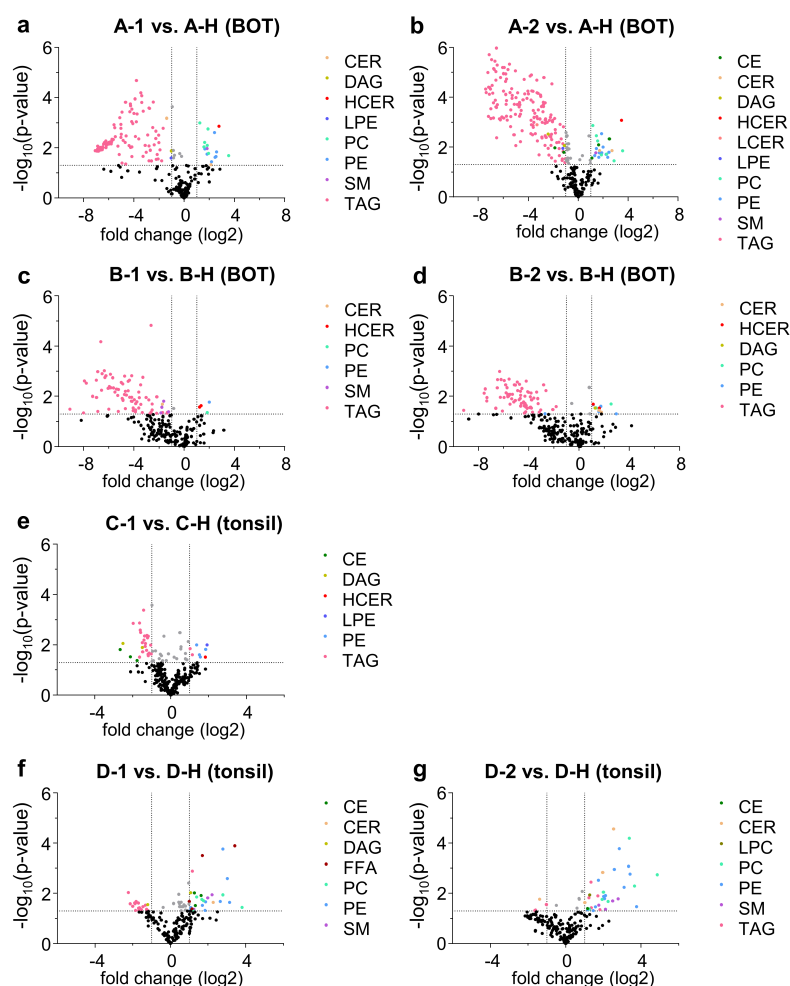


Figure 6. Volcano plots showing the results of the Welch's tests. The lipid species with a significant difference (p -value ≤ 0.05 , two-fold change) in their concentrations between the indicated samples are highlighted. Table 3 gives an overview of the samples and their abbreviations. Lipid species with a p -value > 0.05 are shown in black, and those with a p -value ≤ 0.05 but a fold change < 2 are shown in gray. CE: cholesterol ester; CER: ceramides; DAG: diacylglycerol; DCER: dihydroceramides; FFA: free fatty acids; HCER: hexosylceramides; LCER: lactosylceramides; LPC: lysophosphatidylcholine; LPE: lysophosphatidylethanolamine; PC: phosphatidylcholine; PE: phosphatidylethanolamine; SM: sphingomyelin; TAG: triacylglycerol.

For samples that originated from the BOT (from patients A and B; Figure 6a–d) there was a very strong deflection of the TAG. From the log₂ fold change, the concentration was 60-fold higher in the healthy tissue than in the OPSCC tissue. By contrast, the lipid classes PE, PC, and HCER showed a significant shift to higher concentrations in the OPSCC tissue compared with the non-tumorous oropharyngeal tissue.

We observed a significantly higher concentration of PC and PE in the OPSCC tissue from patient D (Figure 6f,g) compared with the corresponding healthy tissue: the difference was up to 32-fold, which was much higher than the difference in PC for the BOT samples (2–4-fold change). Another interesting lipid class was CE, which showed a significant difference in concentration between OPSCC and healthy tissue from patients A, C, and D. There was an increase in CE lipid species in OPSCC tissue from patients A and D but a decrease in OPSCC tissue from patient C.

Overall, when comparing the BOT and tonsil samples, the tonsil samples had fewer lipid species with significantly lower concentrations in the OPSCC samples than the healthy samples. This is highlighted in Table 4, which displays the number of lipid species with a significant difference (higher or lower) between OPSCC and healthy tissue, according to the results of the Welch's tests.

Table 4. Number of lipid species showing significant differences (p -value < 0.05, two-fold change) to lower or higher concentrations in OPSCC compared to the corresponding healthy tissue (Supplementary Table S3a–d).

Samples tested	BOT				Tonsil		
	Patient A	Patient B		Patient C	Patient D		
	A-1 vs. A-H	A-2 vs. A-H	B-1 vs. B-H	B-2 vs. B-H	C-1 vs. C-H	D-1 vs. D-H	D-2 vs. D-H
↓ in OPSCC	103	162	78	74	26	20	4
↑ in OPSCC	17	24	4	11	8	28	34

All sample pairs showed some significant differences; however, there were a greater number of significant differences for the sample pairs obtained from the BOT than from the tonsil.

3. Discussion

In this pilot study, we successfully demonstrated the feasibility of differentiating oropharyngeal tissue types using an innovative NIRL ablation setup with subsequent MS-based shotgun lipidomic analysis. This study shows the potential of the IRL-based platform to analyze and discriminate fresh frozen tissue samples from tumor (OPSCC) and non-tumor regions in the oropharynx and revealed significantly different lipid class compositions in healthy and cancerous tissue obtained from patients with differing gender, age, and habits (including alcohol and tobacco consumption).

We focused in particular on the exact determination of the lipid composition of the analyzed tissue to provide valuable information for our collective understanding of the alterations in lipid composition in OPSCCs. Therefore, we chose to use fresh frozen tissue samples rather than formalin-fixed paraffin-embedded (FFPE) samples, as some lipids are not preserved during FFPE processing [46–48]. Across all samples, we were able to identify 13 lipid classes with up to 755 individual lipid species.

In the second step, we analyzed the specific lipid classes and species for tissue discriminability. We found significant changes in the concentrations of lipid classes when comparing tumorous and non-tumorous tissue samples from all given patients. The TAG, CER, PC, and PE lipid classes were the decisive classes for the discrimination of tumorous and non-tumorous samples in our analysis. In particular, the 60-fold decrease of TAG in tumorous samples from the base of the tongue and the 2–4-fold decrease of TAG in

some of the tonsillar OPSCC samples make this lipid class potentially important and worth investigating in a larger patient population.

It is noteworthy that previous studies on lipidome changes of other neoplastic entities do not follow a general principal pattern for tumor genesis or progression. Li et al. were able to discriminate prostatic tumor samples from non-tumor samples via changes in CE, CER, nonesterified fatty acids, and TAG [49]. Another study on gastric cancer found relevant changes in the levels of lysophospholipids, PC, PE, PI, phosphoserines, SM, CER, and TAG when comparing cancerous and noncancerous tissue samples [50]. We assume that the patterns of change in lipid classes in our study are also unique to OPSCC. Nevertheless, recently published data by Ogrinc et al. on oral tongue SCC and non-tumor regions showed discrimination based on PC and PE in the positive ion mode and on phosphatidic acid, PI, and phosphatidylserines in the negative ion mode [12].

Similar to the study by Ogrinc et al., we were also confronted with high interpatient variability in lipidomic profiles [12]. Even though we observed a significant decrease in the concentration of TAG in all tumor tissue samples from the base of the tongue, this decrease was not observed in all tonsillar tumors. The same was evident for the increase in the PC and PE in all tumor samples. This may be a result of the macroscopic determination of the material being analyzed. Despite the subsequent histopathological assignment of the residual material, there is a chance that tumor-associated tissue types were present in the ablated region with a resulting alteration in lipid profiles. The presence of the tumor microenvironment is an inevitable factor when studying human specimens: it leads to higher complexity and therefore greater heterogeneity in the examined tissue than when cell line models, xenografts, or organoids are used [51]. Furthermore, the intrapatient heterogeneities found in our patient collective may also be attributed to individual alterations in cancer cell metabolism due to nutrition, lifestyle (e.g., tobacco use), and genetic factors. Despite the small patient cohort ($n = 4$), our findings show the method's potential to differentiate between OPSCC and non-tumorous oropharyngeal tissues based on significant alterations in lipid profiles. However, the above-mentioned (epi)genetic factors should be considered for future studies in a larger patient cohort, as the lipidome analysis of OPSCCs and the understanding of these factors and their influence on individual lipidomic profiles remains limited [52].

Overall, this study demonstrates the feasibility of lipidomic analysis of oropharyngeal tissue using a NIRL-based ablation setup, which, in principal, allows three-dimensional tissue sampling. The ablated tissue volume needed for the quantitative analysis of lipid classes with the Lipidyzer™ Platform is high when compared with approaches that use proteomics [45,53–55]. However, in this study, we successfully analyzed sample volumes of less than 500 nL, which corresponded to a voxel of 800 μm edge length. To our knowledge, this is the smallest reported sample volume for shotgun lipidomics with IRL-based tissue sampling, thus demonstrating the enormous potential of spatial lipidomics. The approach is much faster than classical mechanical homogenization and more volume efficient than the IRL-based sampling described in our previous study, which had an ablation volume of 1 mL (a factor of 2000) and utilized an aerosol cryotrap [40].

Improvements in the efficiency of aerosol capture and post-ablation sample processing, and modification of the MS instrument may help exploit this potential and further improve the spatial resolution of tissue sampling and differentiation. With a further increase in resolution, it may be possible to resolve the heterogeneity of the tumor inside the samples.

This study shows that IRL-based sampling in general—and NIRL-based sampling in particular—combined with tissue homogenization and an aerosol collection system is a very promising concept for future biopsies, as also demonstrated in our previous work [56]. When implemented in an image-guided handheld device or integrated into existing laryngoscopes, this approach could be applied during head and neck cancer screening, disease monitoring, or follow-up examinations. A further potential usage of NIRL MS-based lipidomic tissue sampling is intraoperatively in oncologic surgery, to enable a faster but nevertheless reliable determination of surgical margins in OPSCC. By

providing a deeper insight into the lipidome of OPSCCs, this study lays the foundation for such promising approaches.

4. Methods

4.1. Samples

A total of 11 oropharyngeal tissue samples from four patients were included in this study. The tissue samples were collected from July 2020 to December 2020 under general anesthesia at our institution. Following collection, the tissue samples were immediately rinsed with sodium chloride solution (NaCl 0.9%), transferred to 15 mL centrifuge tubes and frozen in liquid nitrogen. Samples were then stored at $-80\text{ }^{\circ}\text{C}$ until further processing. The samples were collected and processed in accordance with the World Medical Association Declaration of Helsinki and the guidelines for experimentation with humans by the Chambers of Physicians of the State of Hamburg. All patients gave written informed consent for their excised tissue to be used for research purposes. The Hamburg Commissioner for Data Protection and Freedom of Information (HmbBfDI) was notified of the collection of head and neck tumor tissue in the context of a biobank, in accordance with local laws (§12 HmbKHG) and the local ethics committee (Ethics commission Hamburg WF-049/09). For histopathologic reconfirmation, representative parts of the tissue samples were H&E stained following the standard operating procedures of the Institute of Pathology. The stained slides were evaluated blind by an expert pathologist to confirm the histological diagnosis.

4.2. Ablation Setup

The ablation setup is depicted in Figure 7a. From the outlet of the pulsed nanosecond infrared laser system (Opolette SE 2731, Opotek, Carlsbad, CA, USA), the divergent beam passed through a telescope with two plano-convex lenses (ISP-PX-25-150 and ISP-PX-25-100, ISP Optics Latvia, Riga, Latvia) for collimation purposes, followed by a 150 mm focusing lens (ISP-PX-25-150, ISP Optics Latvia, Riga, Latvia) with a spot diameter of about 150 μm . The relatively long focal distance of 150 mm of the setup for focusing the beam formed a relatively long focal spot of about 2 mm in the axial direction with equal energy distribution. This elongated spot volume compensated for minor height deviations on the sample surface. A dual-axis scanning mirror (OIM202, Optics in Motion, Long Beach, CA, USA), controlled by a data acquisition input/output device (USB-6343, National Instruments, Austin, TX, USA), was used for transverse scanning. Laser triggering was synchronized to the scanning mirror and timed to match the maximum possible repetition rate of 20 Hz. The two-inch scanning mirror also allowed the integration of a camera path for aiming purposes. The tissue sample was placed on a cooling stage inside a closed ablation chamber with a glass window on the top and two tube connectors to establish an air stream. The inlet was equipped with an air filter to minimize contamination. The emerging tissue aerosol from the ablation was transported to the outlet by a membrane pump (Mz 2c Vario, Vacuubrand, Wertheim, Germany) [57], where it passed through a short steel tube before being trapped on a glass fiber filter with a diameter of approximately 10 mm (GF50 grade, glass fiber filter without binders, Hahnemühle FineArt, Dassel, Germany) that was placed in a stainless steel filter mount (Figure 7a,b). After each ablation, the filter was transferred to a tube (Figure 7c).

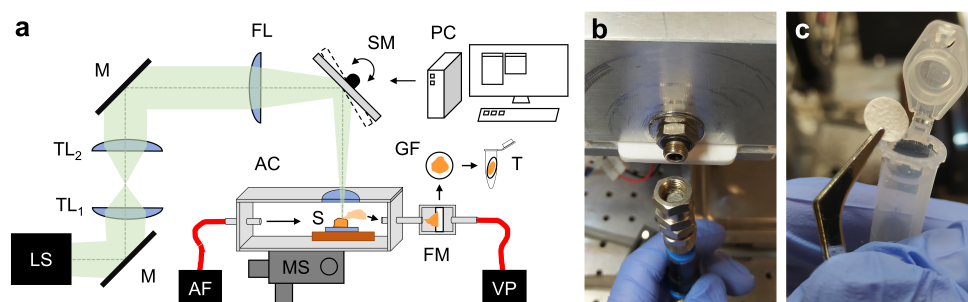


Figure 7. (a) Depiction of the ablation setup. (b) Filter mount (open). (c) Glass fiber filter (placed in a tube after ablation). LS: nanosecond infrared laser system; TL1/2: telescope lens 1/2; M: mirror; FL: focusing lens; SM: scanning mirror; PC: computer; AC: ablation chamber with cooling element; AF: air filter array; MS: 3-axis manual displacement stage; S: frozen sample; FM: filter mount; GF: glass fiber filter; VP: vacuum pump; T: tube.

4.3. Laser Parameters and Tissue Sampling

The tunable wavelength (2.70–3.10 μm) of the NIRL was set to 2.94 μm to match the O-H vibrational stretching band of water. The pulse energy was set to 1500 μJ at the sample position. In the custom-made control software, the scanning area was set to a square of 1.6 mm \times 1.6 mm containing a pattern of 15 \times 15 laser shots with a lateral spacing of 114 μm for each layer. For each sample technical replicate, six layers were ablated, resulting in a total of 1350 applied laser shots and the removal of a volume of about 1750 μm \times 1750 μm \times 160 μm , which corresponded to about 500 nL. The volume was determined by reference measurements with optical coherence tomography, as in our previous studies, where we demonstrated that the NIRL ablation volume is reproducible for technical replicates in a specific tissue type [44,45]. During the ablation process, the frozen tissue sample was temperature controlled at -10 $^{\circ}\text{C}$ to maximize consistent tissue removal. After sampling, the used glass fiber filter was removed and stored in a tube at -24 $^{\circ}\text{C}$. For this study, three ablations (technical replicates) were performed for each tissue sample. Before the next tissue sample was placed, the entire chamber and output tubing down to the filter mount were cleaned with isopropanol; the filter mount was also cleaned with isopropanol, as well as with an ultrasonic cleaner (USC100TH, VWR, Darmstadt, Germany) for 5 min.

4.4. Extraction of Lipids from the Tissue Aerosol Condensates

A LipidizerTM Internal Standards Kit (AB SCIEX, Framingham, MA, USA) was prepared according to the manufacturer's instructions and resuspended in methyl tert-butyl ether (MTBE). The glass fiber filter was mixed with 50 μL internal standard, 500 μL MTBE, and 160 μL methanol and then extracted for 30 min at 20 $^{\circ}\text{C}$ at a rotation speed of 400 rpm on a shaker (ThermoMixer[®] C, Eppendorf SE, Hamburg, Germany). After adding 200 μL water (LC-MS grade), the sample was centrifuged at 16,000 \times g for 5 min. The upper MTBE phase was removed and transferred to a new tube. After adding 300 μL MTBE, 100 μL methanol, and 100 μL water (LC-MS grade), the sample was mixed and centrifuged at 16,000 \times g (MIKRO 185, Andreas Hettich, Tuttlingen, Germany) for 5 min. The upper phase was removed and combined with the previous upper phase. The combined phases were dried in a vacuum concentrator centrifuge (UNIVAPO 100 H, UniEquip, Martinsried, Germany) and stored at -20 $^{\circ}\text{C}$ until further use. Prior to MS analyses, lipids were resuspended in 250 μL of 10 mM ammonium acetate in dichloromethane : methanol (50:50 (v/v)).

4.5. Lipidomic Analysis

Lipidomic analysis was carried out with a triple quadrupole mass spectrometer (QTRAP 5500; AB SCIEX, Framingham, MA, USA) equipped with a differential mobility spectrometer (DMS) interface operating with SelexION technology [58]. This de-

vice was coupled to an ultra-high pressure liquid chromatography system (Nexera X2, Shimadzu, Kyoto, Japan). The lipidomics platform (Lipidyzer™) was operated with lipidomics algorithms (Analyst version 1.6.8 and Lipidomics workflow manager; AB SCIEX, Framingham, MA, USA). The Lipidyzer™ Platform was tuned with a Selection Tuning Kit (AB SCIEX, Framingham, MA, USA), and a system suitability test was performed with a System Suitability Kit (AB SCIEX, Framingham, MA, USA), both according to the manufacturer's instructions. The Lipidyzer™ Platform used 10 mM ammonium acetate in dichloromethane : methanol (50:50 (v/v)) as the running buffer, dichloromethane : methanol (50:50 (v/v)) as rinses 0 and 1, 2-propanol as rinses 2 and 3, and 1-propanol as a DMS modifier. 50 µL samples were injected for both multiple reaction monitoring (MRM) methods: one with DMS on and one with DMS off. A detailed description of this shotgun approach has been reported previously [59]. Data processing and quantification were performed automatically by the Lipidyzer™ lipidomics workflow manager; lipid concentrations are given in nmol/mL.

4.6. Data Analysis and Visualization

Quantified lipid species concentrations were loaded into Perseus (version 1.6.15.0, Max Planck Institute for Biochemistry, Martinsried, Germany) and log₂ transformed. Nonlinear iterative partial least squares (NIPALS) principal component analysis (PCA) was performed in RStudio (version 2022.07.1 + 554, Posit PBC, Boston, MA, USA), with 70% valid values in at least one patient. That corresponded to 13 lipid classes, 122 lipid species with the same fatty acyl chain length and extent of unsaturation, and 327 individual lipid species (Supplementary Table S2a–c). Results of the NIPALS PCA are visualized as scatter plots (Figure 5). Further testing was performed with Welch's test. The results were filtered for *p*-value and fold-change significance (*p*-value ≤ 0.05, two-fold change). Significant lipid species are listed for each patient in Supplementary Table S3a–d.

5. Conclusions

In this pilot study, we have demonstrated that tissue sampling and homogenization utilizing a modified nanosecond infrared laser (NIRL) setup and consecutive mass spectrometric lipidome analysis is a promising approach for tissue classification and differentiation, which also has the potential to provide new insights into lipid composition alterations in OSPCC. To our knowledge, this study is the first to provide MS insights into the lipidome of this specific anatomic location. Subsequent studies with a larger patient population and with optimizations to reduce the minimum sample amount are necessary to fully explore the capacity of the NIRL MS platform and to prospectively enable *in vivo* tissue sampling with improved spatial resolution.

Supplementary Materials: The supporting information can be downloaded at: <https://www.mdpi.com/article/10.3390/ijms24097820/s1>.

Author Contributions: Conceptualization, R.S., D.E. and J.H. (Jan Hahn); methodology, J.H. (Jan Hahn) and M.M.; software, M.M., J.H. (Jan Hahn) and M.M.F.; validation, M.M., J.H. (Jan Hahn), M.M.F., R.S. and H.Z.; formal analysis, M.M., T.S.C. and M.M.F.; resources, J.H. (Jörg Heeren), A.B., D.E., C.S.B., J.H. (Jan Hahn) and H.S.; data curation, H.Z. and M.M.; writing—original draft preparation, R.S., M.M. and J.H. (Jan Hahn); writing—review and editing, R.S., C.S.B., T.S.C., J.H. (Jörg Heeren), J.H. (Jan Hahn), H.S., A.B. and D.E.; visualization, T.S.C., M.M., J.H. (Jan Hahn) and R.S.; supervision, A.B. and J.H. (Jan Hahn); project administration, J.H. (Jörg Heeren), J.H. (Jan Hahn) and D.E.; funding acquisition, J.H. (Jörg Heeren), J.H. (Jan Hahn), H.S., C.S.B., A.B. and D.E. All authors have read and agreed to the published version of the manuscript.

Funding: This research was funded by the “Behörde für Wissenschaft, Forschung, Gleichstellung und Bezirke der Freien und Hansestadt Hamburg” (Public Authority for Science, Research and Equality of the Free and Hanseatic City of Hamburg; grant number LFF-FV-75 and LFF-GK-10). This study was also partly supported by grants from the “Deutsche Forschungsgemeinschaft” (DFG) (INST 337/15-1, INST 337/16-1 and INST 152/837-1). Furthermore, this work was supported by intramural funding from the faculty.

Institutional Review Board Statement: The samples were collected and processed in accordance with the World Medical Association Declaration of Helsinki and the guidelines for experimentation with humans by the Chambers of Physicians of the State of Hamburg. All patients gave written informed consent for their excised tissue to be used for research purposes in context of the University Cancer Center of Hamburg (UCCH) Biobanking (Ethics commission of Hamburg WF-049/09).

Informed Consent Statement: Informed consent was obtained from all subjects involved in the study. Written informed consent has been obtained from the patient(s) to publish this paper.

Data Availability Statement: Mass spectrometric raw data was automatically processed by the Lipidizer Platform. The corresponding quantitative data can be found in Supplementary Table S1a–c.

Acknowledgments: We would like to thank Antonia Gocke for helping perform the laser ablations and sample preparation.

Conflicts of Interest: The authors declare no conflict of interest.

References

1. Sung, H.; Ferlay, J.; Siegel, R.L.; Laversanne, M.; Soerjomataram, I.; Jemal, A.; Bray, F. Global Cancer Statistics 2020: GLOBOCAN Estimates of Incidence and Mortality Worldwide for 36 Cancers in 185 Countries. *CA Cancer J. Clin.* **2021**, *71*, 209–249. [[CrossRef](#)] [[PubMed](#)]
2. Pytynia, K.B.; Dahlstrom, K.R.; Sturgis, E.M. Epidemiology of HPV-associated oropharyngeal cancer. *Oral Oncol.* **2014**, *50*, 380–386. [[CrossRef](#)] [[PubMed](#)]
3. Mody, M.D.; Rocco, J.W.; Yom, S.S.; Haddad, R.I.; Saba, N.F. Head and neck cancer. *Lancet* **2021**, *398*, 2289–2299. [[CrossRef](#)] [[PubMed](#)]
4. Lechner, M.; Liu, J.; Masterson, L.; Fenton, T.R. HPV-associated oropharyngeal cancer: Epidemiology, molecular biology and clinical management. *Nat. Rev. Clin. Oncol.* **2022**, *19*, 306–327. [[CrossRef](#)]
5. Bozec, A.; Culié, D.; Poissonnet, G.; Dassonville, O. Current role of primary surgical treatment in patients with head and neck squamous cell carcinoma. *Curr. Opin. Oncol.* **2019**, *31*, 138–145. [[CrossRef](#)]
6. Johnson, D.E.; Burtneiss, B.; Leemans, C.R.; Lui, V.W.Y.; Bauman, J.E.; Grandis, J.R. Head and neck squamous cell carcinoma. *Nat. Rev. Dis. Prim.* **2020**, *6*, 92. [[CrossRef](#)]
7. Santos, C.R.; Schulze, A. Lipid metabolism in cancer. *FEBS J.* **2012**, *279*, 2610–2623. [[CrossRef](#)]
8. Beloribi-Djefaflija, S.; Vasseur, S.; Guillaumond, F. Lipid metabolic reprogramming in cancer cells. *Oncogenesis* **2016**, *5*, e189. [[CrossRef](#)]
9. Vasseur, S.; Guillaumond, F. Lipids in cancer: a global view of the contribution of lipid pathways to metastatic formation and treatment resistance. *Oncogenesis* **2022**, *11*, 46. [[CrossRef](#)]
10. Butler, L.M.; Perone, Y.; Dehairs, J.; Lupien, L.E.; de Laat, V.; Talebi, A.; Loda, M.; Kinlaw, W.B.; Swinnen, J.V. Lipids and cancer: Emerging roles in pathogenesis, diagnosis and therapeutic intervention. *Adv. Drug Deliv. Rev.* **2020**, *159*, 245–293. [[CrossRef](#)]
11. Snaebjornsson, M.T.; Janaki-Raman, S.; Schulze, A. Greasing the Wheels of the Cancer Machine: The Role of Lipid Metabolism in Cancer. *Cell Metab.* **2020**, *31*, 62–76. [[CrossRef](#)]
12. Ogrinc, N.; Attencourt, C.; Colin, E.; Boudahi, A.; Tebbakha, R.; Salzet, M.; Testelin, S.; Dakpé, S.; Fournier, I. Mass Spectrometry-Based Differentiation of Oral Tongue Squamous Cell Carcinoma and Nontumor Regions With the SpiderMass Technology. *Front. Oral Health* **2022**, *3*, 827360. [[CrossRef](#)]
13. Dickinson, A.; Saraswat, M.; Joenväärä, S.; Agarwal, R.; Jyllikoski, D.; Wilkman, T.; Mäkitie, A.; Silén, S. Mass spectrometry-based lipidomics of oral squamous cell carcinoma tissue reveals aberrant cholesterol and glycerophospholipid—A Pilot study. *Transl. Oncol.* **2020**, *13*, 100807. [[CrossRef](#)]
14. Yu, B.; Wang, J. Lipidomics Identified Lyso-Phosphatidylcholine and Phosphatidylethanolamine as Potential Biomarkers for Diagnosis of Laryngeal Cancer. *Front. Oncol.* **2021**, *11*, 646779. [[CrossRef](#)]
15. Perrotti, F.; Rosa, C.; Cicalini, I.; Sacchetta, P.; Del Boccio, P.; Genovesi, D.; Pieragostino, D. Advances in Lipidomics for Cancer Biomarkers Discovery. *Int. J. Mol. Sci.* **2016**, *17*, 1992. [[CrossRef](#)]
16. Pan, M.; Qin, C.; Han, X. Lipid Metabolism and Lipidomics Applications in Cancer Research. In *Advances in Experimental Medicine and Biology*; Springer: Singapore, 2021; pp. 1–24. [[CrossRef](#)]
17. Baddour, H.M.; Magliocca, K.R.; Chen, A.Y. The importance of margins in head and neck cancer. *J. Surg. Oncol.* **2016**, *113*, 248–255. [[CrossRef](#)]

18. Ringash, J. Survivorship and Quality of Life in Head and Neck Cancer. *J. Clin. Oncol.* **2015**, *33*, 3322–3327. [[CrossRef](#)]
19. Bozzetti, F.; Bonfanti, G.; Bufalino, R.; Menotti, V.; Persano, S.; Andreola, S.; Doci, R.; Gennari, L. Adequacy of margins of resection in gastrectomy for cancer. *Ann. Surg.* **1982**, *196*, 685–690. [[CrossRef](#)]
20. Shin, D.; Park, S.S. Clinical importance and surgical decision-making regarding proximal resection margin for gastric cancer. *World J. Gastrointest. Oncol.* **2013**, *5*, 4–11. [[CrossRef](#)]
21. Heiss, N.; Rousson, V.; Ifticene-Treboux, A.; Lehr, H.A.; Delaloye, J.F. Risk factors for positive resection margins of breast cancer tumorectomy specimen following breast-conserving surgery. *Horm. Mol. Biol. Clin. Investig.* **2017**, *32*. [[CrossRef](#)]
22. Sakr, R.; Poulet, B.; Kaufman, G.; Nos, C.; Clough, K. Clear margins for invasive lobular carcinoma: A surgical challenge. *Eur. J. Surg. Oncol. (EJSO)* **2011**, *37*, 350–356. [[CrossRef](#)] [[PubMed](#)]
23. DiNardo, L.J.; Lin, J.; Karageorge, L.S.; Powers, C.N. Accuracy, Utility, and Cost of Frozen Section Margins in Head and Neck Cancer Surgery. *Laryngoscope* **2000**, *110*, 1773–1776. [[CrossRef](#)] [[PubMed](#)]
24. Ribeiro, N.; Godden, D.; Wilson, G.; Butterworth, D.; Woodward, R. Do frozen sections help achieve adequate surgical margins in the resection of oral carcinoma? *Int. J. Oral Maxillofac. Surg.* **2003**, *32*, 152–158. [[CrossRef](#)] [[PubMed](#)]
25. Du, E.; Ow, T.J.; Lo, Y.T.; Gersten, A.; Schiff, B.A.; Tassler, A.B.; Smith, R.V. Refining the utility and role of Frozen section in head and neck squamous cell carcinoma resection. *Laryngoscope* **2016**, *126*, 1768–1775. [[CrossRef](#)] [[PubMed](#)]
26. Layfield, E.M.; Schmidt, R.L.; Esebua, M.; Layfield, L.J. Frozen Section Evaluation of Margin Status in Primary Squamous Cell Carcinomas of the Head and Neck: A Correlation Study of Frozen Section and Final Diagnoses. *Head Neck Pathol.* **2018**, *12*, 175–180. [[CrossRef](#)]
27. Black, C.; Marotti, J.; Zarovnyaya, E.; Paydarfar, J. Critical evaluation of frozen section margins in head and neck cancer resections. *Cancer* **2006**, *107*, 2792–2800. [[CrossRef](#)]
28. Desciak, E.B.; Maloney, M.E. Artifacts in Frozen Section Preparation. *Dermatol. Surg.* **2000**, *26*, 500–504. [[CrossRef](#)]
29. Novis, D.A.; Zarbo, R.J. Interinstitutional comparison of frozen section turnaround time. A College of American Pathologists Q-Probes study of 32868 frozen sections in 700 hospitals. *Arch. Pathol. Lab. Med.* **1997**, *121*, 559–567.
30. Phelps, D.L.; Balog, J.; Gildea, L.F.; Bodai, Z.; Savage, A.; El-Bahrawy, M.A.; Speller, A.V.; Rosini, F.; Kudo, H.; McKenzie, J.S.; et al. The surgical intelligent knife distinguishes normal, borderline and malignant gynaecological tissues using rapid evaporative ionisation mass spectrometry (REIMS). *Br. J. Cancer* **2018**, *118*, 1349–1358. [[CrossRef](#)]
31. Woolman, M.; Tata, A.; Dara, D.; Meens, J.; D’Arcangelo, E.; Perez, C.J.; Saiyara Prova, S.; Bluemke, E.; Ginsberg, H.J.; Ifa, D.; et al. Rapid determination of the tumour stroma ratio in squamous cell carcinomas with desorption electrospray ionization mass spectrometry (DESI-MS): a proof-of-concept demonstration. *Analyst* **2017**, *142*, 3250–3260. [[CrossRef](#)]
32. Fatou, B.; Saudemont, P.; Leblanc, E.; Vinatier, D.; Mesdag, V.; Wisztorski, M.; Focsa, C.; Salzet, M.; Ziskind, M.; Fournier, I. In vivo Real-Time Mass Spectrometry for Guided Surgery Application. *Sci. Rep.* **2016**, *6*, 25919. [[CrossRef](#)]
33. Zhang, J.; Rector, J.; Lin, J.Q.; Young, J.H.; Sans, M.; Katta, N.; Giese, N.; Yu, W.; Nagi, C.; Suliburk, J.; et al. Nondestructive tissue analysis for ex vivo and in vivo cancer diagnosis using a handheld mass spectrometry system. *Sci. Transl. Med.* **2017**, *9*. [[CrossRef](#)]
34. Woolman, M.; Qiu, J.; Kuzan-Fischer, C.M.; Ferry, I.; Dara, D.; Katz, L.; Daud, F.; Wu, M.; Ventura, M.; Bernards, N.; et al. In situ tissue pathology from spatially encoded mass spectrometry classifiers visualized in real time through augmented reality. *Chem. Sci.* **2020**, *11*, 8723–8735. [[CrossRef](#)]
35. Saudemont, P.; Quanicco, J.; Robin, Y.M.; Baud, A.; Balog, J.; Fatou, B.; Tierny, D.; Pascal, Q.; Minier, K.; Pottier, M.; et al. Real-Time Molecular Diagnosis of Tumors Using Water-Assisted Laser Desorption/Ionization Mass Spectrometry Technology. *Cancer Cell* **2018**, *34*, 840–851.e4. [[CrossRef](#)]
36. Ogrinc, N.; Saudemont, P.; Balog, J.; Robin, Y.M.; Gimeno, J.P.; Pascal, Q.; Tierny, D.; Takats, Z.; Salzet, M.; Fournier, I. Water-assisted laser desorption/ionization mass spectrometry for minimally invasive in vivo and real-time surface analysis using SpiderMass. *Nat. Protoc.* **2019**, *14*, 3162–3182. [[CrossRef](#)]
37. Böttcher, A.; Kucher, S.; Knecht, R.; Jowett, N.; Krötz, P.; Reimer, R.; Schumacher, U.; Anders, S.; Münscher, A.; Dalchow, C.V.; et al. Reduction of thermocoagulative injury via use of a picosecond infrared laser (PIRL) in laryngeal tissues. *Eur. Arch. Otorhinolaryngol.* **2015**, *272*, 941–948. [[CrossRef](#)]
38. Cowan, M.L.; Bruner, B.D.; Huse, N.; Dwyer, J.R.; Chugh, B.; Nibbering, E.T.J.; Elsaesser, T.; Miller, R.J.D. Ultrafast memory loss and energy redistribution in the hydrogen bond network of liquid H₂O. *Nature* **2005**, *434*, 199–202. [[CrossRef](#)]
39. Franjic, K.; Miller, R.J.D. Vibrationally excited ultrafast thermodynamic phase transitions at the water/air interface. *Phys. Chem. Chem. Phys.* **2010**, *12*, 5225. [[CrossRef](#)]
40. Wurlitzer, M.; Hessling, E.; Rinas, K.; Fuh, M.; Petersen, H.; Ricklefs, F.; Lamszus, K.; Regelsberger, J.; Maier, S.; Kruber, S.; et al. Mass Spectrometric Lipid Profiles of Picosecond Infrared Laser-Generated Tissue Aerosols Discriminate Different Brain Tissues. *Lasers Surg. Med.* **2020**, *52*, 228–234. [[CrossRef](#)]
41. Woolman, M.; Ferry, I.; Kuzan-Fischer, C.M.; Wu, M.; Zou, J.; Kiyota, T.; Isik, S.; Dara, D.; Aman, A.; Das, S.; et al. Rapid determination of medulloblastoma subgroup affiliation with mass spectrometry using a handheld picosecond infrared laser desorption probe. *Chem. Sci.* **2017**, *8*, 6508–6519. [[CrossRef](#)]
42. Zou, J.; Talbot, F.; Tata, A.; Ermini, L.; Franjic, K.; Ventura, M.; Zheng, J.; Ginsberg, H.; Post, M.; Ifa, D.R.; et al. Ambient Mass Spectrometry Imaging with Picosecond Infrared Laser Ablation Electrospray Ionization (PIR-LAESI). *Anal. Chem.* **2015**, *87*, 12071–12079. [[CrossRef](#)] [[PubMed](#)]

43. Dreisewerd, K.; Draude, F.; Kruppe, S.; Rohlfing, A.; Berkenkamp, S.; Pohlentz, G. Molecular Analysis of Native Tissue and Whole Oils by Infrared Laser Mass Spectrometry. *Anal. Chem.* **2007**, *79*, 4514–4520. [[CrossRef](#)] [[PubMed](#)]
44. Voß, H.; Moritz, M.; Pelczar, P.; Gagliani, N.; Huber, S.; Nippert, V.; Schlüter, H.; Hahn, J. Tissue Sampling and Homogenization with NIRL Enables Spatially Resolved Cell Layer Specific Proteomic Analysis of the Murine Intestine. *Int. J. Mol. Sci.* **2022**, *23*, 6132. [[CrossRef](#)] [[PubMed](#)]
45. Hahn, J.; Moritz, M.; Voß, H.; Pelczar, P.; Huber, S.; Schlüter, H. Tissue Sampling and Homogenization in the Sub-Microliter Scale with a Nanosecond Infrared Laser (NIRL) for Mass Spectrometric Proteomics. *Int. J. Mol. Sci.* **2021**, *22*, 10833. [[CrossRef](#)]
46. Ogrinc, N.; Caux, P.D.; Robin, Y.M.; Bouchaert, E.; Fatou, B.; Ziskind, M.; Focsa, C.; Bertin, D.; Tierny, D.; Takats, Z.; et al. Direct Water-Assisted Laser Desorption/Ionization Mass Spectrometry Lipidomic Analysis and Classification of Formalin-Fixed Paraffin-Embedded Sarcoma Tissues without Dewaxing. *Clin. Chem.* **2021**, *67*, 1513–1523. [[CrossRef](#)]
47. Vos, D.; Bowman, A.; Heeren, R.; Balluff, B.; Ellis, S. Class-specific depletion of lipid ion signals in tissues upon formalin fixation. *Int. J. Mass Spectrom.* **2019**, *446*, 116212. [[CrossRef](#)]
48. Gaudin, M.; Panchal, M.; Aycirix, S.; Werner, E.; Brunelle, A.; Touboul, D.; Boursier-Neyret, C.; Auzeil, N.; Walther, B.; Duyckaerts, C.; et al. Ultra performance liquid chromatography - mass spectrometry studies of formalin-induced alterations of human brain lipidome. *J. Mass Spectrom.* **2014**, *49*, 1035–1042. [[CrossRef](#)]
49. Li, J.; Ren, S.; Piao, H.L.; Wang, F.; Yin, P.; Xu, C.; Lu, X.; Ye, G.; Shao, Y.; Yan, M.; et al. Integration of lipidomics and transcriptomics unravels aberrant lipid metabolism and defines cholesteryl oleate as potential biomarker of prostate cancer. *Sci. Rep.* **2016**, *6*, 20984. [[CrossRef](#)]
50. Hung, C.Y.; Yeh, T.S.; Tsai, C.K.; Wu, R.C.; Lai, Y.C.; Chiang, M.H.; Lu, K.Y.; Lin, C.N.; Cheng, M.L.; Lin, G. Glycerophospholipids pathways and chromosomal instability in gastric cancer: Global lipidomics analysis. *World J. Gastrointest. Oncol.* **2019**, *11*, 181–194. [[CrossRef](#)]
51. Katz, L.; Woolman, M.; Tata, A.; Zarrine-Afsar, A. Potential impact of tissue molecular heterogeneity on ambient mass spectrometry profiles: A note of caution in choosing the right disease model. *Anal. Bioanal. Chem.* **2021**, *413*, 2655–2664. [[CrossRef](#)]
52. Katz, L.; Tata, A.; Woolman, M.; Zarrine-Afsar, A. Lipid Profiling in Cancer Diagnosis with Hand-Held Ambient Mass Spectrometry Probes: Addressing the Late-Stage Performance Concerns. *Metabolites* **2021**, *11*, 660. [[CrossRef](#)]
53. Donnarumma, F.; Murray, K.K. Laser ablation sample transfer for localized LC-MS/MS proteomic analysis of tissue. *J. Mass Spectrom.* **2016**, *51*, 261–268. [[CrossRef](#)]
54. Pettit, M.E.; Donnarumma, F.; Murray, K.K.; Solouki, T. Infrared laser ablation sampling coupled with data independent high resolution UPLC-IM-MS/MS for tissue analysis. *Anal. Chim. Acta* **2018**, *1034*, 102–109. [[CrossRef](#)]
55. Wang, Y.; Yutuc, E.; Griffiths, W.J. Standardizing and increasing the utility of lipidomics: a look to the next decade. *Expert Rev. Proteom.* **2020**, *17*, 699–717. [[CrossRef](#)]
56. Schluter, M.; Fuh, M.M.; Maier, S.; Otte, C.; Kiani, P.; Hansen, N.O.; Dwayne Miller, R.J.; Schluter, H.; Schlaefer, A. Towards OCT-Navigated Tissue Ablation with a Picosecond Infrared Laser (PIRL) and Mass-Spectrometric Analysis. In Proceedings of the 2019 41st Annual International Conference of the IEEE Engineering in Medicine and Biology Society (EMBC), Berlin, Germany, 23–27 July 2019; pp. 158–161. [[CrossRef](#)]
57. Krutilin, A.; Maier, S.; Schuster, R.; Kruber, S.; Kwiatkowski, M.; Robertson, W.D.; Hansen, N.O.; Miller, R.J.D.; Schlüter, H. Sampling of Tissues with Laser Ablation for Proteomics: Comparison of Picosecond Infrared Laser and Microsecond Infrared Laser. *J. Proteome Res.* **2019**, *18*, 1451–1457. [[CrossRef](#)]
58. Schneider, B.B.; Covey, T.R.; Coy, S.L.; Krylov, E.V.; Nazarov, E.G. Planar differential mobility spectrometer as a pre-filter for atmospheric pressure ionization mass spectrometry. *Int. J. Mass Spectrom.* **2010**, *298*, 45–54. [[CrossRef](#)]
59. Lintonen, T.P.I.; Baker, P.R.S.; Suoniemi, M.; Ubhi, B.K.; Koistinen, K.M.; Duchoslav, E.; Campbell, J.L.; Ekroos, K. Differential Mobility Spectrometry-Driven Shotgun Lipidomics. *Anal. Chem.* **2014**, *86*, 9662–9669. [[CrossRef](#)]

Disclaimer/Publisher's Note: The statements, opinions and data contained in all publications are solely those of the individual author(s) and contributor(s) and not of MDPI and/or the editor(s). MDPI and/or the editor(s) disclaim responsibility for any injury to people or property resulting from any ideas, methods, instructions or products referred to in the content.

5.3 TISSUE SAMPLING AND HOMOGENIZATION WITH NIRL ENABLES SPATIALLY RESOLVED CELL LAYER SPECIFIC PROTEOMIC ANALYSIS OF THE MURINE INTESTINE

Hannah Voß*, Manuela Moritz*, Penelope Pelczar, Nicola Gagliani, Samuel Huber, Vivien Nippert, Hartmut Schlüter and Jan Hahn

Int. J. Mol. Sci. **2022**, *23*, 6132

*Shared first authorship

The studies performed by Hahn & Moritz et al. and Stadlhofer & Moritz et al. have resulted in a notable advancement in the methodological evolution of NIRL-based tissue sampling and sample processing for the mass spectrometric analysis of low-input amounts. In both studies, comprehensive analysis with high coverage was achieved when miniaturized tissue volumes of approximately 500 nL were sampled by NIRL and subsequently processed either by the developed protocol for differential quantitative bottom-up proteomics or quantitative shotgun lipidomics. This provided the foundation for further development towards spatial omics. Therefore, in this study it has been investigated whether the methodological developments can be successfully transferred to an application in spatial 3D proteomics. In the first part of the study, NIRL was used to ablate tissue layers of ~117 µm from the ascending, transverse and descending part of murine intestine. NIRL-ablated samples were further analyzed by subsequent differential bottom-up proteomics and revealed 3,053 proteins across all samples. Overall, 303 proteins were found to be ANOVA significant between the three different colon parts, showing distinguishable protein patterns in the hierarchical clustering. Further enrichment analysis revealed that these differences are primarily associated with proteins involved in diverse metabolic processes (e.g., glycolysis/gluconeogenesis and the citric acid cycle) and antioxidant activity. This finding is consistent with the differences in the activities of the colonic segments in terms of digestion, nutrient absorption, secretion, and immune response and control, which reflect the main functions of the gastrointestinal tract. In the second part of the study, eight consecutive tissue layers of ~117 µm each were sampled from murine intestine by NIRL and the samples were processed by differential quantitative bottom-up proteomics revealing 2,882 proteins with quantitative information. Based on the scatterplot visualization of PCA results, a gradient-wise separation along principal component 1 was observed while principal component 2 represented differences due to the different sampling areas. To further test whether the samples taken layer-by-layer represent different cellular compositions, Pearson correlation-based consensus clustering was applied, and the proportion of ambiguous clustering (PAC) score was calculated. Based on the results, four differentiable protein patterns (cluster 1-4) were identified across the ablated layers and the samples were assigned accordingly to the corresponding clusters prior to further statistical testing. While the ANOVA testing revealed 251 proteins to be significantly differentially abundant between the clusters, the heatmap visualization of ANOVA significant proteins only showed clear differences between cluster 1 and 4 corresponding to the ablated layers 1-2 and layers 6-8, respectively. In a further comprehensive proteome analysis, leucocyte mediated immunity and epithelial cell specificity as well as enrichment of metabolic processes were found for cluster 1. In contrast, cluster 4 showed an enrichment of proteins associated with muscle development and muscle contraction. According to this, it was assumed that cluster 1 (layer 1-2) belongs to the mucosa, including the leucocyte-infiltrated epithelium and cluster 4 (layer 6-8) to the muscularis propria. This assumption was confirmed by analyzing the relative abundances of known epithelial and muscular marker proteins across consecutive layers. While the highest protein abundance of all epithelial markers was found in the first layer, the highest abundance of the respective muscular markers was found in layers 6-8. The specificity of the marker proteins for the mucosa and muscularis propria was additionally verified by immunohistochemical (IHC) stainings obtained from the Human Protein Atlas. For the two intermediate cellular areas 2 and 3, high intensities of both muscle- and epithelium-specific proteins were found, and the cluster could not be clearly assigned to muscularis mucosa and

submucosa. Based on the previously achieved advancements for the sampling and processing of low-input amounts, the proteome of murine intestine was studied with an axial resolution of 117 μm , for the first time. In the follow-up study of Navolić & Moritz et al., the spatial resolution has been further refined to an axial resolution of 40 μm by adapting the sample processing protocol to the latest developments in proteomics regarding the analysis of low-input amounts. In summary, three-dimensional spatial proteome analysis of the region- and cell layer-specific proteome of murine intestine was successfully performed.



Article

Tissue Sampling and Homogenization with NIRL Enables Spatially Resolved Cell Layer Specific Proteomic Analysis of the Murine Intestine

Hannah Voß ^{1,†}, Manuela Moritz ^{1,†}, Penelope Pelczar ², Nicola Gagliani ^{2,3}, Samuel Huber ², Vivien Nippert ¹, Hartmut Schlüter ^{1,*} and Jan Hahn ^{1,*}

¹ Section/Core Facility Mass Spectrometry and Proteomics, University Medical Center Hamburg-Eppendorf (UKE), Martinistraße 52, 20246 Hamburg, Germany; ha.voss@uke.de (H.V.); ma.moritz@uke.de (M.M.); vivien.nippert@gmail.com (V.N.)

² Section of Molecular Immunology und Gastroenterology, I. Department of Medicine, University Medical Center Hamburg-Eppendorf (UKE), Martinistraße 52, 20246 Hamburg, Germany; p.pelczar@uke.de (P.P.); n.gagliani@uke.de (N.G.); s.huber@uke.de (S.H.)

³ Department of General, Visceral and Thoracic Surgery, University Medical Center Hamburg-Eppendorf (UKE), Martinistraße 52, 20246 Hamburg, Germany

* Correspondence: hschluet@uke.de (H.S.); ja.hahn@uke.de (J.H.); Tel.: +49-1575-6085997 (H.S.); +49-1522-2827168 (J.H.)

† These authors contributed equally to this work.



Citation: Voß, H.; Moritz, M.; Pelczar, P.; Gagliani, N.; Huber, S.; Nippert, V.; Schlüter, H.; Hahn, J. Tissue Sampling and Homogenization with NIRL Enables Spatially Resolved Cell Layer Specific Proteomic Analysis of the Murine Intestine. *Int. J. Mol. Sci.* **2022**, *23*, 6132. <https://doi.org/10.3390/ijms23116132>

Academic Editor: Alessandro Attanzio

Received: 30 April 2022

Accepted: 27 May 2022

Published: 30 May 2022

Publisher's Note: MDPI stays neutral with regard to jurisdictional claims in published maps and institutional affiliations.



Copyright: © 2022 by the authors. Licensee MDPI, Basel, Switzerland. This article is an open access article distributed under the terms and conditions of the Creative Commons Attribution (CC BY) license (<https://creativecommons.org/licenses/by/4.0/>).

Abstract: For investigating the molecular physiology and pathophysiology in organs, the most exact data should be obtained; if not, organ-specific cell lines are analyzed, or the whole organ is homogenized, followed by the analysis of its biomolecules. However, if the morphological organization of the organ can be addressed, then, in the best case, the composition of molecules in single cells of the target organ can be analyzed. Laser capture microdissection (LCM) is a technique which enables the selection of specific cells of a tissue for further analysis of their molecules. However, LCM is a time-consuming two-dimensional technique, and optimal results are only obtained if the tissue is fixed, e.g., by formalin. Especially for proteome analysis, formalin fixation reduced the number of identifiable proteins, and this is an additional drawback. Recently, it was demonstrated that sampling of fresh-frozen (non-fixed) tissue with an infrared-laser is giving higher yields with respect to the absolute protein amount and number of identifiable proteins than conventional mechanical homogenization of tissues. In this study, the applicability of the infrared laser tissue sampling for the proteome analysis of different cell layers of murine intestine was investigated, using LC-MS/MS-based differential quantitative bottom-up proteomics. By laser ablation, eight consecutive layers of colon tissue were obtained and analyzed. However, a clear distinguishability of protein profiles between ascending, descending, and transversal colon was made, and we identified the different intestinal-cell-layer proteins, which are cell-specific, as confirmed by data from the Human Protein Atlas. Thus, for the first time, sampling directly from intact fresh-frozen tissue with three-dimensional resolution is giving access to the different proteomes of different cell layers of colon tissue.

Keywords: tissue sampling; nanosecond infrared laser; laser ablation; proteomics; mass spectrometry; colon tissue; 3D-sampling; miniaturization

1. Introduction

The analysis of the entirety of biomolecule classes—omes—in cultured cells in the past two decades has largely improved our knowledge about molecular physiology and pathophysiology. However, the limits of cell-culture-based research is getting more and more obvious. For circumventing these limits, the development of organoids is currently a fast-growing field in life sciences [1]. Nevertheless, the ideal case is to study omes in the cells of tissues because, even in organoids, the microenvironment is lacking [1].

Until today, the analysis of omes from defined cells of a tissue of interest is still challenging and comprises several steps. After removing the tissue from the organism, it must be homogenized for releasing and solubilizing molecules from the tissue in a liquid for making them accessible to analytical techniques. After solubilization, the biomolecules of interest may pass sample preparation steps, e.g., for their enrichment, prior to their analysis with methods such as liquid chromatography (LC) and mass spectrometry (MS). The homogenization of the tissue is usually achieved mechanically. Several homogenization procedures are available and chosen with respect to the type of tissue, as well as the subsequent type of bioanalytical method and biomolecule class of interest (e.g., proteins [2], nucleotides [3], and lipids [4]. Common procedures are, for example, dispersing machines using the rotor-stator principle, milling devices for transforming freeze-dried tissue to powders, bead mills for small amounts of fresh tissue (“wet milling”) [5], or cryogenic grinding devices [6]. High hydrostatic pressure was demonstrated for tissue homogenization by Gross et al. [7].

Homogenization of tissue is always a critical step for several reasons: (1) Homogenization may not be complete, thus leaving biomolecules in those parts, which are not solubilized, and which are part of the pellets remaining after centrifugation. In addition, the insoluble materials may adsorb other biomolecules and, thus, be co-precipitated. Biomolecules being integrated into these insoluble parts or adsorbed to them are lost for subsequent analysis. (2) During homogenization, cells are broken, and, thereby, enzymes are released from their compartments, such as lysosomes. Enzymes can quickly degrade or convert other biomolecules. Proteases are cleaving other proteins; phosphatases are removing phosphates from phosphor-proteins and other phosphorylated molecules. For all biomolecule classes from a cell, there are enzymes that can convert them.

(3) Biomolecules released from their compartments are not protected anymore and therefore often prone to chemical reactions such as oxidation [8], reactions with other biomolecules [9], or with buffer components [10]. Such chemical reactions can already occur during homogenization of tissue. As a result of all these problems that occur during homogenization, the original composition of biomolecules is changed, yielding false results, which make the deciphering of cell physiological mechanisms even more difficult or impossible.

Diverse procedures and instruments were developed for minimizing the above-mentioned problems. For example, protease inhibitors are used for decreasing the enzymatic degradation of proteins [2]. Detailed insights into problems associated with homogenization of tissues and actions for decreasing these problems are given in numerous reviews, e.g., from Bodzon-Kulakowska et al. [11], Gli et al. [12] and Goldberg et al. [6]. An effective instrument to significantly decrease enzymatic affinities in tissues was developed by Svensson et al. [13]. This instrument rapidly and irreversibly denatures the proteins in a tissue sample by conductive heating under controlled pressure. This commercially available instrument (“denator”) is a step forward regarding the stabilization of biomolecules and has been shown in many investigations [14] and summarized in several reviews (e.g., Sköld et al.) [15]. However, the denator instrument is not a solution regarding the problems associated with homogenization as described above.

The state-of-the-art is still the mechanical homogenization of tissues for subsequent omics, dominated by cryo-pulverization procedures. Critical in almost all mechanical homogenization techniques is the problem that the tissue is not 100% solubilized. After centrifugation, there will be still a pellet with undissolved tissue material. A disadvantage is that, in the investigations mentioned above, tissues are homogenized in toto without considering their composition comprising different cell types.

An important aspect of tissues is their three-dimensional spatial organization of tissue-specific cell types. The high importance of spatially and cell-type resolved omics analysis of tissue has been shown, for example, by Doll et al. [16], who described significant proteomic differences across different cell types and regions within the heart, brain, and liver. This aspect should also be carefully addressed, especially in the investigation of tumor tissue.

It is well-known, as Mertins et al., 2018 [17] stated, that solid tumor tissues typically consist of at least epithelial, stromal, and hematologic components, as well as necrotic areas. Thus, for characterizing the omes of cancer cells in a solid tumor, it is desirable to differentiate between the different cancer-associated cell types and exclude non-cancer cell types that are present near the tumor. In the worst case, the important markers of cancer cannot be recognized anymore. A further problem, decreasing the number of identifiable proteins, originates from proteins derived from blood in tissues. Blood-borne proteins have strong suppressive effects in mass spectrometry. Thus, a technique offering spatial resolution during sampling is very advantageous if it is the aim to characterize the entirety of a biomolecule class.

The spatial aspect of tissues today is best addressed by laser-capture microdissection (LCM) [18]. Cells of interest in a tissue section are recognized by a microscope, cut out by a laser, and then collected for subsequent analysis. Hunt et al. (2021) [19] demonstrated the benefits of investigating tumor tissue applying LCM in a 3-dimensional fashion. In this manner, detailed insights into tumor microenvironment heterogeneity are obtained, thereby getting access to prognostic signatures (biomarkers) and molecular cancer pathophysiology [19]. However, LCM is very time-consuming. The best results regarding the selection of target cells are obtained if the tissue is fixed by formalin, where the morphologic structure of the tissue is best preserved, guaranteeing high-quality microscopic images. For proteomics, formalin fixation results in a limited extraction efficiency, as well as the induction of irreversible chemical modification, finally leading to higher error rates and reduced protein numbers in protein identification from LC-MS/MS measurements [20].

A technique, overcoming several of the problems mentioned above, is the sampling and homogenization of tissue with an infrared (IR) laser. Scanning tissue with picosecond IR laser (PIRL) or nanosecond IR laser (NIRL) rapidly converts the tissue into an aerosol by soft cold vaporization. The tissue aerosol is already a homogenate. Additional homogenization is not required. A liquid condensate of the tissue aerosol after centrifugation shows no pellet.

Kwiatkowski et al. showed that, compared to mechanical homogenization, the yield and number of identified proteins increased significantly when a picosecond infrared laser (PIRL) was used [21]. Besides PIRL [21–23] and microsecond infrared laser (MIRL) [23], especially nanosecond infrared lasers (NIRL) with a pulse duration of about 7 ns, have been successfully utilized for tissue sampling prior to proteome analysis [24–26]. In the recent study by our group, Hahn et al. [26] revealed the clear distinguishability of murine colon and spleen tissue, based on >1000 identified proteins after collecting NIRL-induced tissue aerosols as condensates on glass cover slips, followed by bottom-up proteomics.

In this study, we used NIRL-based sampling to investigate the specific proteomes of different tissue cell layers of the intestine, using LC-MS/MS-based differential quantitative proteomics and following the hypothesis that cell-type-specific proteins are identified in the different colon cell layers.

2. Results

Two laser sampling studies of murine intestine tissue were performed to determine the applicability of NIRL ablation for three-dimensional sampling prior to quantitative differential proteomics.

2.1. Analysis of the Proteomes of Different Colon Regions

With the subsequent proteomic analysis of samples obtained by NIRL ablation of ascending (A), transversal (B), and descending (C) colon (Figure 1a), 3053 proteins were quantified ($n = 3$), yielded from an ablation area of about 5 mm²; and an ablation depth of 117 μm (approximately 0.6 μL).

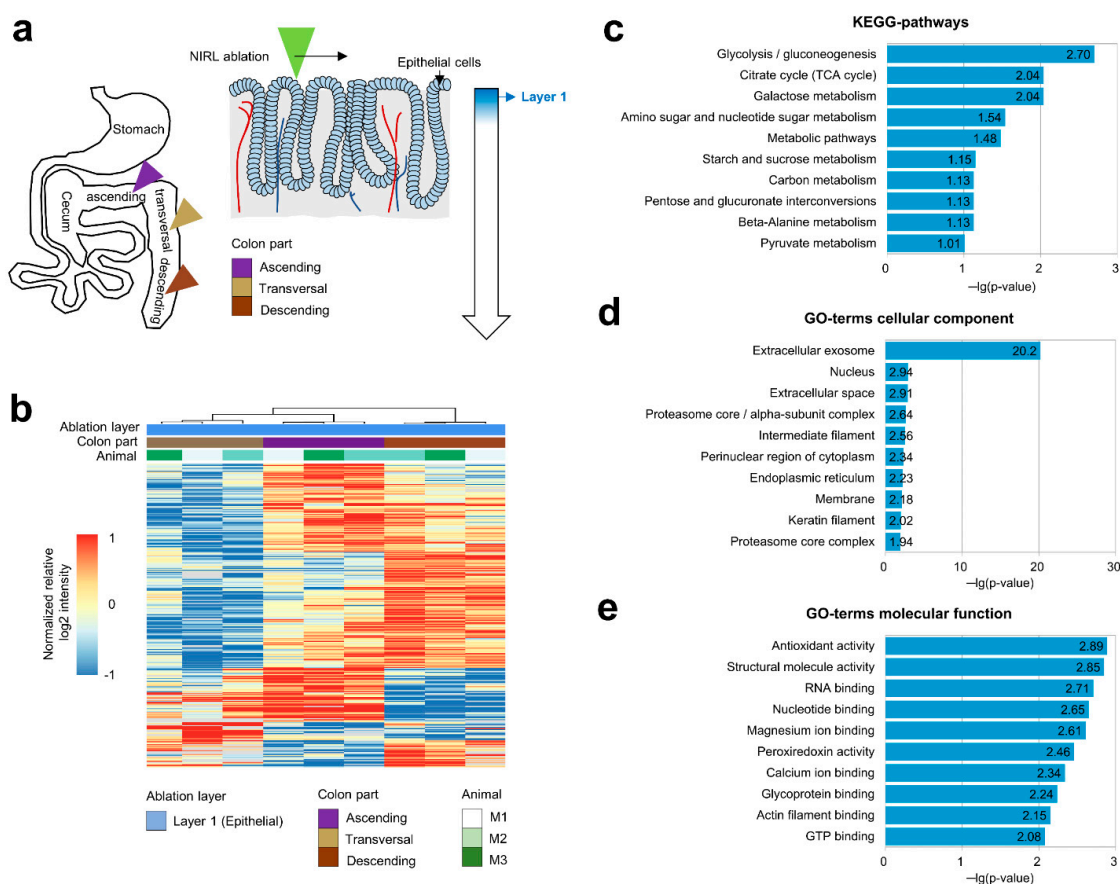


Figure 1. Comparison of epithelial protein signatures across different consecutive colon segments. (a) Schematic overview of the colon structure and the spatial location of ablated epithelial samples. (b) Hierarchical clustering of proteins between ascending, transversal, and descending colon epithelium. (c) Top 10 enriched terms (highest p -value) from KEGG-pathway-based DAVID enrichment of ANOVA significant proteins between ascending, transversal, and descending colon epithelium. (d,e) Top 10 enriched terms (highest p -value) from gene ontology (GO) cellular component-based and molecular function-based DAVID enrichment of ANOVA-significant proteins between ascending, transversal, and descending colon epithelium.

In total, 303 proteins were found to be, via ANOVA, significantly different (p -value < 0.05) (Figure 1b and Supplementary Table S1b). KEGG-pathway-based enrichment analysis of these proteins revealed that they were predominantly associated with metabolic processes (Figure 1c). An enrichment analysis based on gene ontology further indicated a predominant location of regulated proteins in extracellular exosomes (Figure 1d), as well as an enrichment of proteins with antioxidant activity among other terms (Figure 1c–e and Supplementary Table S1c–f).

2.2. Analysis of the Proteomes of Consecutive Colon Tissue Layers

Eight consecutive layers were sampled with NIRL and analyzed with differential quantitative proteomics, as shown in Figure 2a.

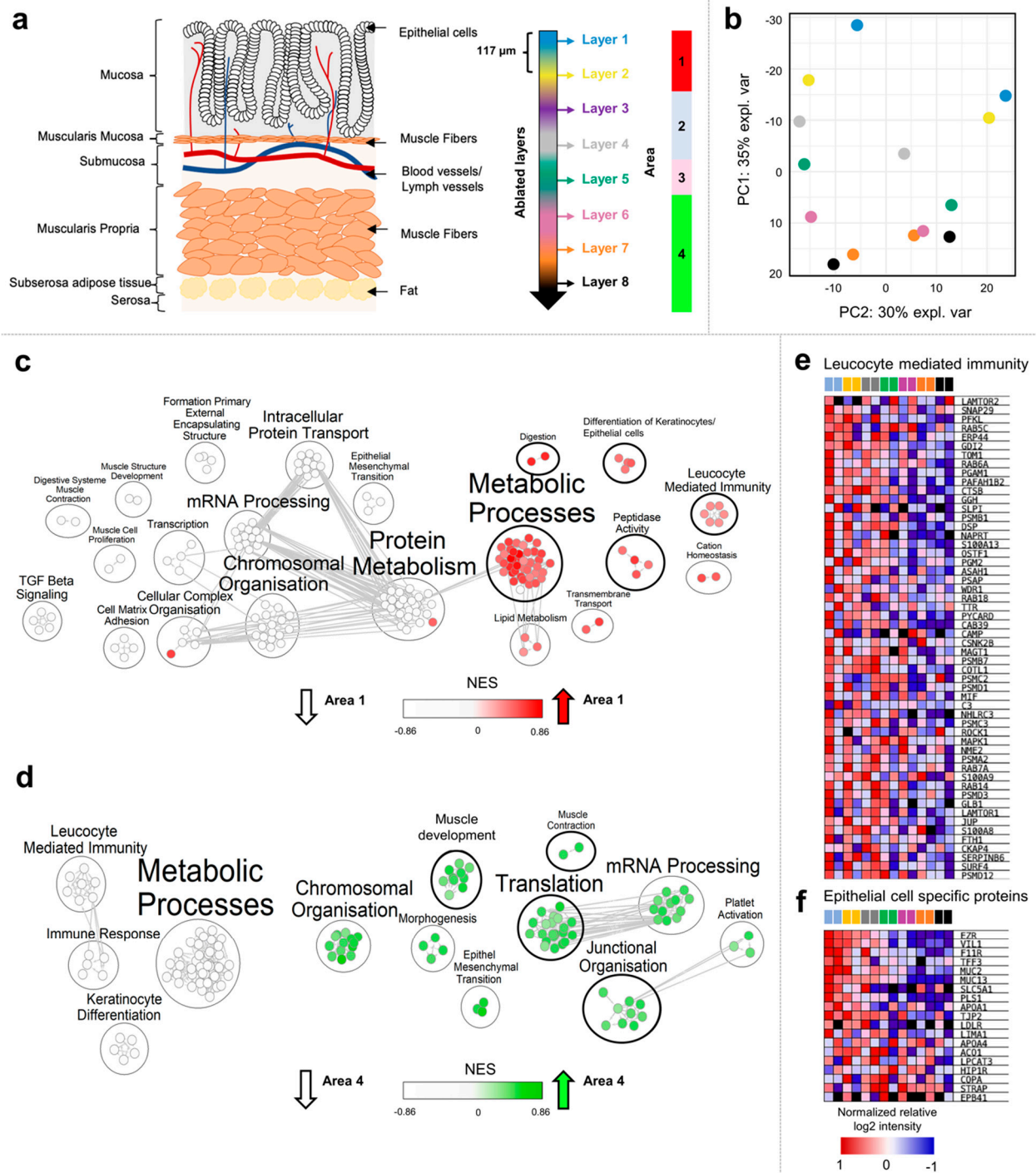


Figure 2. Comparison of different cellular layers of the murine intestine after NIRL ablation. (a) Schematic overview of the colon layer structure and the location of ablated layers and disclosed proteomic signatures along the sagittal axis of the colon. (b) Scatter plot visualization of the first 2 principal components from nonlinear iterative squares (NIPALS) PCA. (c) Positively (red) and negatively (white) enriched gene ontology biological processes (GO-PB) in area 1. (d) Positively (green) and negatively (white) enriched gene ontology biological processes (GO-PB) in area 4. Heatmap visualization of the relative abundance distribution of proteins assigned to the gene set “Leucocyte mediated immunity” (e) and to “Epithelial cell specific proteins” (f) across ablation layers.

In this study, a total of 2882 proteins were quantified (Supplementary Table S2a,b). Nonlinear-iterative-squares PCA revealed a separation of all ablated layers based on

2474 proteins that were found in at least 50% of all samples. Ablation layers formed a consecutive gradient along principal component (PC) one, accounting for 35% of the explained variance (Figure 2b and Supplementary Figure S3b). PC2, accounting for 30% of the explained variance, represented differences between the adjacent areas of the colon. To evaluate how many distinguishable cellular areas were represented across the ablated layers, Pearson correlation-based consensus clustering was applied (Supplementary Figures S1 and S2). To determine the optimal number of clusters, the proportion of ambiguous clustering (PAC) score was calculated, and we identified four differentiable protein patterns across the ablated layers (Supplementary Table S2c). The first area included the ablated layers one and two (0–234 μm). The second area comprised the ablated layers three and four (234–468 μm). Ablated layer five formed an individual area (468–585 μm). Based on the protein abundance distribution, a common area was defined for ablated layers 6–8 (585–939 μm). A total of 251 proteins were identified as statistically differential abundant across different cellular areas in ANOVA testing (p -value < 0.05) (Supplementary Table S2b). While clearly distinguishable proteome profiles were formed between cellular areas one and four. The Pearson-correlation-based hierarchical clustering revealed that the protein profiles of areas two and three showed high abundances of cell-type-specific proteins found in both areas one and four, respectively (Supplementary Figure S3). The Student's t -test revealed 164 statistically significant higher-abundance proteins for ablated area one and 103 higher abundant proteins for area four, respectively. For area two, seven higher-abundance proteins were identified, while only three showed an elevated intensity in area three (Supplementary Table S4).

To further determine the predominate cellular identity of areas one and four, gene ontology biological processes (GO-BP)-based gene-set enrichment was performed, comparing the proteome profile of areas one and four to all other cellular areas (Figure 2e,f and Supplementary Table S2d–g). The gene-set enrichment analysis (GSEA) revealed an enrichment of proteins associated with metabolic processes, digestion, lipid metabolism, peptidase activity, and cation homeostasis (Figure 2c). Furthermore, leucocyte (Figure 2e) and differentiation of epithelial-cell-specific proteins showed a higher abundance (Figure 2f) in cellular area one, decreasing toward cellular area four.

For cellular area four, an enrichment of proteins associated with muscle development, muscle contraction, morphogenesis, mRNA processing, chromosomal organization, and epithelial to mesenchymal transition was found (Figure 2d and Supplementary Figure S4). Based on the results of GSEA, a representation of the mucosa colon layer, including the leucocyte-infiltrated epithelium, can be suspected for the first two ablation layers. Furthermore, it can be assumed that ablation layers six to eight reflect the muscularis propria.

To further test this hypothesis, the abundance of established epithelial (*SFN*, *KRT18*, *VIL1*, *KRT20*, and *CDH1*) (Figure 3a) and muscular marker proteins (*MYL9*, *SMTN*, *CNN1*, *ACTA1*, and *TPM2*) (Supplementary Figure S3b) across different ablation layers was analyzed and compared to immunohistological (IHC) staining of the colon obtained from the Human Protein Atlas (v21.0.proteinatlas.org) [27].

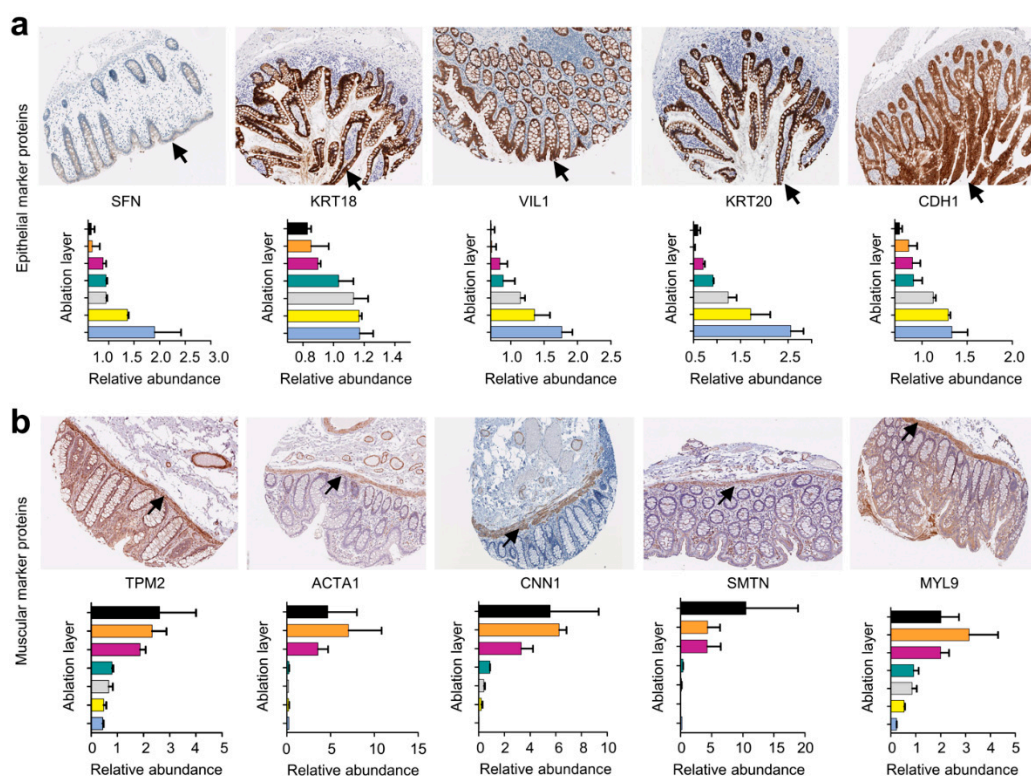


Figure 3. Abundance distribution of known epithelial and muscular proteins across different ablation layers. (a) Abundance distribution of established epithelial marker proteins (*SFN*, *KRT18*, *VIL1*, *KRT20*, and *CDH1*) across different ablation layers, associated with corresponding immunohistological staining of the human intestine, obtained from the Human Protein Atlas (v21.0.proteinatlas.org) [27]. (b) Abundance distribution of established muscular marker proteins (*TPM2*, *ACTA1*, *CNN1*, *SMTN*, and *MYL9*) across different ablation layers, with corresponding immunohistological staining of the human intestine, obtained from the Human Protein Atlas (v21.0.proteinatlas.org) [27].

For all epithelial marker proteins, the highest abundance was identified in the first ablation layer and gradually decreased toward the last ablation layer. These findings go in line with the IHC staining intensity of respective proteins in the human colon epithelium obtained from the Human Protein Atlas (v21.0.proteinatlas.org) [27]. For the ablation layers 6–8, a higher abundance of muscular marker proteins was found. IHC staining additionally confirmed a higher abundance of these proteins in the muscularis propria layer of the colon obtained from the Human Protein Atlas (v21.0.proteinatlas.org) [27].

3. Discussion

In this study, we applied consecutive NIRL-based sampling of colon for obtaining 3D-resolved samples for characterizing the proteomes of different specific areas of the tissue. In this way, we demonstrate the applicability of NIRL-based spatial sampling of tissues at lateral and in-depth resolution.

Addressing the importance of the localization of cells in organs, significant differences were shown between ascending (AC), descending (DC), and transversal (TV) colon. These differences between protein profiles of the epithelial cells of the mucosa of different areas of the colon are mostly assigned to metabolic processes (glycolysis, TCA cycle, amino acid, and sugar metabolism) and antioxidant activities. The predominant functions of the gastrointestinal tract are digestion, absorption of nutrients, secretion, and immune response and control [28]. Differences in the metabolome of AC and DC colon tissue, including the profiles of nucleotides, amino acids, and lipids, have been described for healthy, overweight, and obese adults, respectively [29]. To our knowledge, no study comparing the proteomic profiles of colon tissue in AC, DC, and TV colon has currently been performed. However,

the previously described findings at the metabolome level are in line with the changes at the proteome level described here and underline the successful laterally resolved proteome analysis of colon tissue after NIRL-based sampling.

In comparison to our most recent study [26], where 1617 proteins were identified from murine colon tissue, using a similar setup, we demonstrated a significant increase in the number of identified proteins (3053) for a comparable ablation volume (approximately 0.6 μL). This increased efficiency can be explained by direct trapping of the aerosol on a glass slide above the tissue sample and reducing the scanning area for the laser ablation by shifting of sample repeatedly. Since the scanning laser beam has to pass the glass slide, this scanning area is always lost (Supplementary Figure S1d,e). Furthermore, we increased the precision of the laser ablation by introducing a scan lens and synchronized laser triggering to the setup.

In the second part of the study, we aimed to investigate the applicability of NIRL-based tissue sampling for a three-dimensional (3D) analysis of colon tissue. Here, eight consecutive layers were ablated, covering a total depth of 936 μm in approximately 117 μm steps, to disclose the proteome of different cell layers of the intestine. Thereby, we obtained four different cell-layer-specific areas according to the proteome profiles of the eight different samples yielded by consecutive laser ablation. Hence, ablation layers one and two showed high abundances of epithelial- and leucocyte-specific proteins, indicating a representation of the mucosa cell layer of the intestine at an ablation depth of 0–234 μm , which predominantly consists of epithelial and immunological cells [28,30]. The higher abundance of muscle-cell-specific proteins in ablation layers 6–8 revealed a depiction of the muscularis propria at 585–936 μm , consisting of a large layer of smooth muscle cells arranged in parallel arrays [28]. Between 234 and 585 μm , two different cellular areas of the muscularis mucosa and submucosa were identified that showed high intensities of both muscle- and epithelium-specific proteins, respectively. This can be explained by the cellular architecture of the colon showing epithelial enclosures across all cellular layers, except for the muscularis propria [31]. Muscle-cell-specific profiles at respective ablation depths are represented due to the presence of smooth muscle cells in the muscularis mucosa [28].

While different cellular areas of the intestine could be differentiated, a single-cell-type resolution was not yet achieved in this study, which would particularly be important for studying the microenvironment of murine intestine in more detail. Nevertheless, NIRL ablation enabled a spatially resolved analysis of the colon, which was not possible before our study, with an in-depth resolution of about 117 μm .

In summary, we have shown for the first time that infrared laser ablation of tissue enables spatially resolved analysis of cell-layer-specific proteomes directly from intact fresh-frozen organs. While this technique successfully addresses the spatial aspect of tissues, in contrast to other approaches, NIRL ablation does not require additional steps to homogenize the tissue or extract the proteins, making it suitable for proteome analysis on a miniaturized scale.

4. Material and Methods

4.1. Animals

Mice aged 8–12 weeks old used in this study were on a C57/BL6 background. Mice were kept under specific pathogen free conditions, at an ambient temperature of 20 ± 2 °C, humidity of $55 \pm 10\%$, and a dark/light cycle of 12 h.

4.2. Ablation Setup

The experimental ablation setup is shown in Figure 4a.

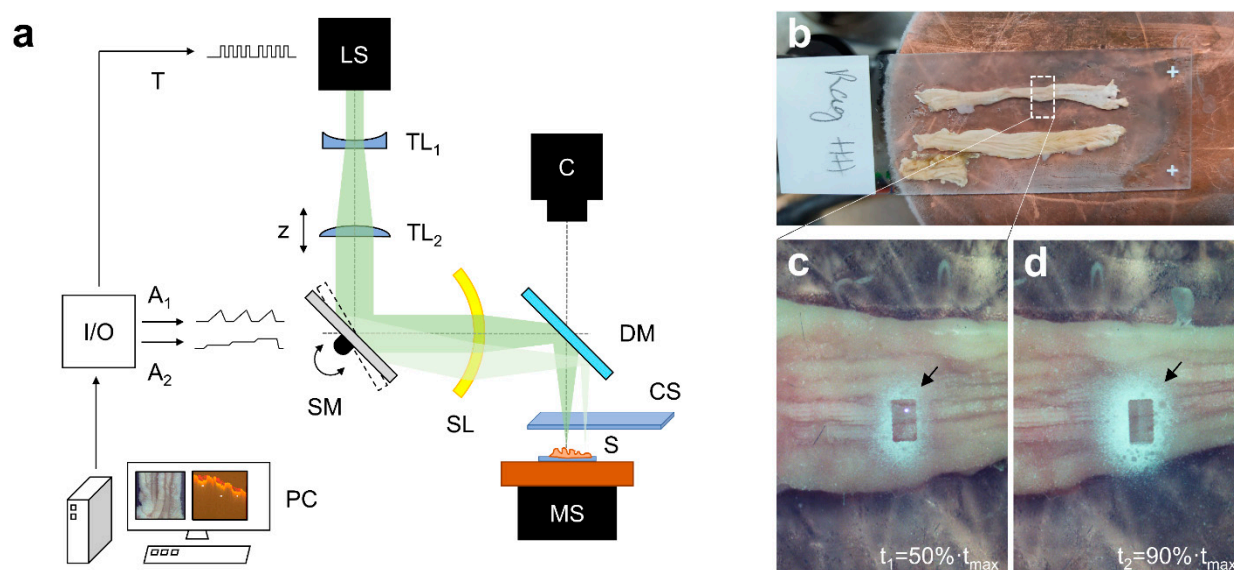


Figure 4. (a) Experimental ablation setup utilizing a nanosecond infrared laser system (LS) with a 2-axis scanning mirror (SM) in combination with a scanning lens (SL). A camera with objective (C) is monitoring the ablation of the sample (S) through a dichroitic mirror (DM). The sample is cooled down to about -10°C and can be displaced by a manual stage (MS). The aerosol is collected by a glass slide (CS), which is placed directly above the sample. PC, control computer; I/O, input/output card; $A_{1/2}$, analog line 1/2; T, trigger line; $TL_{1/2}$, telescope lens 1/2. (b) Murine colon that is transversally cut open and placed on an objective slide for better handling. In the region of interest, the colon is sampled layer-by-layer with NIRL. (c,d) Pictures of the ablation area at two time points (t_1 and t_2) of the ablation time (t_{\max}). The trapped and dried aerosol (black arrow) appears white on the glass slide. A rectangular area within the dried aerosol is lost due to the scanning process.

The beam of a nanosecond infrared laser system (LS) (Opolette SE 2731, Oportek, LLC, Carlsbad, CA, USA) with a pulse width of 7 ns and a tunable wavelength (2.70–3.10 μm) is widened and collimated by a Galaien telescope, consisting of a concave and a convex lens (ISP-PC-25-75 and ISP-PX-25-150, ISP Optics Latvia, LTD, Riga, Latvia). An f-theta scanning lens (SL1-2.94-36-10-100-U-A, II-VI, Inc., Saxonburg, PA, USA) with 100 mm focal length in combination with a 2-axis scanning mirror (OIM202, Optics in Motion LLC, Long Beach, CA, USA) is used to scan the frozen sample, located on a manual xy-stage (XR25P-K1/M, Thorlabs, Newton, NJ, USA) with a custom-built cooling system. The computer synchronizes the scanning mirror with the laser system, using two analog lines and a digital trigger line of an input/output card (USB-6343, National Instruments, Austin, TX, USA). A glass slide (SuperFrost[®] microscope slides, R. Langenbrinck GmbH, Emmendingen, Germany) on a manual xyz-stage (XR25P-K2/M, Thorlabs, Newton, NJ, USA) set is mounted closely above the ablation site to collect the aerosol. The ablation can be observed with a microscope camera (DFK 23UP031, The Imaging Source, Bremen, Germany) through a dichroitic mirror (Separator 109093, Layertec GmbH, Jena, Germany).

4.3. Tissue Sampling and Collection Procedure

For the study on murine colon, the laser wavelength was set to 2.85 μm . A preliminary study showed a maximum protein amount, determined with BCA tests, at this wavelength for this tissue type. The pulse energy was measured to be 0.9 mJ at sample position, corresponding to a fluence of 18.1 J/cm^2 with focal spot dimensions of about $dx = 125 \mu\text{m}$ and $dy = 100 \mu\text{m}$ in diameter, respectively.

Positively charged glass slides (SuperFrost[®], microscope slides, R. Langenbrinck GmbH, Emmendingen, Germany) are placed directly above the tissue at the ablation area to trap the resulting aerosol with the charged side facing the sample (Figure 4c,d). To

increase yield of the trapped aerosol, the beam scanning area was reduced to $1 \times 0.5 \text{ mm}^2$; (Figure 4d, black arrow). Optimal laser focus positioning was achieved by synchronizing a two-axis scanning mirror in combination with a f-theta scan lens of 100 mm focal length with the laser pulse triggering, utilizing a fast input/output card. The custom-made control software enables high-precision placement of the focal laser spot by introducing wait times to let the scanning mirror reach its position and swing out. The integrated monitoring camera with zoom objective was used for calibrating and monitoring lateral spot positioning. Optimal axial positioning of the sample was achieved by observing the dimensions of laser shots on photo paper at different z-positions with reduced laser energy.

After each ablation of a layer set, the sample stage was manually shifted laterally (x-direction) for $600 \mu\text{m}$ to extend the ablation area to about 5 mm^2 .

After completion of the sampling, the dried aerosol was dissolved with $100 \mu\text{L}$ of buffer (0.1 M triethylammonium bicarbonate buffer with 1% sodium deoxycholate), using four pipetting steps with $25 \mu\text{L}$ to reduce the contact area of the protein solution with the glass surface. The removed glass slide was then replaced with a new one for the next layer.

Using this optimized laser setup, two laser ablation experiments were performed in the murine intestine, while obtaining the spatial information of the sample:

1. In the first experiment, one layer was ablated at ascending (A), transversal (B), and descending (C) colon, respectively.
2. In the second experiment, 8 consecutive layers were ablated.

4.4. Determination of Layer Thickness

Layer thickness was determined by utilizing a spectral domain optical coherence tomography system (TEK221PSC2-SP1, Thorlabs, Newton, NJ, USA) with a central wavelength of 1300 nm and the imaging volume set to $699 \times 699 \times 768$ voxels, each measuring $8.58 \times 8.58 \times 3.45 \mu\text{m}^3$ in air. The measurements were performed on three ablations on an additional frozen colon at three different positions (Ab1, Ab2, and Ab3) (Figure 5a–c). Ablation depth was determined (see Figure 5c) at each of the ablation sites, based on 10 random distance measurements, revealing depths of $226 \pm 17 \mu\text{m}$, $245 \pm 14 \mu\text{m}$, and $203 \pm 20 \mu\text{m}$, respectively. The mean layer depth over all ablation sites was determined to about $117 \mu\text{m}$. This value was used for all further considerations.

The ablation parameters for spacing were kept to $143 \mu\text{m} \times 125 \mu\text{m}$, the ablation area was reduced to $1 \text{ mm} \times 1 \text{ mm}$, and the number of ablation layers was reduced to 2. First the OCT image data sets (before and after ablation) were preprocessed (window/level, blur filter, cropped) with Fiji (ImageJ 1.53f51) [32] and afterward registered with the Fiji plugin Fijiyama (version “handsome honeysuckle”) [33] to generate an overlay image stack and determine ablation volume dimensions. For volume quantification and mean depth determination (Supplementary Table S3), the open-source software ITK-Snap (Version 3.8.0 [34]) with its onboard measuring tools was used.

4.5. Tryptic Digestion of Proteins of the Ablated Tissue Samples

The dissolved aerosols were heated and mixed 10 min at $99 \text{ }^\circ\text{C}$, at a rotation speed of 400 rpm, using a shaker (ThermoMixC[®], Eppendorf SE, Hamburg, Germany). Sonification was performed for 5 pulses at 30% power. Disulfide bonds were reduced with 10 mM DTT at $60 \text{ }^\circ\text{C}$ for 30 min. Cysteine residues were alkylated with 20 mM iodoacetamide (IAA) for 30 min at $37 \text{ }^\circ\text{C}$ in the dark. Tryptic digestion was performed for 16 h at $37 \text{ }^\circ\text{C}$, using 250 ng trypsin. After tryptic digestion, the inhibition of trypsin activity, as well as the precipitation of sodium deoxycholate, was achieved by the addition of 1% formic acid (FA). Samples were centrifuged for 5 min at $14,000 \times g$. The supernatant was collected, dried in a vacuum concentrator centrifuge (UNIVAPO 100 H, UniEquip, Martinsried, Germany), and stored at $-20 \text{ }^\circ\text{C}$ until further use. Prior to mass spectrometric analyses, peptides were resuspended in $10 \mu\text{L}$ of 0.1% FA.

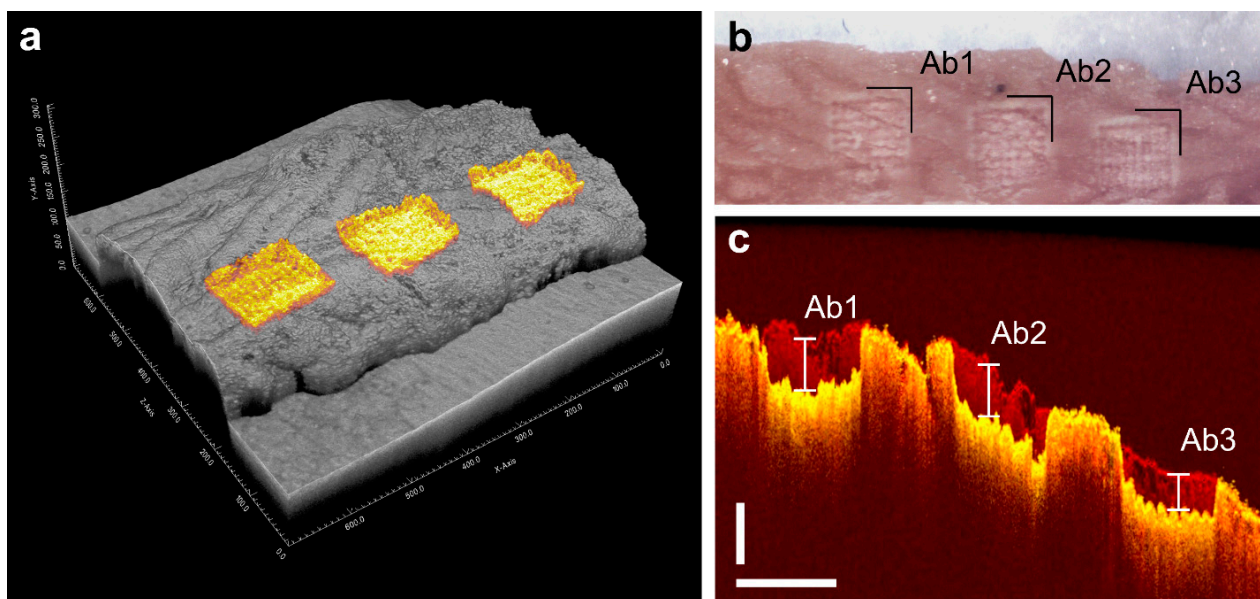


Figure 5. (a) Three-dimensional reconstruction of the two registered OCT volumes before and after the laser ablation, with the ablation surfaces highlighted in yellow. (b) Picture of the murine colon after the ablation of 2 layers at three positions along a line. (c) Example OCT brightness scan (B-scan) of the two registered volumes before (red) and after (yellow) ablation with depth measuring markings for the three ablations Ab1, Ab2, and Ab3. Scale bars measure 250 μm vertical and 500 μm horizontal, respectively.

4.6. LC-MS/MS Data Acquisition

Liquid chromatography–tandem mass spectrometer (LC-MS/MS) measurements were performed on a quadrupole-ion-trap-orbitrap MS (Orbitrap Fusion, Thermo Fisher Scientific, Waltham, MA, USA) coupled to a nano-UPLC (Dionex Ultimate 3000 UPLC system, Thermo Fisher Scientific, Waltham, MA, USA). Tryptic peptides were injected to the LC system via an autosampler, purified and desalted by using a reversed phase trapping column (Acclaim PepMap 100 C18 trap; 100 $\mu\text{m} \times 2 \text{ cm}$, 100 Å pore size, 5 μm particle size; Thermo Fisher Scientific, Waltham, MA, USA), and thereafter separated with a reversed phase column (Acclaim PepMap 100 C18; 75 $\mu\text{m} \times 50 \text{ cm}$, 100 Å pore size, 2 μm particle size, Thermo Fisher Scientific, Waltham, MA, USA). Trapping was performed for 5 min at a flow rate of 5 $\mu\text{L}/\text{min}$ with 99% solvent A (0.1% FA) and 1% solvent B (0.1% FA in ACN). Separation and elution of peptides were achieved by a linear gradient from 1 to 30% solvent B in 70 min at a flow rate of 0.3 $\mu\text{L}/\text{min}$. Eluting peptides were ionized by using a nano-electrospray ionization source (nano-ESI) with a spray voltage of 1800 V, transferred into the MS and analyzed in data dependent acquisition (DDA) mode. For each MS1 scan, ions were accumulated for a maximum of 120 ms or until a charge density of 2×10^5 ions (AGC target) was reached. Fourier-transformation-based mass analysis of the data from the orbitrap mass analyzer was performed by covering a mass range of 400–1300 m/z with a resolution of 120,000 at $m/z = 200$. Peptides with charge states between 2+–5+ above an intensity threshold of 1000 were isolated within a 1.6 m/z isolation window in top-speed mode for 3 s from each precursor scan and fragmented with a normalized collision energy of 30%, using higher energy collisional dissociation (HCD). MS2 scanning was performed, using an ion trap mass analyzer, covering a mass range of 380–1500 m/z with an orbitrap resolution of 15,000 at $m/z = 200$ and accumulated for 60 ms or to an AGC target of 1×10^5 . Already fragmented peptides were excluded for 30 s

4.7. Raw Data Processing

Raw data from LC-MS/MS measurements were processed with MaxQuant (version 1.6.2.10, Max Planck Institute for Biochemistry, Martinsried, Germany), using the integrated

Andromeda algorithm. For protein identification, measured MS2 spectra were searched against theoretical fragment-spectra of tryptic peptides, generated from a reviewed murine Swiss-Prot FASTA database obtained in February 2020 containing 17,015 entries. All samples were handled as individual experiments. The carbamethylation of cysteine residues was set as a fixed modification. methionine oxidation, protein N-terminal acetylation, removal of the initiator methionine at the protein N-terminus and the conversion of glutamine to pyroglutamate were set as variable modifications. Peptides with a minimum length of 6 amino acids and a maximum mass of 6000 Da were identified with a mass tolerance of 10 ppm. Only peptides with a maximum of two missed trypsin cleavage sites were considered. For peptide identification, matching between runs was applied, using a match time window of 0.7 min and an alignment time window of 20 min between individual runs. The error tolerance was set to 20 ppm for the first precursor search and to 4.5 ppm for the following main search. Fragment spectra were matched with 20 ppm error tolerance. A false discovery rate (FDR) value threshold <0.01, using a reverted decoy peptide database approach was set for peptide identification. Label free quantification was performed with an LFQ minimum ratio count of 1. For quantification, all identified razor and unique peptides were considered. The label minimum ratio count was set to 1.

4.8. Data Analysis and Visualization

Identified protein group abundances were loaded into Perseus (version 1.6.15.0, Max Planck Institute for Biochemistry, Martinsried, Germany), log₂ transformed and normalized to the total protein amount per sample to compensate for variations in the injected sample amount. For the analysis of the proteomes of consecutive colon layers, one replicate of layer 3 (depth of 234–351 μm) was excluded due to high yields of blood proteins. Hence, for further statistical testing layer three was excluded due to the absence of replicates.

For ANOVA and t-testing a *p*-value cutoff < 0.05 was set. *p*-value significant proteins with a foldchange difference <1.5 were considered for further analysis after t-testing.

Nonlinear Iterative vertical Least Squares (NIPALS) PCA and hierarchical clustering were performed in the R software environment (version 4.1.3). For Principal component calculation and visualization, the mixOmics package was used in Bioconductor (version 3.14) [35] Hierarchical clustering was performed based on centered and normalized abundances using the heatmap package. Pearson correlation was applied as a distance metric. Ward.D linkage was applied. Missing data in correlation distances was pairwise complete correlation.

To determine the number of distinguishable molecular clusters between different ablation layers, consensus clustering was applied, using the ConsensusClusterPlus package [36]. Pearson correlation was applied as a distance metric. Ward.D linkage was used. Pairwise complete correlation was used to deal with missing values in the generation of Pearson correlation matrices. The number of subsamples was set to 1000 M maximum number of 7 clusters, corresponding to the total number of ablation layers that were used. Reactome-based [37] Gene Set Enrichment Analysis (GSEA) was performed by using the software GSEA (version 4.1, Broad Institute, San Diego, CA, USA), [38] based on log₂-transformed normalized protein abundances. One hundred permutations were used. Permutation was performed based on gene sets. A weighted enrichment statistic was applied, using the signal-to-noise ratio as a metric for ranking genes. No additional normalization was applied within GSEA. Gene sets smaller than 15 and bigger than 500 genes were excluded from analysis. For visualization of GSEA results, the Cytoscape environment (version 3.8.2) [39] was used. The EnrichmentMap (version 3.3) [40] application was used. Gene sets were considered if they were identified at an FDR < 0.25 and a *p*-value < 0.1. For gene-set-similarity filtering, data set edges were set automatically. A combined Jaccard and Overlap metric was used, applying a cutoff of 0.375. For gene set clustering, AutoAnnotate (version 1.3) [41] was applied. A cluster algorithm Markov cluster algorithm (MCL) was used. The gene-set-similarity coefficient was utilized for edge weighting. Individually

analyzes gene sets (leucocyte mediated immunity; keratinocyte/epithelial signatures) were obtained from the molecular signature database (version 3.0) [42].

For the enrichment analysis of ANOVA significant proteins, the DAVID functional annotation tool (version 6.8) [43] was used based on all gene ontology (GO) terms [44]. Terms enriched with a p -value < 0.01 were considered significantly enriched.

4.9. Histological Staining

Immunohistological stainings of the human intestine for selected muscular and epithelial marker proteins were obtained from the Human Protein Atlas (v21.0.proteinatlas.org) [27]. The following images were used:

1. *SFN* (<https://www.proteinatlas.org/ENSG00000175793-SFN/tissue/colon#img>), accessed on 29 April 2022;
2. *KRT18* (<https://www.proteinatlas.org/ENSG00000111057-KRT18/tissue/colon#img>), accessed on 29 April 2022;
3. *VIL1* (<https://www.proteinatlas.org/ENSG00000127831-VIL1/tissue/colon#img>), accessed on 29 April 2022;
4. *KRT20* (<https://www.proteinatlas.org/ENSG00000171431-KRT20/tissue/colon#img>), accessed on 29 April 2022;
5. *CDH1* (<https://www.proteinatlas.org/ENSG00000039068-CDH1/tissue/colon#img>), accessed on 29 April 2022;
6. *TPM2* (<https://www.proteinatlas.org/ENSG00000198467-TPM2/tissue/colon#img>), accessed on 29 April 2022;
7. *ACTA1* (<https://www.proteinatlas.org/ENSG00000143632-ACTA1/tissue/colon#img>), accessed on 29 April 2022;
8. *CNN1* (<https://www.proteinatlas.org/ENSG00000130176-CNN1/tissue/colon#img>), accessed on 29 April 2022;
9. *SMTN* (<https://www.proteinatlas.org/ENSG00000183963-SMTN/tissue/colon#img>), accessed on 29 April 2022;
10. *MYL9* (<https://www.proteinatlas.org/ENSG00000101335-MYL9/tissue/colon#img>), accessed on 29 April 2022.

Supplementary Materials: The following supporting information can be downloaded at: <https://www.mdpi.com/article/10.3390/ijms23116132/s1>.

Author Contributions: Conceptualization, J.H., N.G., H.V., M.M., S.H. and H.S.; methodology, J.H., H.V., V.N. and M.M.; software and validation, J.H., H.V., V.N. and M.M.; formal analysis, H.V., M.M. and J.H.; investigation, J.H. and P.P.; resources, S.H. and H.S.; writing, J.H., M.M., H.V., H.S., P.P. and S.H. All authors have read and agreed to the published version of the manuscript.

Funding: This research was funded by the “Landesforschungsförderung” (LFF) of the city of Hamburg (grant number LFF-FV-75). This study was also partly supported by grants from the “Deutsche Forschungsgemeinschaft” (DFG) (INST 337/15-1, INST 337/16-1, and INST 152/837-1). Furthermore, this work was supported by intramural funding from the faculty.

Institutional Review Board Statement: The study was conducted according to the guidelines of the Declaration of Helsinki and approved by the Institutional Review Board of “Behörde für Soziales, Familie, Gesundheit und Verbraucherschutz” (identification code ORG 934, date of approval: 5 October 2018, Hamburg, Germany).

Informed Consent Statement: Not applicable.

Data Availability Statement: Mass spectrometric data generated in this study can be accessed through the ProteomeXchange Consortium via the PRIDE partner repository with the dataset identifier PXD033584.

Acknowledgments: We thank Esther R. Lange for measurements in the OCT data sets.

Conflicts of Interest: The authors declare no conflict of interest.

References

1. Kim, J.; Koo, B.-K.; Knoblich, J.A. Human organoids: Model systems for human biology and medicine. *Nat. Rev. Mol. Cell Biol.* **2020**, *21*, 1–14. [[CrossRef](#)]
2. Cañas, B.; Piñeiro, C.; Calvo, E.; López-Ferrer, D.; Gallardo, J.M. Trends in sample preparation for classical and second generation proteomics. *J. Chromatogr. A* **2007**, *1153*, 235–258. [[CrossRef](#)]
3. Straube, H.; Witte, C.-P.; Herde, M. Analysis of Nucleosides and Nucleotides in Plants: An Update on Sample Preparation and LC–MS Techniques. *Cells* **2021**, *10*, 689. [[CrossRef](#)]
4. Höring, M.; Krautbauer, S.; Hiltl, L.; Babl, V.; Sigrüener, A.; Burkhardt, R.; Liebisch, G. Accurate Lipid Quantification of Tissue Homogenates Requires Suitable Sample Concentration, Solvent Composition, and Homogenization Procedure—A Case Study in Murine Liver. *Metabolites* **2021**, *11*, 365. [[CrossRef](#)]
5. Menzi, N.; Osinga, R.; Todorov, A.; Schaefer, D.J.; Martin, I.; Scherberich, A. Wet milling of large quantities of human excision adipose tissue for the isolation of stromal vascular fraction cells. *Cytotechnology* **2018**, *70*, 807–817. [[CrossRef](#)]
6. Goldberg, S. Mechanical/physical methods of cell disruption and tissue homogenization. *Methods Mol. Biol.* **2008**, *434*, 3–22.
7. Gross, V.; Carlson, G.; Kwan, A.T.; Smejkal, G.; Freeman, E.; Ivanov, A.R.; Lazarev, A. Tissue fractionation by hydrostatic pressure cycling technology: The unified sample preparation technique for systems biology studies. *J. Biomol. Tech. JBT* **2008**, *19*, 189–199.
8. Kehm, R.; Baldensperger, T.; Raupbach, J.; Höhn, A. Protein oxidation-Formation mechanisms, detection and relevance as biomarkers in human diseases. *Redox Biol.* **2021**, *42*, 101901. [[CrossRef](#)]
9. Auclair, J.R.; Salisbury, J.; Johnson, J.L.; Petsko, G.A.; Ringe, D.; Bosco, D.A.; Agar, N.Y.R.; Santagata, S.; Durham, H.D.; Agar, J.N. Artifacts to avoid while taking advantage of top-down mass spectrometry based detection of protein S-thiolation. *Proteomics* **2014**, *14*, 1152–1157. [[CrossRef](#)]
10. Ji, Y.; Liu, M.; Bachschmid, M.M.; Costello, C.E.; Lin, C. Surfactant-Induced Artifacts during Proteomic Sample Preparation. *Anal. Chem.* **2015**, *87*, 5500–5504. [[CrossRef](#)]
11. Bodzoń-Kulakowska, A.; Bierzynska-Krzysik, A.; Dylag, T.; Drabik, A.; Suder, P.; Noga, M.; Jarzebinska, J.; Silberring, J. Methods for samples preparation in proteomic research. *J. Chromatogr. B* **2007**, *849*, 1–31. [[CrossRef](#)]
12. Gil, A.; Siegel, D.; Permentier, H.; Reijngoud, D.-J.; Dekker, F.; Bischoff, R. Stability of energy metabolites—An often overlooked issue in metabolomics studies: A review. *Electrophoresis* **2015**, *36*, 2156–2169. [[CrossRef](#)]
13. Svensson, M.; Borén, M.; Sköld, K.; Fälth, M.; Sjögren, B.; Andersson, M.; Svenningsson, P.; Andrén, P.E. Heat Stabilization of the Tissue Proteome: A New Technology for Improved Proteomics. *J. Proteome Res.* **2009**, *8*, 974–981. [[CrossRef](#)]
14. Stingl, C.; Söderquist, M.; Karlsson, O.; Borén, M.; Luider, T.M. Uncovering Effects of Ex Vivo Protease Activity during Proteomics and Peptidomics Sample Extraction in Rat Brain Tissue by Oxygen-18 Labeling. *J. Proteome Res.* **2014**, *13*, 2807–2817. [[CrossRef](#)]
15. Sköld, K.; Alm, H.; Scholz, B. The Impact of Biosampling Procedures on Molecular Data Interpretation. *Mol. Cell. Proteom.* **2013**, *12*, 1489–1501. [[CrossRef](#)]
16. Doll, S.; Dreßen, M.; Geyer, P.E.; Itzhak, D.; Braun, C.; Doppler, S.A.; Meier, F.; Deutsch, M.-A.; Lahm, H.; Lange, R.; et al. Region and cell-type resolved quantitative proteomic map of the human heart. *Nat. Commun.* **2017**, *8*, 1–13. [[CrossRef](#)]
17. Mertins, P.; Tang, L.C.; Krug, K.; Clark, D.J.; Gritsenko, M.A.; Chen, L.; Clauser, K.R.; Clauss, T.R.; Shah, P.; Gillette, M.A.; et al. Reproducible workflow for multiplexed deep-scale proteome and phosphoproteome analysis of tumor tissues by liquid chromatography–mass spectrometry. *Nat. Protoc.* **2018**, *13*, 1632–1661. [[CrossRef](#)]
18. Emmert-Buck, M.R.; Bonner, R.F.; Smith, P.D.; Chuaqui, R.F.; Zhuang, Z.; Goldstein, S.R.; Weiss, R.A.; Liotta, L.A. Laser capture microdissection. *Science* **1996**, *274*, 998–1001. [[CrossRef](#)]
19. Hunt, A.L.; Bateman, N.W.; Barakat, W.; Makohon-Moore, S.; Hood, B.L.; Conrads, K.A.; Zhou, M.; Calvert, V.; Pierobon, M.; Loffredo, J.; et al. Extensive three-dimensional intratumor proteomic heterogeneity revealed by multiregion sampling in high-grade serous ovarian tumor specimens. *iScience* **2021**, *24*, 102757. [[CrossRef](#)]
20. Magdeldin, S.; Yamamoto, T. Toward deciphering proteomes of formalin-fixed paraffin-embedded (FFPE) tissues. *Proteomics* **2012**, *12*, 1045–1058. [[CrossRef](#)]
21. Kwiatkowski, M.; Wurlitzer, M.; Omid, M.; Ren, L.; Kruber, S.; Nimer, R.; Robertson, W.D.; Horst, P.-D.D.A.; Miller, R.J.D.; Schlüter, H. Ultrafast Extraction of Proteins from Tissues Using Desorption by Impulsive Vibrational Excitation. *Angew. Chem. Int. Ed.* **2014**, *54*, 285–288. [[CrossRef](#)]
22. Kwiatkowski, M.; Wurlitzer, M.; Krutilin, A.; Kiani, P.; Nimer, R.; Omid, M.; Mannaa, A.; Bussmann, T.; Bartkowiak, K.; Kruber, S.; et al. Homogenization of tissues via picosecond-infrared laser (PIRL) ablation: Giving a closer view on the in-vivo composition of protein species as compared to mechanical homogenization. *J. Proteom.* **2016**, *134*, 193–202. [[CrossRef](#)]
23. Krutilin, A.; Maier, S.; Schuster, R.; Kruber, S.; Kwiatkowski, M.; Robertson, W.D.; Hansen, N.-O.; Miller, R.J.D.; Schlüter, H. Sampling of Tissues with Laser Ablation for Proteomics: Comparison of Picosecond Infrared Laser and Microsecond Infrared Laser. *J. Proteome Res.* **2019**, *18*, 1451–1457. [[CrossRef](#)]
24. Dong, C.; Richardson, L.T.; Solouki, T.; Murray, K.K. Infrared Laser Ablation Microsampling with a Reflective Objective. *J. Am. Soc. Mass Spectrom.* **2022**, *33*, 463–470. [[CrossRef](#)]
25. Donnarumma, F.; Murray, K.K. Laser ablation sample transfer for localized LC-MS/MS proteomic analysis of tissue. *J. Mass Spectrom.* **2016**, *51*, 261–268. [[CrossRef](#)]
26. Hahn, J.; Moritz, M.; Voß, H.; Pelczar, P.; Huber, S.; Schlüter, H. Tissue Sampling and Homogenization in the Sub-Microliter Scale with a Nanosecond Infrared Laser (NIRL) for Mass Spectrometric Proteomics. *Int. J. Mol. Sci.* **2021**, *22*, 10833. [[CrossRef](#)]

27. Uhlén, M.; Fagerberg, L.; Hallström, B.M.; Lindskog, C.; Oksvold, P.; Mardinoglu, A.; Sivertsson, Å.; Kampf, C.; Sjöstedt, E.; Asplund, A.; et al. Tissue-based map of the human proteome. *Science* **2015**, *347*, 6220. [[CrossRef](#)]
28. Johnson, L.R. Regulation of gastrointestinal mucosal growth. *Physiol. Rev.* **1988**, *68*, 456–502. [[CrossRef](#)]
29. Baxter, B.A.; Parker, K.D.; Nosler, M.J.; Rao, S.; Craig, R.; Seiler, C.; Ryan, E.P. Metabolite profile comparisons between ascending and descending colon tissue in healthy adults. *World J. Gastroenterol.* **2020**, *26*, 335–352. [[CrossRef](#)]
30. Jensen, S.R.; Schoof, E.M.; Wheeler, S.E.; Hvid, H.; Ahnfelt-Rønne, J.; Hansen, B.F.; Nishimura, E.; Olsen, G.S.; Kislinger, T.; Brubaker, P.L. Quantitative Proteomics of Intestinal Mucosa From Male Mice Lacking Intestinal Epithelial Insulin Receptors. *Endocrinology* **2017**, *158*, 2470–2485. [[CrossRef](#)]
31. Lyons, J.; Ghazi, P.C.; Starchenko, A.; Tovaglieri, A.; Baldwin, K.R.; Poulin, E.J.; Gierut, J.J.; Genetti, C.; Yajnik, V.; Breault, D.T.; et al. The colonic epithelium plays an active role in promoting colitis by shaping the tissue cytokine profile. *PLoS Biol.* **2018**, *16*, e2002417. [[CrossRef](#)]
32. Schindelin, J.; Arganda-Carreras, I.; Frise, E.; Kaynig, V.; Longair, M.; Pietzsch, T.; Preibisch, S.; Rueden, C.; Saalfeld, S.; Schmid, B.; et al. Fiji: An open-source platform for biological-image analysis. *Nat. Methods* **2012**, *9*, 676–682. [[CrossRef](#)]
33. Fernandez, R.; Moisy, C. FijiYama: A registration tool for 3D multimodal time-lapse imaging. *Bioinformatics* **2020**, *37*, 1482–1484. [[CrossRef](#)]
34. Yushkevich, P.A.; Piven, J.; Hazlett, H.C.; Smith, R.G.; Ho, S.; Gee, J.C.; Gerig, G. User-guided 3D active contour segmentation of anatomical structures: Significantly improved efficiency and reliability. *NeuroImage* **2006**, *31*, 1116–1128. [[CrossRef](#)]
35. Rohart, F.; Gautier, B.; Singh, A.; Lê Cao, K.-A. mixOmics: An R package for 'omics feature selection and multiple data integration. *PLoS Comput. Biol.* **2017**, *13*, e1005752. [[CrossRef](#)]
36. Wilkerson, M.D.; Hayes, D.N. ConsensusClusterPlus: A class discovery tool with confidence assessments and item tracking. *Bioinformatics* **2010**, *26*, 1572–1573. [[CrossRef](#)]
37. Fabregat, A.; Jupe, S.; Matthews, L.; Sidiropoulos, K.; Gillespie, M.; Garapati, P.; Haw, R.; Jassal, B.; Korninger, F.; May, B.; et al. The Reactome Pathway Knowledgebase. *Nucleic Acids Res.* **2018**, *46*, D649–D655. [[CrossRef](#)] [[PubMed](#)]
38. Subramanian, A.; Tamayo, P.; Mootha, V.K.; Mukherjee, S.; Ebert, B.L.; Gillette, M.A.; Paulovich, A.; Pomeroy, S.L.; Golub, T.R.; Lander, E.S.; et al. Gene set enrichment analysis: A knowledge-based approach for interpreting genome-wide expression profiles. *Proc. Natl. Acad. Sci. USA* **2005**, *102*, 15545–15550. [[CrossRef](#)]
39. Shannon, P.; Markiel, A.; Ozier, O.; Baliga, N.S.; Wang, J.T.; Ramage, D.; Amin, N.; Schwikowski, B.; Ideker, T. Cytoscape: A software environment for integrated models of Biomolecular Interaction Networks. *Genome Res.* **2003**, *13*, 2498–2504. [[CrossRef](#)]
40. Merico, D.; Isserlin, R.; Stueker, O.; Emili, A.; Bader, G.D. Enrichment Map: A Network-Based Method for Gene-Set Enrichment Visualization and Interpretation. *PLoS ONE* **2010**, *5*, e13984. [[CrossRef](#)]
41. Millán, P.P.; Kucera, M.; Isserlin, R.; Arkhangorodsky, A.; Bader, G.D. Referee report. For: AutoAnnotate: A Cytoscape app for summarizing networks with semantic annotations [version 1; referees: 1 approved]. *Natl. Cent. Biotechnol. Inf.* **2016**, *5*, 1717. [[CrossRef](#)]
42. Liberzon, A.; Birger, C.; Thorvaldsdóttir, H.; Ghandi, M.; Mesirov, J.P.; Tamayo, P. The Molecular Signatures Database Hallmark Gene Set Collection. *Cell Syst.* **2015**, *1*, 417–425. [[CrossRef](#)] [[PubMed](#)]
43. Dennis, G.; Sherman, B.T.; Hosack, D.A.; Yang, J.; Gao, W.; Lane, H.C.; Lempicki, R.A. DAVID: Database for Annotation, Visualization, and Integrated Discovery. *Genome Biol.* **2003**, *4*, 5. [[CrossRef](#)]
44. Harris, M.A. The Gene Oncology (GO) database and informatics resource. *Nucleic Acids Res.* **2004**, *32*, 258–261.

5.4 DIRECT 3D SAMPLING OF THE EMBRYONIC MOUSE HEAD: LAYER-WISE NANOSECOND INFRARED LASER (NIRL) ABLATION FROM SCALP TO CORTEX FOR SPATIALLY RESOLVED PROTEOMICS

Jelena Navolić*, Manuela Moritz*, Hannah Voß, Simon Schlumbohm, Yannis Schumann, Hartmut Schlüter, Julia E. Neumann, and Jan Hahn

Analytical Chemistry **2023**, 95, 47, 17220-17227

*Shared first authorship

In the previously reported proteomics study of Voß & Moritz et al., the feasibility of NIRL-based tissue sampling for spatially resolved proteomics was shown by analyzing murine intestine with an axial resolution of ~117 µm. Although distinguishable protein patterns were identified for the mucosa including the intestinal epithelium and muscularis propria, the axial resolution of ~117 µm was not necessarily sufficient to spatially resolve the proteome of intermediate cellular structures, corresponding to the muscularis mucosa and submucosa.

To further enhance the spatial resolution, several parameters in the sample processing protocol were modified in this follow-up study. When nine consecutive tissue layers from scalp into the cortex were taken by NIRL directly from embryonic mouse head, the resulting aerosol was captured on polytetrafluoroethylene (PTFE) coated glass slides. By this only a predefined area was covered during resuspension of the sample condensate. To further minimize surface adsorption effects occurring during sample processing, samples were tryptically digested using an adapted one-pot sample preparation protocol that employed the non-ionic detergent *n*-dodecyl β-D-maltoside (DDM). Consequently, the requisite tissue volume for comprehensive analysis was reduced to a volume of less than 30 nL. In terms of spatial resolution, the axial resolution was refined to approximately 40 µm. Overall, 5,031 proteins were identified including 3,126 proteins with quantitative information. Based on the top100 ANOVA significant proteins, a gradient-wise protein abundance distribution was observed across the ablated layers. Further, the identified proteins from each layer were compared to gene sets of the different morphological tissue structures of mouse head, including the skin, bone structures, meninges and cerebral cortex. A significant degree of overlap was observed between the proteins identified in the superficial layers and those present in the skin and bone structures. The bottom layers showed higher abundances of proteins associated with cortical structures. Additionally, known cortex markers like SOX2, KI67, NESTIN, and MAP2 showed a layer-specific spatial protein abundance distribution from the scalp to the ventricular zone of embryonic mouse head, which was further confirmed by IHC stainings. Moreover, potential novel marker proteins for cortical layers, such as MTA1 and NMRAL1 were proposed and validated by in situ hybridization (ISH) images. This study represents the primary investigation into the spatially resolved proteome of the cerebral cortex during embryonic development. Furthermore, it was demonstrated that NIRL-based tissue sampling can be employed to obtain samples from sensitive tissue structures, such as the meninges. This underscores the significant potential and versatility of the developed method for 3D spatial omics.

Direct 3D Sampling of the Embryonic Mouse Head: Layer-wise Nanosecond Infrared Laser (NIRL) Ablation from Scalp to Cortex for Spatially Resolved Proteomics

Jelena Navolić,[⊥] Manuela Moritz,[⊥] Hannah Voß, Simon Schlumbohm, Yannis Schumann, Hartmut Schlüter, Julia E. Neumann,^{*,⊥} and Jan Hahn^{*,⊥}



Cite This: *Anal. Chem.* 2023, 95, 17220–17227



Read Online

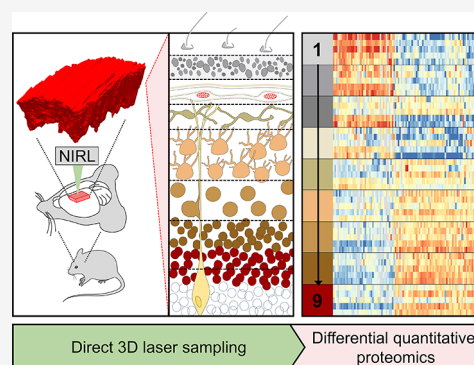
ACCESS |

Metrics & More

Article Recommendations

Supporting Information

ABSTRACT: Common workflows in bottom-up proteomics require homogenization of tissue samples to gain access to the biomolecules within the cells. The homogenized tissue samples often contain many different cell types, thereby representing an average of the natural proteome composition, and rare cell types are not sufficiently represented. To overcome this problem, small-volume sampling and spatial resolution are needed to maintain a better representation of the sample composition and their proteome signatures. Using nanosecond infrared laser ablation, the region of interest can be targeted in a three-dimensional (3D) fashion, whereby the spatial information is maintained during the simultaneous process of sampling and homogenization. In this study, we ablated 40 μm thick consecutive layers directly from the scalp through the cortex of embryonic mouse heads and analyzed them by subsequent bottom-up proteomics. Extra- and intracranial ablated layers showed distinct proteome profiles comprising expected cell-specific proteins. Additionally, known cortex markers like SOX2, KI67, NESTIN, and MAP2 showed a layer-specific spatial protein abundance distribution. We propose potential new marker proteins for cortex layers, such as MTA1 and NMRAL1. The obtained data confirm that the new 3D tissue sampling and homogenization method is well suited for investigating the spatial proteome signature of tissue samples in a layerwise manner. Characterization of the proteome composition of embryonic skin and bone structures, meninges, and cortex lamination in situ enables a better understanding of molecular mechanisms of development during embryogenesis and disease pathogenesis.



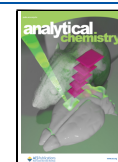
INTRODUCTION

In the past decade, there have been increasing efforts in mass spectrometry-based proteomics to analyze even smaller sample quantities down to single cells. Based on fluorescence-activated cell sorting (FACS), different cell types of a tissue sample could be analyzed with bottom-up proteomics.^{1,2} However, the spatial information and important components from the tissue microenvironment such as the extracellular matrix (ECM) are lost.³ Thus, many research groups have focused on methods for spatial proteomics. For example, different macroscopic brain regions (cerebellum, hippocampus, thalamus, striatum, olfactory bulb, prefrontal cortex) were dissected prior to subsequent bottom-up proteomics, resulting in coarse spatial resolution within the brain.^{4,5} This however does not sufficiently consider heterogeneities within the structures.³ In contrast, using Matrix-Assisted Laser Desorption and Ionization Mass Spectrometry Imaging (MALDI–MSI), it is possible to analyze different omics modalities while maintaining high spatial information.^{6–8} A laser beam scans a single tissue section in a grid-wise manner and allows a two-dimensional (2D) image of spatial protein or peptide distribution for proteomic analysis.⁹ Depending on the proximity of measured

points, the resolution can be increased to 10 μm .⁷ Furthermore, computational methods reconstruct and stack the 2D images of single tissue sections into a final 3D MSI data set to investigate multidimensional protein distribution.⁷ While MALDI–MSI is well suited for the analysis of spatial peptide distribution, a drawback of this approach is that only a small part of the tissue proteome is detected due to suppression effects.^{8,10,11} Using MALDI–MSI only, a few hundred proteins can be identified, whereas LC-MS/MS-based methods for bottom-up proteomics reveal several thousands of proteins with quantitative information.^{8,10}

Another approach used in spatial proteomics is laser-capture microdissection (LCM). This tool utilizes a pulsed laser for the dissection and isolation of a region of interest (ROI) on a

Received: June 16, 2023
Revised: October 6, 2023
Accepted: October 12, 2023
Published: November 13, 2023



tissue section in the submicrometer scale.¹² To define the ROI for tissue sectioning, staining and visualization with a light microscope is required.^{3,13} The dissected sample had to be further processed according to the bottom-up proteomics workflow. Here, one crucial step is the sample homogenization, releasing the biomolecules from the original tissue sample. During this, enzymatic or mechanical degradation can occur, resulting in alterations of the protein composition.¹⁴

A novel approach to overcome the above-mentioned limitations is the nanosecond infrared laser (NIRL) for a fast simultaneous tissue sampling and homogenization.^{15–18} The process is based on tissue irradiation with ultrashort infrared laser pulses at a wavelength of 2940 nm. During this process, the energy is absorbed and converted into vibrational motion of the OH stretch band of water molecules in the cell. This causes an explosion, wherein the biomolecules are released in a homogenized aerosol and captured for further sample processing.^{19,20} As the biomolecules remain in their native form, it offers an insight into the proteome, which is closer to the original composition in the intact tissue.^{14,21,22} Furthermore, during the ablation, only the irradiated tissue region is removed without damaging the surrounding area,²³ and thus, the method is well suited for its application in spatial proteomics. Recently, it was used to spatially resolve the layered structure of the murine intestine with a lateral resolution of 117 μm by subsequent bottom-up proteomics.¹⁶

In this study, we used NIRL-based tissue sampling to ablate directly from an intact, fresh frozen embryonic mouse head. Targeting the forebrain region, we gained even higher axial resolution with consecutive layers of 40 μm thick from the scalp to the cerebral cortex. It is known that corticogenesis is a highly orchestrated process and depends on gradients of specific markers or pathways. In the ventricular zone (VZ), the deepest layer of the cerebral cortex, radial glial cells (RGCs) proliferate and generate neurons known as direct neurogenesis. Alternatively, RGCs can give rise to intermediate progenitors (IPs) in the second germinal layer, the subventricular zone (SVZ). These IPs can further divide to generate pairs of neurons (indirect neurogenesis). Postmitotic cells leave the germinal layer and migrate radially along the RGCs to more superficial regions to form the subplate (SP), which later becomes the cortical plate (CP). Early-born projection neurons remain in deeper layers, while later-born neurons migrate in more superficial cortex layers.^{24,25} Spatially defined gradients of single factors or pathways are crucial for intact cortical layering. One well-known protein that regulates migration is Reelin, expressed by Cajal-Retzius cells in the marginal zone (MZ), the first layer of the cortex.²⁶ Mutations in the human *RELN* gene revealed impaired neuron migration leading to irregular cortex layering associated with neural migration disorders (NMD) like agyria and cortical dysplasia.^{27,28} Characterization of layer-specific signatures in development and disease is therefore crucial to unravel the pathogenesis of cortical malformations.

Comprehensive analysis of proteome composition within the embryonic mouse head structures and especially for the heterogeneity of cortical layers has not yet been performed. Our study provides a three-dimensional map of protein abundances, enabling new insights into these complex structures at a developmental stage.

EXPERIMENTAL SECTION

Animal Handling and Preparation. All animals were kept at 12 h/12 h light/dark cycle with accessible water and food supply. The animals were handled according to local government guidelines. We used four control mice (FB1–4) with a C57BL/6 background at embryonic day E14.5. The mouse head was flash-frozen in liquid nitrogen-cooled 2-methylbutane. The base of the head was mounted with Tissue-Tek O.C.T. compound onto a glass slide. To standardize the ROI, the midline and left eye were marked with red color. The ROI for ablation was then placed near the marked regions. The mounted tissue was stored at $-80\text{ }^{\circ}\text{C}$ until laser ablation.

Laser Ablation and Sample Collection. A nanosecond infrared laser (NIRL) system was used for tissue ablation. The general laser system build-up is published,¹⁶ the main experiment-specific parameters will be further described. The wavelength of the laser was set to 2940 nm using a pulse width of 7 ns, pulsing with the maximum repetition rate of 20 Hz. A pulse energy of 650 μJ was measured at the sample position. A scan lens with a focal length of 100 mm was used for focusing the beam. The glass slide with the tissue was placed on a cooling stage, which was set to $-5\text{ }^{\circ}\text{C}$ during the ablation. The cooling stage was mounted onto a translation stage composed of two motorized linear stages (MLT25, Newport Corp., CA). A PTFE-coated glass slide with 12 wells (Eprexia X5XER202-WAD1, catalog-no. 17342650) was placed at a short distance ($<1\text{ mm}$) above the ROI (800 μm \times 800 μm). Single wells were used to collect the plume material of a single layer. In total, nine layers were ablated from five hemispheres, and each layer was $2 \times 25\text{ }\mu\text{m}$ deep and consisted of 112 laser pulses.

Thickness Measurement and Optical Coherence Tomography (OCT). To estimate the number of layers to ablate, H&E-stained FFPE frontal sections of the mouse head were used. To determine the actual ablation volume, OCT measurements were performed before and after NIRL ablation of nine consecutive tissue layers. Additional information can be found in [Supporting Information](#).

Sample Processing. Further sample processing was done with the protocol published by Tsai et al.²⁹ The condensed sample aerosol was resuspended in 10 μL of 0.01% DDM (n-dodecyl β -D-maltoside) and transferred from the well into a protein low binding tube (Protein LoBind Tubes, Eppendorf SE, catalog-no. 0030108116). All other sample preparation steps were adapted from the mentioned protocol with the change to 20 ng trypsin for tryptic digestion.²⁹ The samples were dried in a vacuum centrifuge and stored at $-20\text{ }^{\circ}\text{C}$. Prior to mass spectrometric measurement, tryptic peptides were resuspended in 10 μL of 0.1% FA.

Fraction Library Preparation. Besides NIRL-based laser ablation of four different mouse heads, brain tissue was conventionally homogenized for building a fraction library to improve the search engine results in later data processing by matching between runs function. A more detailed description can be found in the [Supporting Information](#).

Mass Spectrometric Data Acquisition. Liquid chromatography–tandem mass spectrometry (LC-MS/MS) measurements were performed on a Tribrid Mass spectrometer (Orbitrap Fusion, Thermo Fisher Scientific, Waltham, MA) coupled to a nano-UPLC (Dionex Ultimate 3000 UPLC system, Thermo Fisher Scientific, Waltham, MA)

Separation and elution of peptides were achieved by a linear gradient from 2 to 30% solvent B in 30 min at a flow rate of 0.3

$\mu\text{L}/\text{min}$. Eluting peptides were ionized by using a nano-electrospray ionization source (nano-ESI) with a spray voltage of 1800 V, transferred to the MS, and analyzed in data-dependent acquisition (DDA) mode. More information in the [Supporting Information](#).

Data Processing and Analyses. Database search was performed with Proteome Discoverer (version 2.4.1.15). Spectra were searched using Sequest HT against a reviewed murine Swissprot FASTA database obtained in December 2021 containing 17,085 entries. Further data processing and analysis were done in R studio (version 4.2.3). The \log_2 -transformed data was used for the HarmonizR framework (version 0.0.0.9000)³⁰ for batch effect reduction of pseudo batches (p batch) with the ComBat method (mode 1). More information about data processing and statistical analyses including prior batch effect reduction can be found in the [Supporting Information](#).

Histological Staining. Hematoxylin-Eosin (H&E) staining was performed on acetone-fixed cryosections ($8\ \mu\text{m}$) and on formalin-fixed and paraffin-embedded (FFPE) tissue sections ($2\ \mu\text{m}$). Immunohistochemistry (IHC) with 3, 3-diaminobenzidine (DAB) was performed on FFPE sections with the Ventana Benchmark XT machine (Ventana, Tuscon). First antibodies used: MAP2C (M4403, 1:3000), NESTIN (611658, 1:200), KI67 (ab15580, 1:100), and SOX2 (ab97959, 1:200). The stained sections were scanned and digitalized with Hamamatsu Photonics K.K. and NDP.view (version 2.8.24). The in situ hybridization images (ISH) of embryonic mice at E13.5 were obtained from <http://developingmouse.brain-map.org>, accessed on 21.12.2022.³¹ The corresponding experiment IDs and sources are provided in the [Supporting Information](#). All Images were processed with Photoshop Elements 15 and Fiji (ImageJ 2.1.0)³².

RESULTS AND DISCUSSION

Laser Ablation Parameters and Quantification. In this study, we utilized NIRL-based 3D sampling and homogenization to directly ablate consecutive layers from fresh frozen embryonic mouse head for mass spectrometry-based spatial bottom-up proteomics. To estimate the required total laser ablation depth from the scalp to the ventricular zone, we used H&E-stained FFPE frontal head sections and measured the thickness from the skin surface to the ventricle margin (total thickness) at three different embryonic time points of development (Figure 1a, each time point $n = 6-9$, [Supporting Information](#)). As expected, there was no significant difference between the left (l) and right (r) hemispheres at any time point, while the mean total thickness was increasing over time, E14.5: $\bar{x} = 294.6\ \mu\text{m}$ (min = $203\ \mu\text{m}$, max = $445.7\ \mu\text{m}$), E16.5: $\bar{x} = 623.3\ \mu\text{m}$ (min = $548\ \mu\text{m}$, max = $683.9\ \mu\text{m}$), and for E18.5: $\bar{x} = 957.8\ \mu\text{m}$ (min = $613.4\ \mu\text{m}$, max = $1204\ \mu\text{m}$) (Figure 1a).

The ablation setup with the NIRL system (Figure 1b) allows automated ablation of the focused laser beam over the tissue surface in the defined ROI (Figure 1c). Based on preliminary experiments, it was known that one single laser shot removes a cylindrical tissue fraction with a diameter of about $100\ \mu\text{m}$ and a height of $25\ \mu\text{m}$ on average (Figure 1c). Due to the given ablation scope (Figure 1a–c), we decided to ablate nine consecutive layers of the E14 mouse head. Each layer is covering a theoretical ablation depth of $50\ \mu\text{m}$ ($2 \times 25\ \mu\text{m}$), estimating $450\ \mu\text{m}$ depth in total. Each ablated layer consisted of 112 laser pluses distributed over an ablation area of $800 \times 800\ \mu\text{m}$ (Figure 1c). For future studies, the ablation depth and

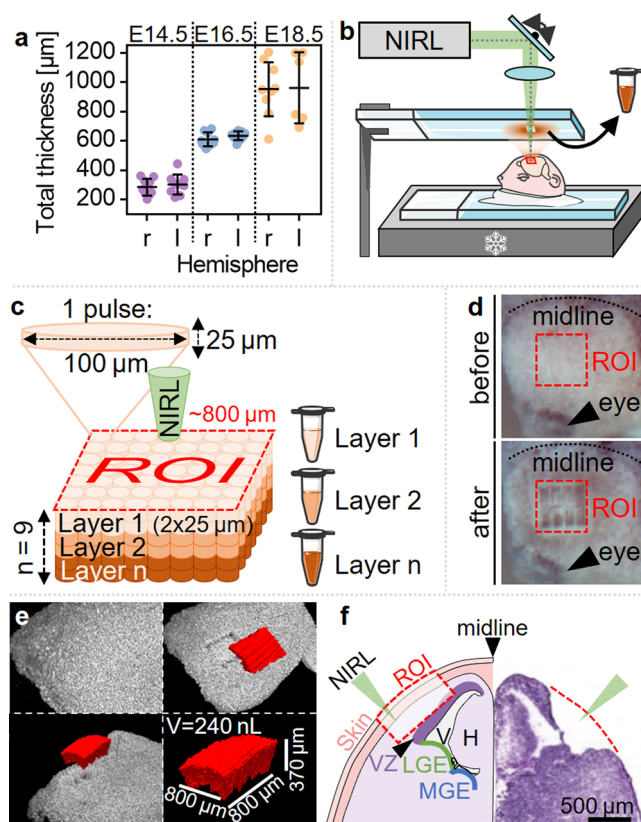


Figure 1. Experimental setting for laser ablation-based sampling and homogenization of the embryonic mouse head at E14.5. (a) Quantification of skin and mouse cortex thickness on frontal H&E-stained sections at embryonic day E14.5, E16.5, and E18.5 ($n = 6-9$). r = right; l = left ([Supporting Information](#)). Mean and SD are shown. (b) Schematic illustration of the laser ablation setup. Laser wavelength: 2940 nm; repetition rate: 20 Hz; pulse energy: $650\ \mu\text{J}$. NIRL = nanosecond infrared laser (c) The region of interest (ROI) was set to an area of $800\ \mu\text{m} \times 800\ \mu\text{m}$ and ablated by 112 laser shots per layer. Nine layers were obtained in total. (d) Pictures of the specimen. The ROI was set on the hemisphere between the midline and the eye. (e) Frontal section of the mouse head. Left: scheme. Right: H&E-staining of a frozen section after the laser ablation. H = hippocampus, V = ventricle, VZ = ventricular zone, LGE = lateral ganglionic eminence, and MGE = medial ganglionic eminence. (f) Optical coherence tomography (OCT) analysis before and after the ablation with the manually segmented ROI in red ([Supporting Information](#)). Mean values are displayed ($n = 3$).

area can be dynamically adjusted to the required resolution. Here, we aim to target the cerebral cortex, avoiding the midline region. Prior to ablation, we marked the midline and the left eye to standardize the ablation region and placed the ROI in equal proximity to the marked region (Figure 1d).

In order to determine the actual depth of the ablated volume, we scanned the surface of the specimens with optical coherence tomography (OCT) before and after the ablation. The results show that the actual average ablation depth of all nine layers in total reached about $370\ \mu\text{m}$ and a volume of $240\ \text{nL}$ ($n = 3$) (Figure 1f). The deviation from the initially estimated $50\ \mu\text{m}/\text{layer}$ to the actual coverage of $41.1\ \mu\text{m}/\text{layer}$ may occur due to decreasing laser energy over ablation depth and the sample being out of laser focus. As further refinement for the ablation system, an automated adjustment of the laser settings after each layer ablation could be implemented. To verify the ablation region and depth using histology, we

prepared fresh frozen sections of the specimen after the ablation. Respective frontal sections were stained via H&E and showed that the nine ablated layers cover most of the cortex area but were insufficient to reach the border to the ventricle (V) (Figure 1e). Overall, we covered a large part of the cortex with a high spatial resolution for further differential quantitative proteomics.

Sample Processing. The principle of NIRL-based sampling and homogenization is the cold evaporation of tissue samples, where the biomolecules are released within an aerosol. For targeted aerosol collection, we used glass slides with 12 wells predefined by PTFE coating. Each well was manually placed above the ROI on the embryonic mouse head to collect the aerosol of the single layers. Based on microscope images, we reassured that the collected aerosol is evenly distributed and well homogenized. Only a few larger chunks were observed, most likely formed during the drying process of the tissue aerosol (Supplementary Figure 1). For subsequent sample preparation, we adapted to a protocol using *n*-dodecyl β -D-maltoside (DDM) as a nonionic detergent. DDM is compatible with mass spectrometry and brings membrane proteins into solution particularly well.²⁹ After the resuspension of the condensed sample aerosol with DDM, all sample preparation steps were performed in a single low protein binding tube, thus avoiding unnecessary transfer steps that could potentially lead to adsorption effects. These effects also occur during resuspension of the sample. Using predefined wells for targeted aerosol collection, the wetted area was limited during resuspension by the hydrophobic properties of PTFE coating. This additionally minimized the loss of sample due to adsorption effects.

Altogether, we were able to reduce the ablation volume by a factor of 20, from the prior 600¹⁶ to 30 nL per layer, and still identify 3126 proteins with quantitative information. In terms of spatial resolution, this means that we effectively enhanced the *z*-resolution from 117¹⁶ to 41 μ m per layer. The potential to further increase the resolution to the laser beam dimensions (Figure 1c) depends on further sample processing improvements and measurements with highly sensitive mass spectrometers to accomplish resolutions like conventional methods for spatial proteomics such as MALDI-MSI⁷ or laser capture microdissection (LCM).^{3,12,13} Both methods MALDI-MSI and LCM contain several sample preparation steps like tissue sectioning, fixation, matrix application, and staining, risking degradation processes resulting in altered protein composition.¹⁴ In contrast, the simple application of NIRL requires neither prior tissue sectioning nor complex sample preparation. Instead, concurred homogenization allows fast sampling, ensuring that biomolecules remain close to their native form (Figure 1b). Moreover, direct 3D sampling offers more flexibility to orientate the sample and reach respective regions of interest.

Data Preprocessing and Batch Effect Reduction. In our study, we ablated five hemispheres from four mouse heads (FB1–4), the right hemisphere from FB1–3 as biological replicates, and the right and left hemispheres of FB4 as technical replicates ($n = 5$ in total). The ablation of each animal was performed on four different days, and each day was labeled as a laser ablation batch (LA batches). Altogether, 45 samples were acquired (nine layers per hemisphere and five hemispheres in total). These samples were measured in five different batches by mass spectrometry (m batches), and we identified in total 5031 proteins including 3126 proteins with

quantitative information. These batches can introduce technical bias, the so-called batch effects, which we want to investigate and reduce. Therefore, the LA batch and m batch were combined and assigned into six pseudo batches (p batches, Supplementary Table 1). To examine whether a batch effect is present within the six pseudo batches, nonlinear Iterative Partial Least Squares principal component analysis (NIPALS-PCA) was performed using relative protein abundances of 88 detected housekeeping proteins.³³ Before applying the HarmonizR framework³⁰ for batch effect reduction, scatterplot visualization of NIPALS-PCA results in strong pseudo batch effects. Whereas after batch effect reduction, no separation is apparent for the pseudo batches (Figure 2a). Additionally, based on housekeeping proteins

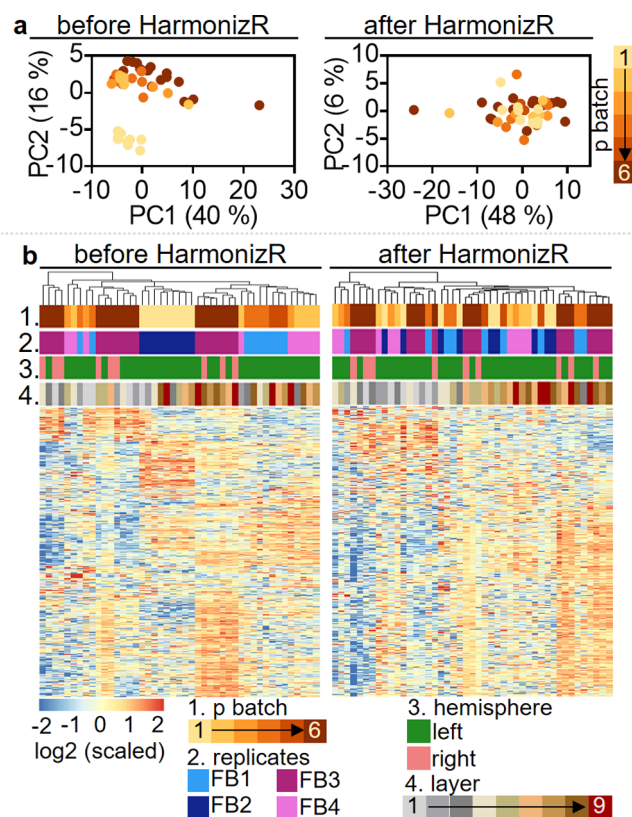


Figure 2. Batch effect reduction by integration into pseudo batches. (a) Nonlinear Iterative Partial Least Squares principal component analysis (NIPALS-PCA) based on 88 housekeeping proteins.³³ (b) Hierarchical clustering with 70% valid values before (1369 proteins) and after (1350 proteins) HarmonizR.³⁰

ACTB, GAPDH, and TUBB3, it was shown that relative protein abundances were adjusted to similar mean values across the pseudo batches after HarmonizR³⁰ (Supplementary Figure 2). For further validation of the impact of batch effects regarding the entire protein data set, hierarchical clustering was performed with 70% valid values of both data sets, before and after HarmonizR. Without batch effect reduction, the samples clustered strongly according to p batches associated with the replicates. For the harmonized data, no clustering was observed for p batches, whereas layerwise distribution was enhanced (Figure 2b). All together, we showed, by combining technical and biological replicates and reducing technical batch effects, that the laser ablation method is reproducible and applicable for analyzing layerwise signatures of the samples.

Layer Proteome Signature. After applying the Harmonizr framework³⁰ for batch effect reduction, we maintained 3040 proteins with quantitative information. We observed a higher number of detected proteins in deeper layers, suggesting a positive correlation of cell number and protein density (Supplementary Figure 3). The harmonized data (Supplementary Table 2) was used to study the proteome signature of the ablated layers. We used two different approaches for dimension reduction to analyze whether the samples can be differentiated based on the layers. First, the NIPALS-PCA allows calculations with missing values. Therefore, we used proteins with 70% valid values along the 45 samples, resulting in 1350 proteins. The scatter-plot visualization of PCA shows a gradient-wise distribution from superficial to deeper layers in the first two components, as expected (Figure 3a). This

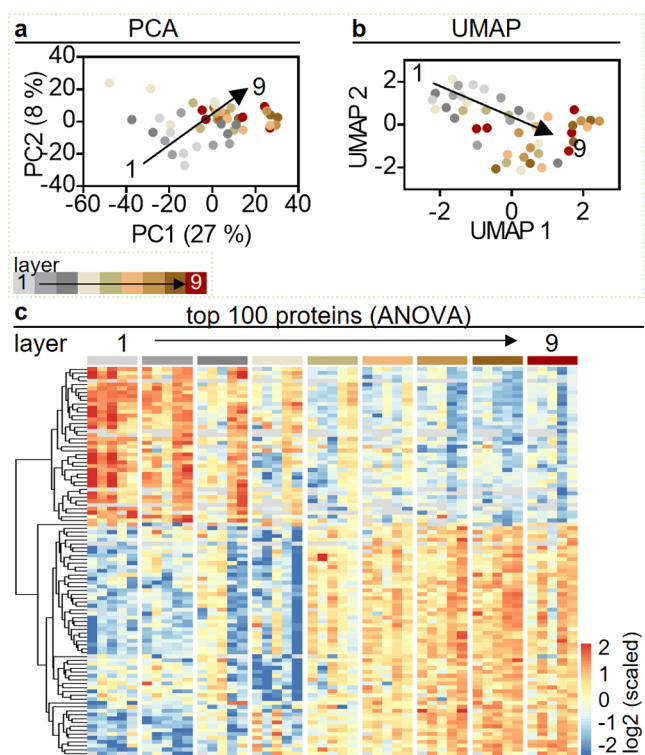


Figure 3. Dimension reduction analysis to resolve sample distribution after batch effect correction. (a) Scatter-plot visualization of the first two principal components (PC) of the NIPALS-PCA with 70% valid values (1350 proteins). (b) UMAP for dimension reduction with 100% valid values (570 proteins). Annotation color is based on layers for (a) and (b). (c) Top 100 proteins with 70% valid values were selected based on ANOVA between ablated layers ($p < 0.05$) and demonstrated in a heatmap with Euclidean distance-based hierarchical clustering.

observation can be explained by the layer composition of different cell types and factors. To confirm this observation, we additionally used UMAP (Uniform Manifold Approximation and Projection) and proteins with 100% valid values (570 proteins) and observed a similar outcome (Figure 3b).

To show which proteins drive this distribution along the layers, we selected the top 100 proteins based on ANOVA testing between the layers (70% valid values, $p < 0.05$) and visualized the abundances in a heatmap (Figure 3c, Supplementary Table 3). These results indicated distinct proteome signatures in each layer with the formation of two

superordinate protein signatures involving layers 1–4 and layers 5–9 wherein gradient-wise abundance can be observed (Figure 3c).

Next, we compared the proteins from each layer with gene sets of anatomical structures (Figure 4a, Supplementary Table 4). The mean abundance for all given proteins (Supplementary Table 5) within a gene set showed that layers 1–3 have a signature highly associated with skin and bone structures. This shows the potential to further investigate multilayered organs like the skin. Proteome analysis of the layered skin structure will improve the understanding of wound healing processes³⁴ and diverse skin conditions such as dermatitis³⁵ or psoriasis.³⁶ Layer 4 displayed a high abundance of proteins associated with the meninges (Figure 4b). Usually, during brain dissection, the two outer layers dura and arachnoidea mater are detached from the brain and impede investigating the meningeal system.³⁷ With our layer ablation method, we captured the meninges within a layer. This provides the possibility to investigate altered conditions of the blood-brain barrier in different neurological diseases.³⁸ Moreover, global proteomic analysis enables to find the potential target proteins for drug delivery and treatment of cancer and other diseases.^{34,39} Layer 5 showed a high abundance of proteins in the marginal zone. The abundance profiles of layers 6–9 corresponded with the signature from the cortical plate, including the cortical-preplate and -subplate, the subventricular zone and ventricular zone (Figure 4b). We showed that, despite the relatively simple histological composition at E14.5, we were able to show spatial differences on the proteomic level and relate the layers to anatomical structures.

To further validate our data, we compared layerwise protein abundances with immunohistochemical (IHC) staining of the E14.5 mouse cortex. We investigated proteins that are commonly used as laminar markers (Figure 4c). The brain tissue signature in layers 5–9 is supported by the high MAP2 (microtubuli associated protein)⁴⁰ protein abundance and the positive IHC staining of this dendritic marker in layers 4–9. NESTIN, a radial glia (RG) marker, showed increasing abundance toward the ventricular zone (VZ) where the somata of apical RG are located, indicating that we attained parts of the VZ.^{25,41} KI67 is an established marker for proliferating cells, which predominantly reside in the ventricular zone.⁴² Moreover, the progenitor cell marker SOX2 is also expected to be present in the VZ.^{41,43,44} Both proteins were indeed highly abundant in layer 4 and in deeper layers 8 and 9. This indicates high proliferation activity of RGs in the VZ,²⁵ a region where tumors potentially develop.²⁷ Further analysis could reveal molecular environmental factors that may facilitate tumor formation.

In order to find potential new protein markers for certain regions, we analyzed highly variant proteins among the ablated layers and compared the candidates (DLG4, APOE, NMRAL1, and MTA1) to in situ hybridization (ISH) images of mouse cortex at E13.5 (<http://www.developingmouse.brain-map.org>).³¹ We showed that both proteins, DLG4 and APOE, are associated with superficial layers on the proteomic level, which could be validated by the ISH images (Figure 4d). The protein DLG4 (Disks large homolog 4) also known as PSD95 is a postsynaptic scaffold protein regulating the excitability of glutamatergic synapses. Deficiency of this protein was shown to be related to psychiatric disorders.^{45,46} APOE (Apolipoprotein E) is a protein expressed in the brain and is associated with astrocytic cells, which are in close proximity to the pial

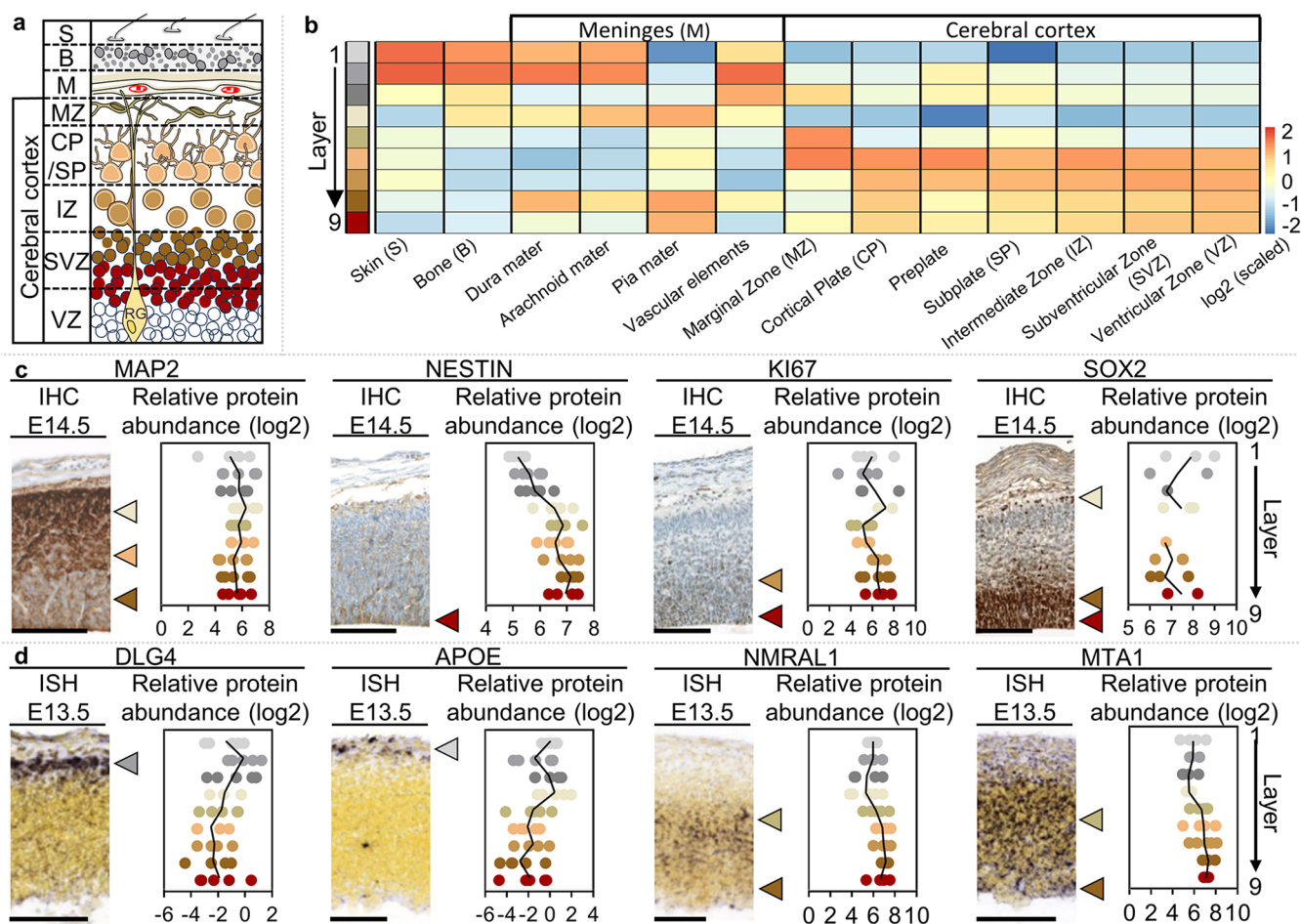


Figure 4. Analysis of layer-specific signature and marker proteins. (a) Schematic illustration of the cortex structure after the second trimester of embryonic development. RG = radial glial cells. (b) Gene set enrichment analysis of cortex structures applied to ablated layers. The layerwise calculated mean abundance of present proteins for each gene set is plotted. (c) IHC staining of mouse E14.5 cortex with known marker proteins and the corresponding protein abundance for each layer. Arrows indicate the corresponding layer with a high relative protein abundance. Scale bar: 100 μm . (d) Variant protein abundances are compared to RNA in situ hybridization (ISH) images of mouse cortex at E13.5 obtained from <http://www.developingmouse.brain-map.org>.³¹ Arrows indicate the corresponding layer with high relative protein abundance. Scale bar: 110 μm .

surface.^{47–49} NMRAL1 and MTA1 were shown to be more abundant in layers 5–9 (Figure 4d). Whereas these proteins have not been reported in the context of cortical development yet, MTA1 (Metastasis-associated protein) is known to be expressed in different cancer types and to regulate the stability of the oncosuppressor p53.^{50–52} Additionally, NMRAL1 (NmrA-like family domain-containing protein 1) is a largely unknown protein, and only a NADPH-binding function is assumed.⁵³

The results of our study confirm the potential to spatially resolve the proteomic signatures of embryonic mouse head structures and forebrain regions using NIRL-based 3D sampling and subsequent bottom-up proteomics. Direct ablation from a 3-dimensional tissue sample like the mouse head with an axial resolution of about 40 μm paves the way for numerous research questions focusing on spatial resolution in proteomics with the additional possibility to achieve even higher resolution. The high spatial resolution with 3D NIRL-based sampling for bottom-up proteomics allows future incorporation of multiomics modalities like lipidomics⁵⁴ or transcriptomics. The translation from the genomic to protein level is crucial to understand the functional and organizational complexity during development, disease pathogenesis, or

malformations and enable a better translation from disease models to the clinics.^{39,55,56}

CONCLUSIONS

In this work, we used NIRL-based 3D sampling to directly ablate consecutive tissue layers from the embryonic mouse head to the forebrain. By optimizing sample processing for subsequent quantitative, bottom-up proteomics of very small ablation volumes (<30 nL), we were able to significantly increase the spatial resolution in depth ($\sim 40 \mu\text{m}$). Further adaptation will allow to sample and analyze smaller volumes with higher spatial resolution. Our findings highlight the potential of NIRL-based sampling to spatially resolve three-dimensional tissue heterogeneities without the need for prior elaborate sample preparation steps. Thus, it is possible to specifically sample regions of interest like the scalp or meninges of the embryonic mouse head to address related research questions. Common approaches to dissociate structural layered tissue samples using proteases (e.g., dispase to separate the epidermis and dermis) will no longer be necessary.

■ ASSOCIATED CONTENT

Data Availability Statement

Data is available via ProteomeXchange with the identifier PXD043011.

SI Supporting Information

The Supporting Information is available free of charge at <https://pubs.acs.org/doi/10.1021/acs.analchem.3c02637>.

Experimental section; visualization of condensed aerosol (Figure S1); batch effect reduction by integration of pseudo batches using the HarmonizR framework (Figure S2); cell density of extracranial and cerebral cortex structures compared to the number of detected proteins with valid values per layer (Figure S3) (PDF)

Sample information and unprocessed quantitative data (Table S1) (XLSX)

Harmonized data (Table S2) (XLSX)

ANOVA significant proteins (Table S3) (XLSX)

Gene list input (Table S4) (XLSX)

Protein list (Table S5) (XLSX)

■ AUTHOR INFORMATION

Corresponding Authors

Julia E. Neumann – Research Group Molecular Pathology in Neurooncology, Center for Molecular Neurobiology (ZMNH), University Medical Center Hamburg–Eppendorf, 20251 Hamburg, Germany; Institute of Neuropathology, University Medical Center Hamburg–Eppendorf, 20251 Hamburg, Germany; orcid.org/0000-0002-1162-8771; Email: ju.neumann@uke.de

Jan Hahn – Section/Core Facility Mass Spectrometry and Proteomics, Center for Diagnostics, University Medical Center Hamburg–Eppendorf, 20251 Hamburg, Germany; orcid.org/0000-0003-3416-636X; Email: ja.hahn@uke.de

Authors

Jelena Navolić – Research Group Molecular Pathology in Neurooncology, Center for Molecular Neurobiology (ZMNH), University Medical Center Hamburg–Eppendorf, 20251 Hamburg, Germany; orcid.org/0009-0005-2112-3987

Manuela Moritz – Section/Core Facility Mass Spectrometry and Proteomics, Center for Diagnostics, University Medical Center Hamburg–Eppendorf, 20251 Hamburg, Germany; orcid.org/0000-0002-8537-7493

Hannah Voß – Section/Core Facility Mass Spectrometry and Proteomics, Center for Diagnostics, University Medical Center Hamburg–Eppendorf, 20251 Hamburg, Germany

Simon Schlumbohm – High Performance Computing, Helmut Schmidt University, 22043 Hamburg, Germany

Yannis Schumann – High Performance Computing, Helmut Schmidt University, 22043 Hamburg, Germany

Hartmut Schlüter – Section/Core Facility Mass Spectrometry and Proteomics, Center for Diagnostics, University Medical Center Hamburg–Eppendorf, 20251 Hamburg, Germany; orcid.org/0000-0002-9358-7036

Complete contact information is available at:

<https://pubs.acs.org/doi/10.1021/acs.analchem.3c02637>

Author Contributions

¹J.N. and M.M. contributed equally to this work and share the first authorship. J.E.N. and J.H. contributed equally to this

work and share senior authorship. The manuscript was written through the contributions of all authors. All authors have given approval to the final version of the manuscript.

Funding

This research was funded by the “Behörde für Wissenschaft, Forschung, Gleichstellung und Bezirke der Freien und Hansestadt Hamburg” (Public Authority for Science, Research and Equality of the Free and Hanseatic City of Hamburg; grant number LFF-FV-75 and LFF-GK-10). This study was supported by grants from the Deutsche Forschungsgemeinschaft (DFG) (INST 337/15–1, INST 337/16–1, INST 152/837–1, INST 152/947–1 FUGG, and SCHL 406/21–1). Furthermore, this work was supported by intramural funding from the faculty. J.E.N. is supported in the Emmy Noether program (DFG project number 416054672).

Notes

The authors declare no competing financial interest.

■ ACKNOWLEDGMENTS

The authors would like to thank Shweta Godbole, Matthias Dottermusch and Tasia Lempertz for their great support in working with mice, Antonia Gocke for helping perform sample preparation and Anton Walter for the support in OCT analysis. Further, the authors would like to thank the Institute of Neuropathology and Kristin Hartmann from the Mouse Pathology facility for the technical assistance and service. The authors thank Ursula Müller, Jasmin Seydler, Alexandra Gröss, Anke Dorendorf, Beate Miksche, and the other members of the animal facility team for their support and service. The authors used images and templates for parts of Figures 1 and 4 from <http://smart.servier.com>, licensed under a Creative Common Attribution 3.0 Generic License.

■ REFERENCES

- (1) Maes, E.; Cools, N.; Willems, H.; Baggerman, G. *Int. J. Mol. Sci.* **2020**, *21*, 6557.
- (2) Dyring-Andersen, B.; Løvendorf, M. B.; Coscia, F.; et al. *Nat. Commun.* **2020**, *11*, No. 5587, DOI: [10.1038/s41467-020-19383-8](https://doi.org/10.1038/s41467-020-19383-8).
- (3) Mao, Y.; Wang, X.; Huang, P.; Tian, R. *Analyst* **2021**, *146*, 3777–3798.
- (4) Sharma, K.; Schmitt, S.; Bergner, C. G.; et al. *Nat. Neurosci.* **2015**, *18*, 1819–1831.
- (5) Giansanti, P.; Samaras, P.; Bian, Y.; et al. *Nat. Methods* **2022**, *19*, 803–811.
- (6) Schwamborn, K.; Caprioli, R. M. *Mol. Oncol.* **2010**, *4*, 529–538.
- (7) Zhu, X.; Xu, T.; Peng, C.; Wu, S. *Front. Chem.* **2022**, *9*, 782432.
- (8) Ščupáková, K.; Balluff, B.; Tressler, C.; et al. *Clin. Chem. Lab. Med.* **2020**, *58*, 914–929.
- (9) Thiele, H.; Heldmann, S.; Trede, D.; et al. *Biochim. Biophys. Acta - Proteins Proteomics* **2014**, *1844*, 117–137.
- (10) Dilillo, M.; Pellegrini, D.; Ait-Belkacem, R.; et al. *J. Proteome Res.* **2017**, *16*, 2993–3001.
- (11) Lin, M.; Eberlin, L. S.; Seeley, E. H. *J. Am. Soc. Mass Spectrom.* **2022**, *33*, 296–303.
- (12) Xu, R.; Tang, J.; Deng, Q.; et al. *Anal. Chem.* **2018**, *90*, 5879–5886.
- (13) Davis, S.; Scott, C.; Ansonge, O.; Fischer, R. *J. Proteome Res.* **2019**, *18*, 1787–1795.
- (14) Kwiatkowski, M.; Wurlitzer, M.; Omid, M.; et al. *Angew. Chem. - Int. Ed.* **2015**, *54*, 285–288.
- (15) Hahn, J.; Moritz, M.; Voß, H.; et al. *Int. J. Mol. Sci.* **2021**, *22*, 10833 DOI: [10.3390/ijms221910833](https://doi.org/10.3390/ijms221910833).
- (16) Voß, H.; et al. *Int. J. Mol. Sci.* **2022**, *23*, 6132 DOI: [10.3390/ijms23116132](https://doi.org/10.3390/ijms23116132).

- (17) Dong, C.; Donnarumma, F.; Murray, K. K. *J. Am. Soc. Mass Spectrom.* **2022**, *33*, 1003–1010.
- (18) Dong, C.; Richardson, L. T.; Solouki, T.; Murray, K. K. *J. Am. Soc. Mass Spectrom.* **2022**, *33*, 463–470.
- (19) Franjic, K.; Miller, R. J. D. *Phys. Chem. Chem. Phys.* **2010**, *12*, 5225–5239.
- (20) Amini-Nik, S.; Kraemer, D.; Cowan, M. L.; et al. *PLoS One* **2010**, *5*, e13053.
- (21) Sampson, J. S.; Murray, K. K.; Muddiman, D. C. *J. Am. Soc. Mass Spectrom.* **2009**, *20*, 667–673.
- (22) Kwiatkowski, M.; Wurlitzer, M.; Krutilin, A.; et al. *J. Proteomics* **2016**, *134*, 193–202.
- (23) Böttcher, A.; Kucher, S.; Knecht, R.; et al. *Eur. Arch. Oto-Rhino-Laryngol.* **2015**, *272*, 941–948.
- (24) Nadarajah, B.; Parnavelas, J. G. *Nat. Rev. Neurosci.* **2002**, *3*, 423–432.
- (25) Florio, M.; Huttner, W. B. *Development* **2014**, *141*, 2182–2194.
- (26) Ogawa, M.; Miyata, T.; Nakajimat, K.; et al. *Neuron* **1995**, *14*, 899–912.
- (27) Copp, A. J.; Harding, B. N. *Epilepsy Res.* **1999**, *36*, 133–141.
- (28) Hevner, R. F. *J. Neuropathol. Exp. Neurol.* **2007**, *66*, 101–109.
- (29) Tsai, C. F.; Zhang, P.; Scholten, D.; et al. *Commun. Biol.* **2021**, *4*, 265.
- (30) Voß, H.; et al. *Nat. Commun.* **2022**, *13*, No. 3523.
- (31) Allen Reference Atlas – Developing Mouse Brain. <http://developingmouse.brain-map.org/>.
- (32) Schneider, C. A.; Rasband, W. S.; Eliceiri, K. W. *Nat. Methods* **2012**, *9*, 671–675.
- (33) Uhlén, M.; Fagerberg, L.; Hallström, B. M.; et al. *Science* **2015**, *347*, 1260419 DOI: 10.1126/science.1260419.
- (34) Zomer, H. D.; Trentin, A. G. *J. Dermatol. Sci.* **2018**, *90*, 3–12.
- (35) Rizzo, J. M.; Oyelakin, A.; Min, S.; et al. *Cell Death Differ.* **2016**, *23*, 1073–1085.
- (36) Schön, M. P.; Manzke, V.; Erpenbeck, L. *J. Allergy Clin. Immunol.* **2021**, *147*, 439–455.
- (37) Louveau, A.; Filiano, A. J.; Kipnis, J. *Curr. Protoc. Immunol.* **2018**, *121*, 678–687.
- (38) Munji, R. N.; Soung, A. L.; Weiner, G. A.; et al. *Nat. Neurosci.* **2019**, *22*, 1892–1902.
- (39) Ha, J.; Park, H.; Park, J.; Park, S. B. *Cell Chem. Biol.* **2021**, *28*, 394–423.
- (40) Caceres, A.; Binder, L.; Payne, M.; et al. *J. Neurosci.* **1984**, *4*, 394–410.
- (41) Penisson, M.; Ladewig, J.; Belvindrah, R.; Francis, F. *Front. Cell. Neurosci.* **2019**, *13*, 1–21.
- (42) Li, L. T.; Jiang, G.; Chen, Q.; Zheng, J. N. *Mol. Med. Rep.* **2015**, *11*, 1566–1572.
- (43) Miyagi, S.; Nishimoto, M.; Saito, T.; et al. *J. Biol. Chem.* **2006**, *281*, 13374–13381.
- (44) Amador-Arjona, A.; Cimadamore, F.; Huang, C. T.; et al. *Proc. Natl. Acad. Sci. U.S.A.* **2015**, *112*, E1936–E1945.
- (45) Keith, D.; El-Husseini, A. *Front. Mol. Neurosci.* **2008**, *1*, 200 DOI: 10.3389/neuro.02.004.2008.
- (46) Coley, A. A.; Gao, W. J. *Prog. Neuro-Psychopharmacol. Biol. Psychiatry* **2018**, *82*, 187–194.
- (47) Abnet, K.; Fawcett, J. W.; Dunnett, S. B. *Dev. Brain Res.* **1991**, *59*, 187–196.
- (48) Sun, Y.; Wu, S.; Bu, G.; et al. *J. Neurosci.* **1998**, *18*, 3261–3272.
- (49) Pfrieder, F. W. *Cell. Mol. Life Sci.* **2003**, *60*, 1158–1171.
- (50) Gururaj, A. E.; Singh, R. R.; Rayala, S. K.; et al. *Proc. Natl. Acad. Sci. U.S.A.* **2006**, *103*, 6670–6675.
- (51) Li, D. Q.; Divijendra Natha Reddy, S.; Pakala, S. B.; et al. *J. Biol. Chem.* **2009**, *284*, 34545–34552.
- (52) Liu, J.; Xu, D.; Wang, H.; et al. *Oncotarget* **2014**, *5*, 5153–5164.
- (53) Zang, W.; Zheng, X. *Free Radic. Biol. Med.* **2020**, *160*, 768–774.
- (54) Stadlhofer, R.; et al. *Int. J. Mol. Sci.* **2023**, *24*, 7820.
- (55) Pradet-Balade, B.; Boulmé, F.; Beug, H.; Müllner, E. W.; Garcia-Sanz, J. A. *Trends Biochem. Sci.* **2001**, *26*, 225–229.
- (56) Wang, T.; Cui, Y.; Jin, J.; et al. *Nucleic Acids Res.* **2013**, *41*, 4743–4754.

6 DISCUSSION

The studies published as part of this thesis provide clear evidence of the significant potential of NIRL-based tissue sampling for subsequent mass spectrometric analysis. By simplifying and improving processing workflows, these studies have made a significant contribution to the field of spatial omics. The following discussion focuses on the methodological advancements achieved in the respective studies, with particular emphasis on the intended application of the NIRL-based technique in three-dimensional spatial omics.

In the initial study published by Hahn & Moritz et al. in 2021, approximately 500 nL of tissue, corresponding to a tissue amount of 500 μg [67], was sampled from unprocessed murine spleen and colon tissues by NIRL [68]. Similar to previous studies by our group [49, 50, 57, 69], NIRL ablation was operated in reflection geometry to allow sampling and homogenization from intact tissue specimens. In contrast, Kermit Murray's group employed NIRL ablation for the sampling of tissue sections in transmission geometry. The downward-facing cryosections are irradiated by NIRL and the resulting aerosol is collected in a reaction vessel comprising buffer solution and placed in close proximity to the glass slide [70, 71]. Besides the limited application of this method to tissue sections, the aerosol captured in buffer solution not only contains the biomolecules of interest but also endogenous enzymes that remain active [60]. This may potentially result in the degradation of biomolecules, such as proteins. In the study of Hahn & Moritz et al., commercially available microscope slides were used for capturing the aerosol [68]. The glass slide was placed slightly above the tissue sample to be ablated, where the sample condensate dried immediately, thereby inhibiting enzyme activity. The samples were further processed by the developed bottom-up proteomic workflow and overall, 1,889 proteins were obtained with quantitative information. In comparison to a previous study by our group [50], where a cooling trap was used for aerosol collection, the number of proteins was in the same order of magnitude, although a 100-fold smaller tissue volume was analyzed. It was reasoned that the direct collection of the sample aerosol on microscope slides effectively circumvents the potential material loss that could otherwise result from surface adsorption on the tubing system utilized for aerosol transport. Differential quantitative proteome analysis revealed that spleen and colon tissue samples could be clearly distinguished. Given the inherent differences between the soft tissue of the spleen and the muscular tissue of the intestine, it was further tested whether the observed results were potentially attributable to disparate ablation behaviors. The comparable protein abundances of housekeeping proteins [72], representing the basic inventory of a cell, and the markedly differential abundance of tissue-specific marker proteins confirmed that both soft tissue and muscular tissue can be homogenized equally effectively using NIRL. This is consistent with the underlying DIVE principle [47, 48]. The use of short pulse mid-infrared laser ablation results in the excitation of water molecules within the tissue samples. The absorbed energy is converted into vibrational motion of the OH stretch band, leading to an explosion and decomposition of the irradiated tissue area, whereby the biomolecules are released into the gas phase. Since all biological tissues contain water [73], mid-infrared laser ablation is perfectly suited for the homogenization of the wide variety of tissue samples. In previous studies, it was even possible to ablate hard tissues like cortical bone of chicken [74] and human teeth [75]. In addition, the study by Kwiatkowski et al. (2015) demonstrated that PIRL facilitates a more effective homogenization of muscle tissue, as evidenced by the higher protein yield observed in the PIRL homogenate relative to the conventional homogenization method using mortar and pestle [49].

Even with more recent homogenization techniques like the pressure cycling technology (PCT), the homogenization of muscular tissues results in less protein yields compared to other tissues like brain, liver, lung or kidney [15, 41]. In the study of Shao et al. (2016), tissue samples of 2-4 mg were homogenized by PCT and 1,500-2,000 proteins were identified, with the lowest number of proteins found for muscle-rich heart tissue [15]. In the study of Hahn & Moritz et al., a comparable number of proteins could be identified using an 8-fold smaller amount of tissue [68]. According to this, the method developed here seems to enable more efficient homogenization and sample processing for low-input mass spectrometric proteome analysis.

In a more recent study, approximately 4,000 proteins from mouse kidneys weighing between 0.8-1.2 mg were analyzed, in which PCT-assisted homogenization and tryptic digestion was utilized [76]. Nevertheless, the processing of muscle-rich tissues, such as the intestine and stomach, by PCT remains a significant challenge. Despite the expectation of a similar protein content [73], significantly lower peptide yields were observed for intestinal and gastric tissues in comparison to other tissues, such as renal and pancreatic tissues [76]. In the study of Stadlhofer & Moritz et al., for the first time NIRL-based tissue sampling was combined with shotgun lipidomics [77]. In this study, human HPV-positive oropharyngeal squamous cell carcinoma (OPSCC) and healthy mucosa samples were analyzed. In contrast to the study by Hahn & Moritz et al. [68], an ablation chamber had to be used here. When human tissue samples are ablated, the resulting aerosol poses a potential risk of infection for the experimenter, since viruses are still active after ablation [78]. Similar to the previous study of Hänel et al. (2018), the ablation chamber was operated with a glass fiber filter for aerosol collection [69]. However, the PTFE tubing was removed to minimize potential adsorption effects and the diameter of the glass fiber filter was minimized to approximately 1 cm [77]. As in the previous proteomics study, tissue volumes of approximately 500 nL were sampled by NIRL. The lipids were extracted from the glass fiber filter in advance of subsequent shotgun lipidomics. Quantitative lipidome analysis was performed using the Lipidyzer™ Platform [79, 80]. Overall, 755 lipid species from 13 lipid classes were analyzed from OPSCC and mucosa samples. The quantitative lipid data facilitated the differentiation of OPSCC and non-tumorous mucosa samples, as also enabling the characterization of mucosa samples originating from either the tonsil or the base of the tongue (BOT) by means of different lipid profiles [77].

In a recent study by Ogrinc et al. (2022), the SpiderMass technology was employed to analyze squamous cell carcinoma (SCC) from the oral cavity by means of online MS measurements [64]. The SpiderMass technology utilizes NIRL as a tissue microsampling device combined with mass spectrometry-based real-time molecular analysis [61]. Similar to the results of Stadlhofer & Moritz et al. [77], oral tongue SCC and non-tumor regions were also discriminated by alterations in the phosphatidylcholine (PC) and phosphatidylethanolamine (PE). While the real-time molecular analysis utilized in the SpiderMass technology [61, 63, 64, 81–83] and PIRL-MS [62, 65, 66, 84, 85], a technique developed by the group of Arash Zarrine-Afsar, offers a rapid and sensitive method for diagnostic purposes, shotgun lipidomics is an analytical approach for large-scale and systematic analysis of the composition, structure, and quantity of cellular lipids. Further advancements in shotgun lipidomics have been achieved through the development of the Lipidyzer™ Platform, which utilizes direct infusion, differential mobility spectrometry (DMS) technology, and multiple reaction monitoring (MRM) on a QTRAP mass spectrometer, enabling the separation and quantification of even isobaric molecular species [79, 80, 86]. The benefits of integrating NIRL-based tissue sampling with the Lipidyzer™ Platform are underscored by the findings of Cao et al. (2020). In comparison to the study of Stadlhofer & Moritz et al., a 50-fold larger tissue amount (~25 mg) was used and only a comparable number of 787 lipid species from heart and liver tissue were quantified with the Lipidyzer™ platform [80]. Moreover, it was observed that the NIRL-based methodology appears to have a markedly beneficial impact on the coverage of the lipidome, particularly in the processing of low-input amounts. In the study performed by Stadlhofer & Moritz et al., 755 lipid species were quantified [77]. In contrast, the study by Odenkirk et al. (2022) yielded only 248 lipids from a micropunch of lipid-rich brain with a similar tissue amount of 500 µg [11]. Höring et al. (2021) tested the influence of different homogenization techniques and solvents using quantitative lipidome analysis of murine liver [38]. It was found that lipid recovery can be strongly influenced not only by the homogenization efficiency but also by the solvent composition used. These findings underline the advancements of the NIRL-based methodologies for mass spectrometric omics. Here, no solvent is required for cell lysis as all the biomolecules independently of their physico-chemical properties are released from their cellular compartments in a soft and cold vaporization process. In conventional techniques, sodium dodecyl sulfate (SDS) is added to the solvent to minimize enzymatic degradation and further enhance the sample stability [38]. In contrast, using NIRL-based sampling the samples are taken quickly and the aerosol is collected either on the glass slide or the glass fiber filter

and dried immediately, so that the exposure to enzymatic degradation is minimized as much as possible, thereby enabling for a closer view in the *in vivo* composition of biomolecules compared to conventional techniques. This is also demonstrated by the findings of Kwiatkowski et al. (2016), where significantly more intact protein species were analyzed for the PIRL homogenate of human tonsil when compared to the samples homogenized by cryo-grinding, where much more proteolytic species were found [50]. Based on the findings achieved in the studies of Hahn & Moritz et al. [68] and Stadlhofer & Moritz et al. [77], it was determined that 500 nL scaled tissue volumes were sufficient input material for mass spectrometry-based bottom-up proteomics and shotgun lipidomics with high coverage. These results formed the basis for further development in the direction of 3D spatial omics as tissue voxels of the same size were applied for the region and cell layer resolved proteome analysis of murine intestine. Tissue layer of ~117 μm from three different colon parts (ascending, transverse, descending) as well as eight consecutive layers from murine intestine were sampled by NIRL and subsequently analyzed by bottom-up proteomics. With regard to the previous study of Hahn & Moritz et al. (2021), it was determined that the condensed sample aerosol is lost in the scanning area of the laser beam as the laser beam must pass through this specific region during the sampling process [68]. Therefore, the scanning area was reduced by ablating smaller areas, and instead moving the samples stepwise to cover the entire region of interest. Additionally, a scan lens and synchronized laser triggering were introduced to the setup to increase the precision of the laser ablation. In fact, this increased the number of proteins identified by bottom-up proteomics from approximately 1,600 [68] to 3,000 proteins when a comparable tissue volume (~600 nL) of murine colon was ablated [87]. In the proteomic data, distinguishable protein patterns were found for the ascending, transverse and descending colon parts. These differences mainly belong to proteins which are associated with different metabolic processes and antioxidant activity [87]. While the overall function and architecture of the large intestine was long considered to be similar, it is now known that, among other things, metabolic processes gradually change along the length of colon, emphasizing the molecular dynamics in this organ [88]. This becomes even more apparent by the favored development of colonic diseases like ulcerative colitis [89] and colorectal cancer [90] in the distal part of colon [88]. Furthermore, it is assumed that the development of tumors in the proximal and distal colon underlies different molecular pathways in colorectal cancer [90]. However, far less is known about the global proximal–distal variation in protein levels [88]. One reason for that might be that there is no appropriate method for a spatially resolved omics analysis of the intestine. Van der Post et al. (2014) tried to spatially resolve the membrane proteome of human colon by analyzing isolated epithelial cells from millimeter-sized human biopsies of four different colon parts (ascending, transverse, descending, and sigmoid) [88]. The epithelial cells were detached from the biopsies through a chemical treatment with DTT and EDTA, and subsequently separated by centrifugation. While this method limited the spatial resolution of the analysis to the selected size of the sections, the detachment of epithelial cells results in the partial loss of the tissue microenvironment [18]. The tissue microenvironment, including the extracellular matrix (ECM), is crucial for a comprehensive understanding of biological processes and spatial organization in tissues [18, 91, 92]. Since every cell is influenced by its surroundings and responds to biochemical and mechanical signals provided by the tissue microenvironment [91], it is controversially seen how well the cell state is represented in isolated cells [18]. In contrast, in the study of Voß & Moritz et al. (2022) spatially resolved proteome analysis of intestinal epithelium was performed by taking a whole tissue layer with a thickness of ~117 μm from the ascending, transverse and descending colon parts using NIRL [87]. In comparison to the aforementioned study, the tissue microenvironment including the ECM was preserved. The importance of preserving the ECM for global analysis is underscored by the results of the performed enrichment analysis of top100 ANOVA significant proteins between the three different colon parts. Among other things, significant differences for the extracellular exosome were found [87]. In future studies, NIRL-based tissue sampling could be easily applied for the gradient-wise sampling of the intestinal epithelium along the proximal-distal axis as it can rather be assumed that the abundance of the corresponding proteins gradually changes along the intestine [93, 94]. Thus, the novel NIRL-based methodology could provide spatial resolution in future proteomics

studies of intestine, allowing a better understanding of the variation of biological processes along the intestine, such as in the progression of ulcerative colitis from the distal to the proximal colon [88, 89]. Beside the proximal-distal alterations, the colon architecture is composed of tissue layers showing distinct anatomical structures and functionalities [95]. Based on the layer-by-layer sampling, cell layer resolved proteome analysis of murine intestine was achieved with an axial resolution of 117 μm , for the first time. In the recently published protocol of Jørgensen et al. (2021), the mucosa and submucosa were separated by using scissors, forceps and chemical treatment with EDTA [22]. While such protocols often require extensive practice before tissue processing could be repeated consistently [22], NIRL-based 3D tissue sampling could be easily applied to sample successive tissue layers from intact murine intestine [87]. In the differential quantitative bottom-up proteome analysis, the eight consecutively sampled tissue layers were distinguished into four cellular clusters with different protein patterns. Based on the proteomic signature, the first two layer (cluster 1) could be clearly assigned to the mucosa including the intestinal epithelium and the last three layers (cluster 4) were found to originate from the muscularis propria [87]. As already shown by the results of Hahn & Moritz et al. (2021), NIRL-based 3D tissue sampling allows tissue volumes to be removed and homogenized independently of the tissue type, e.g. soft or fibrous. Based on the results obtained by Voß & Moritz et al. (2022) this advantage can be emphasized once again, particularly with regard to spatially resolved proteome analysis. Not only the proteome of the soft mucosal layer but also that of the muscle-rich muscularis propria could be spatially resolved. Accordingly, NIRL-based 3D tissue sampling in combination with subsequent mass spectrometric analysis can be used as an unbiased method for spatial omics where the overall feasibility is given for the variety of tissue types. However, the axial resolution of $\sim 117 \mu\text{m}$ seemed to be not sufficient to spatially resolve the proteome of the intermediate layers corresponding to the muscularis mucosa and submucosa as they could not be clearly assigned to the ablated samples. This is also consistent with the tissue architecture of the intestine, which shows that the muscularis mucosa and submucosa are much thinner than the mucosa and muscularis propria, respectively [87]. To enhance the spatial resolution, parameters in the sample processing were optimized to enable the proteome analysis of even smaller ablation volumes. Since the sodium deoxycholate (SDC)-based protocol used for tryptic digestion in the previous studies [68, 87] is not specifically designed for the processing of low-input amounts, it was revised to an adapted one-pot sample preparation protocol using *n*-dodecyl β -D-maltoside (DDM) [96, 97]. Thereby sample transfer steps during sample processing were minimized and occurring analyte losses mainly avoided. In addition, to further minimize adsorption effects the microscope slides for capturing the aerosol were replaced by PTFE coated glass slides to keep the wetted area to a minimum when resuspending the sample condensate [97]. As a result, in the follow-up study by Navolić & Moritz et al. spatially resolved proteome analysis of the embryonic mouse head was performed with an axial resolution of $\sim 40 \mu\text{m}$ [97]. Despite the 20-fold reduction of ablated tissue volumes from 600 nL [87] to 30 nL [97], overall 5,031 proteins were identified including 3,126 proteins with quantitative information. Since previous work confirmed that mid-infrared laser ablation is suitable for distinct tissue types [68, 74], direct sampling from the intact mouse head was performed, whereby nine consecutive layers including the scalp to the cerebral cortex were ablated by NIRL. Based on the proteomic data, not only skin and bone structures could be assigned, but also specific marker proteins for the meninges were identified [97]. In common methods, the meninges are isolated when the brain is dissected using a scalpel [98]. However, when opening the skull, the two outer layers dura and arachnoid mater are often separated from the brain and lost for analysis [98]. Since the meninges not only have a protective function for the brain [99], but also play an important role in neurological processes and, above all, in the immune response [100] crucial information are lost when conventional techniques are used for the isolation of meninges. In contrast, the direct application of NIRL-based tissue sampling and homogenization on intact tissue specimens not only simplifies sample processing, as no prior sample preparation is necessary, but also ensures that no layer gets lost for subsequent analysis. This makes it an ideal method for studying meninges. In the study of Santorella et al. (2023) it was found that the proteome of the meninges changes along the central nervous system (CNS) axis [101]. Accordingly, the novel NIRL-based sampling technique may also be

useful to study gradual changes in meninges proteome by spatially resolved analysis. In previous spatial omics studies, the spatial resolution was often defined and partially limited by the underlying tissue structure, for example, by distinct cellular layers [22, 24, 102] or different anatomical regions [19, 21]. As already seen in the study of Voß & Moritz et al. (2022), NIRL-based sampling provides a high resolution in both lateral and axial resolution in the sampling process and the proteome of complex tissue structures can be spatially resolved by a defined resolution independently of the actual tissue architecture [87]. In the study of Navolić & Moritz et al. (2023), for the first time, spatially resolved proteome analysis of cerebral cortex during embryonic development was achieved [97]. To date, no study has performed a comprehensive analysis of the proteome composition within the cerebral cortex at development stage. In the study by MacDonald et al. (2019) laser capture microdissection (LCM) was used to examine individual layers from the cerebral cortex [103]. However, the development of cerebral cortex, also known as corticogenesis, highly depends on gradients of specific markers or pathways [104–106]. Therefore, it is particularly important to analyze not only individual layers but rather characterize layer-specific and almost gradient-wise signatures during development and disease to unravel the pathogenesis of cortical malformations [97]. Although it would be possible to perform spatially resolved proteome analysis with three-dimensional resolution applying LCM, it is rarely performed due to the enormous time and cost factor [33]. In contrast, the universally applicable methodology developed in this work enables for a fast and gentle sampling and homogenization of fresh-frozen unprocessed tissue samples, in which biomolecules can be analyzed more closely to their *in vivo* composition. Furthermore, the three-dimensional tissue structure is considered during sampling and both the lateral and axial spatial information is retained for further analysis making the application for 3D spatial omics accessible. While the previous studies by Voß & Moritz et al. [87] and Navolić & Moritz et al. [97] focused on spatially resolved proteome analysis, spatially resolved lipidome analysis will also be pursued in the future since the spatial distribution of lipids within a tissue offers novel insights into mechanisms of the synthesis, accumulation and regulation of lipids in physiological and pathophysiological condition [107]. Accordingly, potential new therapeutical targets could be proposed in future studies [108]. In addition, NIRL-based 3D tissue sampling gives access to a variety of omics and may be also utilized for future incorporation in spatial multiomics studies.

7 CONCLUSION AND OUTLOOK

In conclusion, NIRL-based 3D tissue sampling was successfully combined with low-input bottom-up proteomics and shotgun lipidomics when miniaturized tissue volumes in the size of ~500 nL were applied, thereby demonstrating the feasibility of this approach. This significant advancement was not only crucial for the further application in spatial omics but also of substantial benefit for clinical research, as the sample amount of patient biopsies is often limited. It was further demonstrated that NIRL-based sampling can be employed to obtain successive tissue layers with a defined layer thickness, irrespective of the tissue architecture present. This approach enables the standardization of tissue sampling, thereby facilitating the acquisition of more consistent and reproducible results. This allows a gradual distribution of biomolecules to be analyzed, which is associated with the actual spatial information in the tissue. Furthermore, when used in conjunction with mass spectrometric analysis, this approach offers an unbiased insight into the molecular composition of a tissue. The overall conclusion is that the methodological evolution of NIRL-based spatial tissue sampling in conjunction with optimized sample processing of low input amounts for mass spectrometric analysis can be successfully applied for 3D spatial omics.

The prospective incorporation of image guidance will allow for cross-validation and, moreover, for the targeted sampling of specific tissue structures, such as the meninges. In previous studies, the sampled tissue layers were only subsequently assigned to the corresponding physiological tissue structures based on their proteomic signature [87, 97]. However, for the future implementation of image-guidance, some requirements must be fulfilled. Most importantly, imaging must consider the three-dimensional morphology of the tissue samples, which necessitates reflection-mode visualization. In addition, the visualization should be based on a label-free approach with no need for exogenous contrast agents. It would therefore be of interest to implement optical coherence tomography (OCT) and advanced microscopy techniques such as photoacoustic remote sensing microscopy (PARS). In the previous study of Schluter et al. (2019), OCT was utilized for imaging during PIRL ablation [109]. In the studies performed in this, OCT measurements were used to determine the actual ablation volumes [68, 77, 87, 97]. The combination of OCT and PARS has been shown to provide a comprehensive view of biological samples by imaging the complementary contrasts of endogenous optical scattering and optical absorption, respectively [110, 111]. In addition, the lateral resolution and signal intensity of microscopy techniques highly rely on focusing of the objective lens. If the surface is not completely flat and the depth variations exceed the depth of focus of the objective lens, the quality of resolution is decreased [110]. However, in the previously performed studies of Hosseinaee et al. [112] and Ecclestone et al. [111], OCT was utilized to create a surface profile, thereby enabling the subsequent performance of a high-resolution PARS measurement under dynamic focusing. The multimodal imaging approach, which combines OCT and PARS, offers a distinct advantage in that it enables direct analysis of the tissue sample without the necessity of creating a smooth surface. The merged, co-registered data from PARS and OCT provide a three-dimensional visualization with sub-micron depth-resolved nuclear imaging and micron-scale depth-resolved tissue morphology [111]. Therefore, this multimodal imaging technique appears to be optimally suited for future integration with image guidance in NIRL-based 3D tissue sampling.

8 REFERENCES

- [1] Vailati-Riboni, M., Palombo, V., Loor, J. J., in: *Periparturient Diseases of Dairy Cows: A Systems Biology Approach*, Springer International Publishing, Cham 2017, pp. 1–7.
- [2] Bressan, D., Battistoni, G., Hannon, G. J., The dawn of spatial omics. *Science* 2023, 381, eabq4964. doi:10.1126/science.abq4964.
- [3] Palla, G., Fischer, D. S., Regev, A., Theis, F. J., Spatial components of molecular tissue biology. *Nat Biotechnol* 2022, 40, 308–318. doi:10.1038/s41587-021-01182-1.
- [4] Jones, A., Cai, D., Li, D., Engelhardt, B. E., Optimizing the design of spatial genomic studies. *Nat Commun* 2024, 15, 4987. doi:10.1038/s41467-024-49174-4.
- [5] Marx, V., Method of the Year: spatially resolved transcriptomics. *Nat Methods* 2021, 18, 9–14. doi:10.1038/s41592-020-01033-y.
- [6] Cheng, M., Jiang, Y., Xu, J., Mentis, A.-F. A. et al., Spatially resolved transcriptomics: a comprehensive review of their technological advances, applications, and challenges. *Journal of Genetics and Genomics* 2023, 50, 625–640. doi:10.1016/j.jgg.2023.03.011.
- [7] Tumanov, S., Kamphorst, J. J., Recent advances in expanding the coverage of the lipidome. *Current Opinion in Biotechnology* 2017, 43, 127–133. doi:10.1016/j.copbio.2016.11.008.
- [8] Labib, M., Kelley, S. O., Single-cell analysis targeting the proteome. *Nature reviews. Chemistry* 2020, 4, 143–158. doi:10.1038/s41570-020-0162-7.
- [9] Dai, X., Shen, L., Advances and Trends in Omics Technology Development. *Front. Med.* 2022, 9, 911861. doi:10.3389/fmed.2022.911861.
- [10] Varga-Zsíros, V., Migh, E., Marton, A., Kóta, Z. et al., Development of a Laser Microdissection-Coupled Quantitative Shotgun Lipidomic Method to Uncover Spatial Heterogeneity. *Cells* 2023, 12, 428. doi:10.3390/cells12030428.
- [11] Odenkirk, M. T., Horman, B. M., Dodds, J. N., Patisaul, H. B., Baker, E. S., Combining Micropunch Histology and Multidimensional Lipidomic Measurements for In-Depth Tissue Mapping. *ACS Measurement Science Au* 2022, 2, 67–75. doi:10.1021/acsmeasuresciau.1c00035.
- [12] Makhmut, A., Di Qin, Fritzsche, S., Nimo, J. et al., A framework for ultra-low-input spatial tissue proteomics. *cels* 2023, 14, 1002-1014.e5. doi:10.1016/j.cels.2023.10.003.
- [13] Kelly, R. T., Single-cell Proteomics: Progress and Prospects. *Molecular & cellular proteomics : MCP* 2020, 19, 1739–1748. doi:10.1074/mcp.R120.002234.
- [14] Gerhardtova, I., Jankech, T., Majerova, P., Piestansky, J. et al., Recent Analytical Methodologies in Lipid Analysis. *International journal of molecular sciences* 2024, 25, 2249. doi:10.3390/ijms25042249.
- [15] Shao, S., Guo, T., Gross, V., Lazarev, A. et al., Reproducible Tissue Homogenization and Protein Extraction for Quantitative Proteomics Using MicroPestle-Assisted Pressure-Cycling Technology. *Journal of proteome research* 2016, 15, 1821–1829. doi:10.1021/acs.jproteome.5b01136.
- [16] Ericsson, C., Peredo, I., Nistér, M., Optimized protein extraction from cryopreserved brain tissue samples. *Acta Oncologica* 2007, 46, 10–20. doi:10.1080/02841860600847061.
- [17] Züllig, T., Trötz Müller, M., Köfeler, H. C., Lipidomics from sample preparation to data analysis: a primer. *Anal Bioanal Chem* 2020, 412, 2191–2209. doi:10.1007/s00216-019-02241-y.
- [18] Mao, Y., Wang, X., Huang, P., Tian, R., Spatial proteomics for understanding the tissue microenvironment. *The Analyst* 2021, 146, 3777–3798. doi:10.1039/d1an00472g.
- [19] Sharma, K., Schmitt, S., Bergner, C. G., Tyanova, S. et al., Cell type- and brain region-resolved mouse brain proteome. *Nature neuroscience* 2015, 18, 1819–1831. doi:10.1038/nn.4160.

- [20] Fitzner, D., Bader, J. M., Penkert, H., Bergner, C. G. et al., Cell-Type- and Brain-Region-Resolved Mouse Brain Lipidome. *Cell Reports* 2020, 32, 108132. doi:10.1016/j.celrep.2020.108132.
- [21] Doll, S., Dreßen, M., Geyer, P. E., Itzhak, D. N. et al., Region and cell-type resolved quantitative proteomic map of the human heart. *Nature Communications* 2017, 8, 1469. doi:10.1038/s41467-017-01747-2.
- [22] Jørgensen, P. B., Fenton, T. M., Mörbe, U. M., Riis, L. B. et al., Identification, isolation and analysis of human gut-associated lymphoid tissues. *Nat Protoc* 2021, 16, 2051–2067. doi:10.1038/s41596-020-00482-1.
- [23] Cichoń, M. A., Elbe-Bürger, A., Epidermal/Dermal Separation Techniques and Analysis of Cell Populations in Human Skin Sheets. *The Journal of investigative dermatology* 2023, 143, 11-17.e8. doi:10.1016/j.jid.2022.10.012.
- [24] Dyring-Andersen, B., Løvendorf, M. B., Coscia, F., Santos, A. et al., Spatially and cell-type resolved quantitative proteomic atlas of healthy human skin. *Nature Communications* 2020, 11, 5587. doi:10.1038/s41467-020-19383-8.
- [25] Mahalingam, M., Laser Capture Microdissection: Insights into Methods and Applications. *Methods in molecular biology (Clifton, N.J.)* 2018, 1723, 1–17. doi:10.1007/978-1-4939-7558-7_1.
- [26] Espina, V., Wulfkühle, J. D., Calvert, V. S., VanMeter, A. et al., Laser-capture microdissection. *Nature protocols* 2006, 1, 586–603. doi:10.1038/nprot.2006.85.
- [27] Bonner, R. F., Emmert-Buck, M., Cole, K., Pohida, T. et al., Laser capture microdissection: molecular analysis of tissue. *Science (New York, N.Y.)* 1997, 278, 1481,1483. doi:10.1126/science.278.5342.1481.
- [28] Ahram, M., Flaig, M. J., Gillespie, J. W., Duray, P. H. et al., Evaluation of ethanol-fixed, paraffin-embedded tissues for proteomic applications. *Proteomics* 2003, 3, 413–421. doi:10.1002/pmic.200390056.
- [29] Chung, S. H., Shen, W., Laser capture microdissection: from its principle to applications in research on neurodegeneration. *Neural Regeneration Research* 2015, 10, 897–898. doi:10.4103/1673-5374.158346.
- [30] Esposito, G., in: Mocellin, S. (Ed.), *Microarray technology and cancer gene profiling*, Springer Science+Business Media, LLC; Landes Bioscience/Eurekah.com, New York, N.Y., Austin, Tex. 2007, pp. 54–65.
- [31] Sánchez-Porras, D., Bermejo-Casares, F., Carmona, R., Weiss, T. et al., Tissue Fixation and Processing for the Histological Identification of Lipids. *Methods in molecular biology (Clifton, N.J.)* 2023, 2566, 175–186. doi:10.1007/978-1-0716-2675-7_14.
- [32] Liotta, L. A., Pappalardo, P. A., Carpino, A., Haymond, A. et al., Laser Capture Proteomics: spatial tissue molecular profiling from the bench to personalized medicine. *Expert review of proteomics* 2021, 18, 845–861. doi:10.1080/14789450.2021.1984886.
- [33] Hunt, A. L., Bateman, N. W., Barakat, W., Makohon-Moore, S. et al., Extensive three-dimensional intratumor proteomic heterogeneity revealed by multiregion sampling in high-grade serous ovarian tumor specimens. *iScience* 2021, 24, 102757. doi:10.1016/j.isci.2021.102757.
- [34] Duong, V.-A., Lee, H., Bottom-Up Proteomics: Advancements in Sample Preparation. *International journal of molecular sciences* 2023, 24. doi:10.3390/ijms24065350.
- [35] Cañas, B., Piñeiro, C., Calvo, E., López-Ferrer, D., Gallardo, J. M., Trends in sample preparation for classical and second generation proteomics. *Journal of Chromatography A* 2007, 1153, 235–258. doi:10.1016/j.chroma.2007.01.045.
- [36] Prieto, D. A., Blonder, J., in: Issaq, H. J. (Ed.), *Proteomic and Metabolomic Approaches to Biomarker Discovery*, Academic Press 2020, pp. 39–52.
- [37] Ericsson, C., Nistér, M., Protein extraction from solid tissue. *Methods in molecular biology (Clifton, N.J.)* 2011, 675, 307–312. doi:10.1007/978-1-59745-423-0_17.

- [38] Höring, M., Krautbauer, S., Hittl, L., Babl, V. et al., Accurate Lipid Quantification of Tissue Homogenates Requires Suitable Sample Concentration, Solvent Composition, and Homogenization Procedure-A Case Study in Murine Liver. *Metabolites* 2021, 11. doi:10.3390/metabo11060365.
- [39] Carrasco, M., Mirzaei, H. (Eds.), *Modern Proteomics - Sample Preparation, Analysis and Practical Applications*, Springer International Publishing; Imprint: Springer, Cham 2016.
- [40] Smejkal, G. B., Robinson, M. H., Lawrence, N. P., Tao, F. et al., Increased protein yields from *Escherichia coli* using pressure-cycling technology. *Journal of biomolecular techniques : JBT* 2006, 17, 173–175.
- [41] Lucas, N., Robinson, A. B., Marcker Espersen, M., Mahboob, S. et al., Accelerated Barocycler Lysis and Extraction Sample Preparation for Clinical Proteomics by Mass Spectrometry. *Journal of proteome research* 2019, 18, 399–405. doi:10.1021/acs.jproteome.8b00684.
- [42] Kang, J., David, L., Li, Y., Cang, J., Chen, S., Three-in-One Simultaneous Extraction of Proteins, Metabolites and Lipids for Multi-Omics. *Frontiers in genetics* 2021, 12, 635971. doi:10.3389/fgene.2021.635971.
- [43] Teo, C. C., Chong, W. P. K., Tan, E., Basri, N. B. et al., Advances in sample preparation and analytical techniques for lipidomics study of clinical samples. *TrAC Trends in Analytical Chemistry* 2015, 66, 1–18. doi:10.1016/j.trac.2014.10.010.
- [44] Poluri, K. M., Gulati, K., Sarkar, S., in: Poluri, K. M., Gulati, K., Sarkar, S. (Eds.), *Protein-Protein Interactions*, Springer Singapore, Singapore 2021, pp. 1–60.
- [45] Vogel, A., Venugopalan, V., in: *Optical-Thermal Response of Laser-Irradiated Tissue*, Springer Netherlands, Dordrecht 2011, pp. 551–615.
- [46] Cowan, M. L., Bruner, B. D., Huse, N., Dwyer, J. R. et al., Ultrafast memory loss and energy redistribution in the hydrogen bond network of liquid H₂O. *Nature* 2005, 434, 199–202. doi:10.1038/nature03383.
- [47] Franjic, K., Cowan, M. L., Kraemer, D., Miller, R. J. D., Laser selective cutting of biological tissues by impulsive heat deposition through ultrafast vibrational excitations. *Optics Express* 2009, 17, 22937–22959. doi:10.1364/OE.17.022937.
- [48] Franjic, K., Miller, D., Vibrationally excited ultrafast thermodynamic phase transitions at the water/air interface. *Physical Chemistry Chemical Physics* 2010, 12, 5225–5239. doi:10.1039/c000359j.
- [49] Kwiatkowski, M., Wurlitzer, M., Omid, M., Ren, L. et al., Ultrafast extraction of proteins from tissues using desorption by impulsive vibrational excitation. *Angewandte Chemie (International ed. in English)* 2015, 54, 285–288. doi:10.1002/anie.201407669.
- [50] Kwiatkowski, M., Wurlitzer, M., Krutilin, A., Kiani, P. et al., Homogenization of tissues via picosecond-infrared laser (PIRL) ablation: Giving a closer view on the in-vivo composition of protein species as compared to mechanical homogenization. *Journal of proteomics* 2016, 134, 193–202. doi:10.1016/j.jprot.2015.12.029.
- [51] Hess, M., Hildebrandt, M. D., Müller, F., Kruber, S. et al., Picosecond infrared laser (PIRL): an ideal phonomicrosurgical laser? *European Archives of Oto-Rhino-Laryngology* 2013, 270, 2927–2937. doi:10.1007/s00405-013-2561-6.
- [52] Böttcher, A., Kucher, S., Knecht, R., Jowett, N. et al., Reduction of thermocoagulative injury via use of a picosecond infrared laser (PIRL) in laryngeal tissues. *European Archives of Oto-Rhino-Laryngology* 2015, 272, 941–948. doi:10.1007/s00405-015-3501-4.
- [53] Amini-Nik, S., Kraemer, D., Cowan, M. L., Gunaratne, K. et al., Ultrafast mid-IR laser scalpel: protein signals of the fundamental limits to minimally invasive surgery. *PLoS ONE* 2010, 5, e13053. doi:10.1371/journal.pone.0013053.
- [54] Jowett, N., Wöllmer, W., Mlynarek, A. M., Wiseman, P. et al., Heat generation during ablation of porcine skin with erbium:YAG laser vs a novel picosecond infrared laser. *JAMA otolaryngology-- head & neck surgery* 2013, 139, 828–833. doi:10.1001/jamaoto.2013.3974.

- [55] Niemz, M. H., *Laser-Tissue Interactions*, Springer International Publishing, Cham 2019.
- [56] Vogel, A., Venugopalan, V., Mechanisms of pulsed laser ablation of biological tissues. *Chem. Rev.* 2003, *103*, 577–644. doi:10.1021/cr010379n.
- [57] Krutilin, A., Maier, S., Schuster, R., Kruber, S. et al., Sampling of Tissues with Laser Ablation for Proteomics: Comparison of Picosecond Infrared Laser and Microsecond Infrared Laser. *Journal of proteome research* 2019, *18*, 1451–1457. doi:10.1021/acs.jproteome.9b00009.
- [58] Wang, K., Donnarumma, F., Herke, S. W., Herke, P. F., Murray, K. K., Infrared laser ablation sample transfer of tissue DNA for genomic analysis. *Analytical and bioanalytical chemistry* 2017, *409*, 4119–4126. doi:10.1007/s00216-017-0373-z.
- [59] Wang, K., Donnarumma, F., Herke, S. W., Dong, C. et al., RNA sampling from tissue sections using infrared laser ablation. *Analytica chimica acta* 2019, *1063*, 91–98. doi:10.1016/j.aca.2019.02.054.
- [60] Wang, K., Donnarumma, F., Baldone, M. D., Murray, K. K., Infrared laser ablation and capture of enzymes with conserved activity. *Analytica chimica acta* 2018, *1027*, 41–46. doi:10.1016/j.aca.2018.04.058.
- [61] Fatou, B., Saudemont, P., Leblanc, E., Vinatier, D. et al., In vivo Real-Time Mass Spectrometry for Guided Surgery Application. *Scientific reports* 2016, *6*, 25919. doi:10.1038/srep25919.
- [62] Woolman, M., Gribble, A., Bluemke, E., Zou, J. et al., Optimized Mass Spectrometry Analysis Workflow with Polarimetric Guidance for ex vivo and in situ Sampling of Biological Tissues. *Scientific reports* 2017, *7*, 468. doi:10.1038/s41598-017-00272-y.
- [63] Ogrinc, N., Saudemont, P., Balog, J., Robin, Y.-M. et al., Water-assisted laser desorption/ionization mass spectrometry for minimally invasive in vivo and real-time surface analysis using SpiderMass. *Nature protocols* 2019, *14*, 3162–3182. doi:10.1038/s41596-019-0217-8.
- [64] Ogrinc, N., Attencourt, C., Colin, E., Boudahi, A. et al., Mass Spectrometry-Based Differentiation of Oral Tongue Squamous Cell Carcinoma and Nontumor Regions With the SpiderMass Technology. *Frontiers in Oral Health* 2022, *3*, 827360. doi:10.3389/froh.2022.827360.
- [65] Woolman, M., Kuzan-Fischer, C. M., Ferry, I., Kiyota, T. et al., Picosecond Infrared Laser Desorption Mass Spectrometry Identifies Medulloblastoma Subgroups on Intrasurgical Timescales. *Cancer Research* 2019, *79*, 2426–2434. doi:10.1158/0008-5472.CAN-18-3411.
- [66] Katz, L., Woolman, M., Kiyota, T., Pires, L. et al., Picosecond Infrared Laser Mass Spectrometry Identifies a Metabolite Array for 10 s Diagnosis of Select Skin Cancer Types: A Proof-of-Concept Feasibility Study. *Analytical chemistry* 2022, *94*, 16821–16830. doi:10.1021/acs.analchem.2c03918.
- [67] Duck, F. A., in: Duck, F. A. (Ed.), *Physical Properties of Tissues*, Academic Press, London 1990, pp. 137–165.
- [68] Hahn, J., Moritz, M., Voß, H., Pelczar, P. et al., Tissue Sampling and Homogenization in the Sub-Microliter Scale with a Nanosecond Infrared Laser (NIRL) for Mass Spectrometric Proteomics. *International journal of molecular sciences* 2021, *22*. doi:10.3390/ijms221910833.
- [69] Hänel, L., Gosau, T., Maar, H., Valentiner, U. et al., Differential Proteome Analysis of Human Neuroblastoma Xenograft Primary Tumors and Matched Spontaneous Distant Metastases. *Scientific reports* 2018, *8*, 13986. doi:10.1038/s41598-018-32236-1.
- [70] Donnarumma, F., Murray, K. K., Laser ablation sample transfer for localized LC-MS/MS proteomic analysis of tissue. *Journal of mass spectrometry : JMS* 2016, *51*, 261–268. doi:10.1002/jms.3744.

- [71] Dong, C., Richardson, L. T., Solouki, T., Murray, K. K., Infrared Laser Ablation Microsampling with a Reflective Objective. *Journal of the American Society for Mass Spectrometry* 2022, 33, 463–470. doi:10.1021/jasms.1c00306.
- [72] Lee, H.-G., Jo, J., Hong, H.-H., Kim, K. K. et al., State-of-the-art housekeeping proteins for quantitative western blotting: Revisiting the first draft of the human proteome. *Proteomics* 2016, 16, 1863–1867. doi:10.1002/pmic.201500344.
- [73] Duck, F. A., in: Duck, F. A. (Ed.), *Physical Properties of Tissues*, Academic Press, London 1990, pp. 319–328.
- [74] Jowett, N., Wöllmer, W., Reimer, R., Zustin, J. et al., Bone ablation without thermal or acoustic mechanical injury via a novel picosecond infrared laser (PIRL). *Otolaryngology–Head and Neck Surgery* 2014, 150, 385–393. doi:10.1177/0194599813517213.
- [75] Friedrich, R. E., Quade, M., Jowett, N., Kroetz, P. et al., Ablation Precision and Thermal Effects of a Picosecond Infrared Laser (PIRL) on Roots of Human Teeth: A Pilot Study Ex Vivo. *In vivo (Athens, Greece)* 2020, 34, 2325–2336. doi:10.21873/invivo.12045.
- [76] Cai, X., Xue, Z., Wu, C., Sun, R. et al., High-throughput proteomic sample preparation using pressure cycling technology. *Nat Protoc* 2022, 17, 2307–2325. doi:10.1038/s41596-022-00727-1.
- [77] Stadlhofer, R., Moritz, M., Fuh, M. M., Heeren, J. et al., Lipidome Analysis of Oropharyngeal Tumor Tissues Using Nanosecond Infrared Laser (NIRL) Tissue Sampling and Subsequent Mass Spectrometry. *International journal of molecular sciences* 2023, 24. doi:10.3390/ijms24097820.
- [78] Ren, L., Robertson, W. D., Reimer, R., Heinze, C. et al., Towards instantaneous cellular level bio diagnosis: laser extraction and imaging of biological entities with conserved integrity and activity. *Nanotechnology* 2015, 26, 284001. doi:10.1088/0957-4484/26/28/284001.
- [79] Ubhi, B. K., Direct Infusion-Tandem Mass Spectrometry (DI-MS/MS) Analysis of Complex Lipids in Human Plasma and Serum Using the Lipidyzer™ Platform. *Methods in molecular biology (Clifton, N.J.)* 2018, 1730, 227–236. doi:10.1007/978-1-4939-7592-1_15.
- [80] Cao, Z., Schmitt, T. C., Varma, V., Sloper, D. et al., Evaluation of the Performance of Lipidyzer Platform and Its Application in the Lipidomics Analysis in Mouse Heart and Liver. *Journal of proteome research* 2020, 19, 2742–2749. doi:10.1021/acs.jproteome.9b00289.
- [81] Fatou, B., Saudemont, P., Duhamel, M., Ziskind, M. et al., Real time and in vivo pharmaceutical and environmental studies with SpiderMass instrument. *Journal of Biotechnology* 2018, 281, 61–66. doi:10.1016/j.jbiotec.2018.06.339.
- [82] Ogrinc, N., Kruszewski, A., Chaillou, P., Saudemont, P. et al., Robot-Assisted SpiderMass for In Vivo Real-Time Topography Mass Spectrometry Imaging. *Analytical chemistry* 2021, 93, 14383–14391. doi:10.1021/acs.analchem.1c01692.
- [83] Saudemont, P., Quanico, J., Robin, Y.-M., Baud, A. et al., Real-Time Molecular Diagnosis of Tumors Using Water-Assisted Laser Desorption/Ionization Mass Spectrometry Technology. *Cancer Cell* 2018, 34, 840-851.e4. doi:10.1016/j.ccell.2018.09.009.
- [84] Woolman, M., Ferry, I., Kuzan-Fischer, C. M., Wu, M. et al., Rapid determination of medulloblastoma subgroup affiliation with mass spectrometry using a handheld picosecond infrared laser desorption probe. *Chemical science* 2017, 8, 6508–6519. doi:10.1039/c7sc01974b.
- [85] Katz, L., Kiyota, T., Woolman, M., Wu, M. et al., Metabolic Lipids in Melanoma Enable Rapid Determination of Actionable BRAF-V600E Mutation with Picosecond Infrared Laser Mass Spectrometry in 10 s. *Analytical chemistry* 2023, 95, 14430–14439. doi:10.1021/acs.analchem.3c02901.
- [86] Lintonen, T. P. I., Baker, P. R. S., Suoniemi, M., Ubhi, B. K. et al., Differential mobility spectrometry-driven shotgun lipidomics. *Analytical chemistry* 2014, 86, 9662–9669. doi:10.1021/ac5021744.













- [87] Voß, H., Moritz, M., Pelczar, P., Gagliani, N. et al., Tissue Sampling and Homogenization with NIRL Enables Spatially Resolved Cell Layer Specific Proteomic Analysis of the Murine Intestine. *International journal of molecular sciences* 2022, 23. doi:10.3390/ijms23116132.
- [88] van der Post, S., Hansson, G. C., Membrane protein profiling of human colon reveals distinct regional differences. *Molecular & cellular proteomics : MCP* 2014, 13, 2277–2287. doi:10.1074/mcp.M114.040204.
- [89] Magro, F., Rodrigues, A., Vieira, A. I., Portela, F. et al., Review of the disease course among adult ulcerative colitis population-based longitudinal cohorts. *Inflammatory bowel diseases* 2012, 18, 573–583. doi:10.1002/ibd.21815.
- [90] Iacopetta, B., Are there two sides to colorectal cancer? *International journal of cancer* 2002, 101, 403–408. doi:10.1002/ijc.10635.
- [91] Buckley, C. D., Ospelt, C., Gay, S., Midwood, K. S., Location, location, location: how the tissue microenvironment affects inflammation in RA. *Nat Rev Rheumatol* 2021, 17, 195–212. doi:10.1038/s41584-020-00570-2.
- [92] Sachs, P. C., Mollica, P. A., Bruno, R. D., Tissue specific microenvironments: a key tool for tissue engineering and regenerative medicine. *J Biol Eng* 2017, 11, 34. doi:10.1186/s13036-017-0077-0.
- [93] LaPointe, L. C., Dunne, R., Brown, G. S., Worthley, D. L. et al., Map of differential transcript expression in the normal human large intestine. *Physiological genomics* 2008, 33, 50–64. doi:10.1152/physiolgenomics.00185.2006.
- [94] Birkenkamp-Demtroder, K., Olesen, S. H., Sørensen, F. B., Laurberg, S. et al., Differential gene expression in colon cancer of the caecum versus the sigmoid and rectosigmoid. *Gut* 2005, 54, 374–384. doi:10.1136/gut.2003.036848.
- [95] Siri, S., Zhao, Y., Maier, F., Pierce, D. M., Feng, B., The Macro- and Micro-Mechanics of the Colon and Rectum I: Experimental Evidence. *Bioengineering (Basel, Switzerland)* 2020, 7. doi:10.3390/bioengineering7040130.
- [96] Tsai, C.-F., Zhang, P., Scholten, D., Martin, K. et al., Surfactant-assisted one-pot sample preparation for label-free single-cell proteomics. *Communications biology* 2021, 4, 265. doi:10.1038/s42003-021-01797-9.
- [97] Navolić, J., Moritz, M., Voß, H., Schlumbohm, S. et al., Direct 3D Sampling of the Embryonic Mouse Head: Layer-wise Nanosecond Infrared Laser (NIRL) Ablation from Scalp to Cortex for Spatially Resolved Proteomics. *Analytical chemistry* 2023, 95, 17220–17227. doi:10.1021/acs.analchem.3c02637.
- [98] Louveau, A., Filiano, A. J., Kipnis, J., Meningeal whole mount preparation and characterization of neural cells by flow cytometry. *Current Protocols in Immunology* 2018, 121, e50. doi:10.1002/cpim.50.
- [99] Dasgupta, K., Jeong, J., Developmental biology of the meninges. *Genesis (New York, N.Y. : 2000)* 2019, 57, e23288. doi:10.1002/dvg.23288.
- [100] Sakka, L., in: Cinalli, G., Ozek, M. M., Sainte-Rose, C. (Eds.), *Pediatric Hydrocephalus*, Springer International Publishing, Cham 2020, pp. 1–55.
- [101] Santorella, E., Balsbaugh, J. L., Ge, S., Saboori, P. et al., Proteomic interrogation of the meninges reveals the molecular identities of structural components and regional distinctions along the CNS axis. *Fluids Barriers CNS* 2023, 20, 74. doi:10.1186/s12987-023-00473-w.
- [102] Dyrlund, T. F., Poulsen, E. T., Scavenius, C., Nikolajsen, C. L. et al., Human cornea proteome: identification and quantitation of the proteins of the three main layers including epithelium, stroma, and endothelium. *Journal of proteome research* 2012, 11, 4231–4239. doi:10.1021/pr300358k.
- [103] MacDonald, M. L., Favo, D., Garver, M., Sun, Z. et al., Laser capture microdissection-targeted mass spectrometry: a method for multiplexed protein quantification within individual layers of the cerebral cortex. *Neuropsychopharmacol* 2019, 44, 743–748. doi:10.1038/s41386-018-0260-0.

- [104] Ogawa, M., Miyata, T., Nakajima, K., Yagyu, K. et al., The reeler gene-associated antigen on Cajal-Retzius neurons is a crucial molecule for laminar organization of cortical neurons. *Neuron* 1995, *14*, 899–912. doi:10.1016/0896-6273(95)90329-1.
- [105] Copp, A. J., Harding, B. N., Neuronal migration disorders in humans and in mouse models--an overview. *Epilepsy Research* 1999, *36*, 133–141. doi:10.1016/S0920-1211(99)00047-9.
- [106] Hevner, R. F., Layer-specific markers as probes for neuron type identity in human neocortex and malformations of cortical development. *J Neuropathol Exp Neurol* 2007, *66*, 101–109. doi:10.1097/nen.0b013e3180301c06.
- [107] Zheng, Y., Lin, C., Chu, Y., Gu, S. et al., Spatial metabolomics in head and neck tumors: a review. *Frontiers in oncology* 2023, *13*, 1213273. doi:10.3389/fonc.2023.1213273.
- [108] Escribá, P. V., Busquets, X., Inokuchi, J., Balogh, G. et al., Membrane lipid therapy: Modulation of the cell membrane composition and structure as a molecular base for drug discovery and new disease treatment. *Progress in Lipid Research* 2015, *59*, 38–53. doi:10.1016/j.plipres.2015.04.003.
- [109] Schluter, M., Fuh, M. M., Maier, S., Otte, C. et al., Towards OCT-Navigated Tissue Ablation with a Picosecond Infrared Laser (PIRL) and Mass-Spectrometric Analysis. *Annual International Conference of the IEEE Engineering in Medicine and Biology Society. IEEE Engineering in Medicine and Biology Society. Annual International Conference 2019*, 2019, 158–161. doi:10.1109/EMBC.2019.8856808.
- [110] Dadkhah, A., Zhou, J., Yeasmin, N., Jiao, S., Integrated multimodal photoacoustic microscopy with OCT- guided dynamic focusing. *Biomedical optics express* 2019, *10*, 137–150. doi:10.1364/BOE.10.000137.
- [111] Ecclestone, B. R., Hosseinaee, Z., Abbasi, N., Bell, K. et al., Three-dimensional virtual histology in unprocessed resected tissues with photoacoustic remote sensing (PARS) microscopy and optical coherence tomography (OCT). *Sci Rep* 2021, *11*, 13723. doi:10.1038/s41598-021-93222-8.
- [112] Hosseinaee, Z., Nima, A., Pellegrino, N., Khalili, L. et al., Functional and structural ophthalmic imaging using noncontact multimodal photoacoustic remote sensing microscopy and optical coherence tomography. *Sci Rep* 2021, *11*, 11466. doi:10.1038/s41598-021-90776-5.
- [113] *GESTIS-Stoffdatenbank*, <https://gestis.dguv.de/> (accessed July 24, 2024).

9 APPENDIX

9.1 RISK AND SAFETY STATEMENTS

List of the chemicals used in this work. The substances are listed with the corresponding hazard symbols, hazard statements and precautionary statements [113].

Chemical	Hazard symbol	Hazard statement(s)	Precautionary statement(s)
Acetonitrile		H225, H302+H312+H332, H319	P210, P280, P301+312, P303+P361+P353, P304+P340+P312, P305+P351+P338
Ammonium acetate*			
Ammonium bicarbonate		H302	P301+P312+P330
Dichloromethane		H315, H319, H336, H351	P201, P302+P352, P305+P351+P338, P308+P313
Dithiothreitol		H302, H315, H318	P264, P270, P280, P301+P312, P302+P352, P305+P351+P338
n-Dodecyl β -D-maltoside*			
Formic acid		H226, H302, H331, H314	P210, P280, P303+P361+P353, P304+P340+P310, P305+P351+P338
Iodoacetamide		H301, H317, H334, H413	P261, P264, P273, P280, P301+P310, P302+P352
Methanol		H225, H301+H311+H331, H370	P210, P233, P280, P301+310, P303+P361+P353, P304+P340+P311
Methyl tert-butyl ether		H225, H315	P210, P233, P240, P241, P242, P303+P361+P353
1-Propanol		H225, H318, H336	P210, P240, P280, P305+P351+P338, P313, P403+P233
2-Propanol		H225, H319, H336	P210, P240, P305+P351+P338, P403+P233
Sodium deoxycholate		H302	P264, P270, P301+P312, P501
Triethylammonium bicarbonate*			
Trypsin		H315, H319, H334, H335	P261, P264, P271, P280, P302+P352, P305+P351+P338

*No hazardous substance according to GHS

10 ACKNOWLEDGEMENTS

At the beginning of my studies, I wondered what it would be like when I held my doctoral thesis in my hands. Now the time has come, and I realize that I am both very proud and relieved, but above all very happy and grateful. Grateful, that I have been lucky enough to meet people in my life, who have supported me professionally and privately and encouraged me on my path to my doctorate.

First of all, I would like to thank my doctoral supervisor Prof. Dr. Hartmut Schlüter for the interesting research question and the opportunity to realize my ideas in this thesis. I have learned a great deal during the period of my doctorate and very much appreciate the way I was challenged and supported.

I would also like to thank my colleague and friend Dr.-Ing. Jan Hahn. When we're not developing new ideas together at the Laser Group headquarters, it's just as nice to go on private adventures with you. You are an inspiring person; I am lucky to call you a friend and it is always a great pleasure to work with you.

Additionally, I would like to thank the entire Schlüter working group, namely the former group members Dr. Christoph Krisp and Dr. Hannah Voß as well as my current colleagues Dr. Maria Riedner, Bente Siebels, Thomas Mair and above all Sönke Harder, probably the most important person in the working group. Thanks for shaping my time as a doctoral student and the unforgettable moments. I always felt very comfortable and appreciate the respectful interaction and the opportunity for professional discussions.

A very special thanks also goes to my family. Without you, I would not have been able to complete my studies, and I would also like to thank you for your support and constant confidence, even when things got tough. Thank you for your understanding and for your love.

A big thank you also goes to my mother and father-in-law Anette and Wolfgang. I could not imagine a better second family.

My dearest friends Sina, Lana and Chrissi. You have been with me for so many years now and I couldn't be happier to have such great friends around me who are always ready with an open ear and advice. Or even just with a hug. Thank you for being here. I look forward to many more unforgettable moments with you.

When I think about who will be most happy about my title, I know it will be my friend Aem, who has affectionately called me "the doctor" for several years which caused some confused looks. Now I can officially bear the title! Thank you for your support and, above all, for the many wonderful moments in our friendship.

A big thank you goes to my friends Maja and Anja for proofreading this work. Your understanding of language is simply impressive, and I am grateful for your support.

Finally, I would like to thank my wife, Linda. I am lucky to have found the person of my heart in you, who understands me without words and makes me so infinitely happy with her love and kindness. Whenever I get stuck or am plagued by doubts, you are there, by my side and making me feel that everything will be alright. I'm very much looking forward to our future and everything that lies ahead. I love you.

11 DECLARATION

Hiermit versichere ich an Eides statt, die vorliegende Dissertationsschrift selbst verfasst und keine anderen als die angegebenen Quellen und Hilfsmittel benutzt zu haben. Sofern im Zuge der Erstellung der vorliegenden Dissertationsschrift generative Künstliche Intelligenz (gKI) basierte elektronische Hilfsmittel verwendet wurden, versichere ich, dass meine eigene Leistung im Vordergrund stand und dass eine vollständige Dokumentation aller verwendeten Hilfsmittel gemäß der Guten wissenschaftlichen Praxis vorliegt. Ich trage die Verantwortung für eventuell durch die gKI generierte fehlerhafte oder verzerrte Inhalte, fehlerhafte Referenzen, Verstöße gegen das Datenschutz- und Urheberrecht oder Plagiate.



Hamburg, den 31.07.2024